Search for Cosmic High Energy Neutrinos with the AMANDA-B10 Detector

DISSERTATION

zur Erlangung des akademischen Grades
doctor rerum naturalium
(dr. rer. nat.)
im Fach Physik

eingereicht an der
Mathematisch-Naturwissenschaftlichen Fakultät I
Humboldt-Universität zu Berlin

von
Dipl.-Phys. Matthias J. Leuthold
geboren am 23.02.1971 in Dresden

Präsident der Humboldt-Universität zu Berlin:
Prof. Dr. Jürgen Mlynek

Dekan der Mathematisch-Naturwissenschaftlichen Fakultät I:
Prof. Dr. Bernhard Ronacher

Gutachter:

1. Prof. Dr. Th. Lohse
2. Prof. Dr. P. O. Hulth
3. Prof. Dr. P. Söding

Eingereicht am: 6. Oktober 2001
Tag der mündlichen Prüfung: 1. November 2001

Abstract

High energy neutrinos are a possible probe for cosmic acceleration mechanisms. Using data taken with the AMANDA-B10 detector in 1997 an upper limit of $E^2 d\Phi/dE < 10^{-6}$ cm^{-2}s^{-1}sr^{-1}GeV on the flux of cosmic neutrinos with energies between 5 TeV and 1 PeV was obtained.

Keywords:
Neutrinos, Cosmic rays, High energy, AMANDA

Zusammenfassung

Diese Arbeit beschreibt die Suche nach hochenergetischen kosmischen Neutrinos mit dem AMANDA-B10 Detektor.

Das Antarctic Muon and Neutrinos Detection Array - AMANDA - ist ein Experiment zum Nachweis hochenergetischer Neutrinos. Es besteht aus einem Gitter optischer Detektoren, die in den antarktischen Gletscher eingeschmolzen wurden. Hochenergetische Myonneutrinos können anhand aufwärts laufender Myonspuren identifiziert werden. Nur Neutrinos reagieren ausschließlich durch die schwache Wechselwirkung, was sie zur einzigen Teilchensorte macht, die die ganze Erde durchlaufen kann. Aufwärtslaufende Spuren sind daher eine klare Signatur für neutrinoinduzierte Ereignisse. Die Richtung der Myonen kann anhand des abgestrahlten Cherenkovlichtes rekonstruiert werden. Für Neutrinoenergien oberhalb einiger hundert GeV behält das Myon die Richtung des Neutrinos im wesentlichen bei. Aus der Richtung des Myons kann daher auf die Richtung des Neutrinos geschlossen werden. Das erlaubt die Identifikation von Quellen.

Die häufigste Klasse von Untergrundereignissen sind abwärtslaufende Spuren von Myonen, die durch kosmische Strahlen in der Erdatmosphäre erzeugt werden. Damit ist der wichtigste Selektionsparameter der rekonstruierte Zenithwinkel. Ein weitere Klasse von Untergrundereignissen für die Beobachtung kosmische Neutrinos sind aufwärtslaufende Myonspuren von sogenannten atmosphärischen Neutrinos. Das sind Neutrinos, die von der kosmischen Strahlung in der Atmosphäre der Nordhalbkugel erzeugt werden, die Erde durchlaufen und als aufwärtslaufende Spuren die gleiche Signatur haben wie kosmische Neutrinos. Im Falle von Punktquellen ist die Identifikation kosmischer Neutrinos über die Häufung von Neutrinos aus einer bestimmten Richtung möglich. Eine weitere Möglichkeit, kosmische Neutrinos von atmosphärischen Neutrinos zu unterscheiden, ist die Energieverteilung: atmosphärische Neutrinos haben ein Energiespektrum mit einem spektralen Index von ungefähr -3.7, während für kosmische Neutrinos ein Spektrum mit einem spektralen Index von -2 erwartet wird. Die Signatur kosmischer Neutrinos ist daher ein Überschuß von hochenergetischen Ereignissen. Zur Selektion dieser Ereignisse ist ein Energieparameter notwendig.

Das Thema dieser Arbeit ist die Suche nach einem diffusen Fluß hochenergetischer kosmischer Neutrinos, als die Überlagerung der Flüsse von vielen, für sich genommen nicht nachweisbaren Quellen. Zum Nachweis der Funktionsfähigkeit des Detektors wurde zuerst die Separation von atmosphärischen Neutrinos mitentwickelt. Die erhaltenen Kandidaten wurden auf einen Überschuß hochenergetischer Neutrinos untersucht. Dazu wurde die Methode zur Energierekonstruktion, die für den Baikal-Detektor entwickelt wurde, an die optischen Eigenschaften von Eis angepaßt. Eine Analyse der Fehlerbeiträge ergab jedoch, daß stochastische Fluktuationen der Energie- und damit Lichtdeposition die Energieauflösung begrenzen. Die Suche nach alternativen energieabhängigen Selektionsparametern ergab die Anzahl der getroffen Kanäle als effektiven Selektionsparameter für hochenergetische Ereignisse. Mit diesem Parameter konnte

die Sensitivität des Detektors für hochenergetische Ereignisse abgeschätzt werden. Eine detaillierte Analyse ergab jedoch systematische Abweichungen zwischen Daten und Monte Carlo.

Als Konsequenz wurde ein separater Filter für hochenergetische Ereignisse entwickelt. Mit Separationsschnitten auf nur fünf Parameter konnten die Daten auf weniger als ein Prozent reduziert werden. Die abschließenden Schnitte wurden mit einem Optimierungsprogramm entwickelt. Zur Optimierung der Sensitivität wurde eine Vielfalt von Parametern verglichen. Ein Satz besonders hochenergetischer Ereignisse konnte selektiert werden. Die Zahl und Verteilung der Ereignisse ist konsistent mit der Erwartung für atmosphärische Neutrinoereignisse. Ein Überschuß von Ereignissen hoher Energie wurde nicht beobachtet. Nach einem letzten Schnitt auf die Anzahl der getroffenen Kanäle als Energieparameter ließ sich daher eine obere Grenze für den Fluß hochenergetischer kosmischer Neutrinos ableiten. Unter der generischen Annahme eines E_ν^{-2}-Spektrums ergibt sich eine Grenze für Energien zwischen $5 \cdot 10^3$ GeV und $1 \cdot 10^6$ GeV von

$$E^2 \left(\frac{d\Phi_{\nu+\bar{\nu}}}{dE} \right)_{90\%\ C.L.} \leq 1.0 \cdot 10^{-6} \mathrm{cm}^{-2} \mathrm{s}^{-1} \mathrm{sr}^{-1} \mathrm{GeV} \qquad .$$

Der systematische Fehler durch die Unsicherheiten der Erwartung für den atmosphärischen Neutrinofluß, die Unsicherheit der Sensitivität der optischen Module und die Unsicherheiten der Simulation von Myon- und Photonpropagation wurde mit maximal 10% abgeschätzt und ist in der Flußgrenze berücksichtigt.

Der Vergleich zu anderen experimentellen Flußgrenzen und theoretischen Vorhersagen ist in Abbildung 8.1 gezeigt. Die hier vorgestellte Flußgrenze ist die gegenwärtig härteste experimentelle Grenze im angegebenen Energiebereich. Der Wert ist geringfügig niedriger als eine theoretische Grenze, die aus der Intensität der diffusen kosmischen Gammastrahlung abgeleitet wurde, und schließt eines der Modelle für Aktive Galaktische Kerne mit Neutrinoproduktion in Proton-Proton-Wechselwirkungen knapp aus.

Das Ergebnis dieser Arbeit ist als vorläufige Flußgrenze auf zwei internationalen Konferenzen gezeigt worden und wird in einer Zeitschrift publiziert werden.

Das wesentliche methodische Ergebnis dieser Arbeit ist die Entwicklung und systematische Analyse eines Filters für hochenergetische kosmische Neutrinos. Die Entwicklung des Verständnisses der Daten hat mehrere Jahre in Anspruch genommen. In dieser Zeit sind der Detektor vervollständigt und mehr Daten genommen worden. Die Analyse dieser Daten sollte eine baldige Verbesserung der Sensitivität um einen Faktor 5 bis 10 ermöglichen.

Sclagwörter:
Neutrinos, kosmische Strahlung, Hochenergie, AMANDA

Acknowledgments

This work has been made possible by the support of many people. It is my pleasure to acknowledge their contributions at this point.

First of all, I want to thank Dr. Christian Spiering for the ignition of my fascination in neutrino astronomy, the space to develop my ideas and the support in the phase of completion. I thank Prof. Dr. T. Lohse for taking the responsibility for this work. Further I would like to thank Dr. Peter Steffen for his calm and friendly advice in the second half of my work.

I very much appreciated the support of the members of AMANDA group in Zeuthen. Especially for the proofreading on short notice I thank Alexander Biron, Sebastian Böser, Tonio Hauschild, Marek Kowalski and Henrike Wissing.

Another group of people has contributed to this work during several working visits in Madison and Stockholm. I would like to thank Francis Halzen and Per-Olof Hulth for making these stays possible. Further I would like to thank Gary Hill for the introduction to the physics and methods of diffuse neutrino flux measurements, Tyce DeYoung for fruitful discussions on science, non-science and the importance of style, and Katherine Rawlins for intensive proofreading.

Explicitely I would like to thank Stephan Hundertmark and Ole Streicher for the introduction to the technical and social circumstances of Siegmund and AMANDA. I thank Christopher Wiebusch for an intense and short phase of fruitful collaboration at the very beginning of my time with AMANDA.

I thank Henrike Wissing for an enjoyable year of work on IceCube and the inspiration during the writeup of this work, Markus Gaug for patient and ambitious instructions on `cuteval`.

Finally I want to thank the non-amandists that have supported me during the time of this work: Sabine Schlösser, Hildrun Freuling, Dr. Agathe Israel, Tilo Höhnel, Michael Koppitz, Kathrin Röschel, Kerstin Hörnich and Kathrin Werner.

Abschließend möchte ich die Gelegenheit nutzen, um mich bei meinen Eltern für viele Jahre der Unterstützung und Ermutigung zu bedanken.

Contents

Chapter 1

Introduction

The observation of the stars has fascinated humans for thousands of years. The longest time the naked eye was the only way to observe the skys. With the invention of the telescope, the horizon extended and changed the human understanding of the world. The methods invented over the last century have expanded the field of view over the entire range of the electro- magnetic spectrum. Today we watch the sky at all wavelengths from radio and infrared to X-ray and gamma ray energies, over many orders of magnitude in wavelength.

With the discovery of cosmic radiation in 1912, the proton established as a new type of messanger from space. Cosmic rays have been observed to with energies of up to 10^{20} eV, which is the energy of a tennis ball flying with 200 km/h concentrated in one single particle. This led to one of the most exciting puzzles in modern astronomy – the question about the origin of high energy cosmic rays. Since charged particles are deflected in cosmic magnetic fields, source identification requires the exploitation of neutral information carriers. A dozen sources of TeV gamma rays have been detected over the last decade. Still, a final answer may come only from a further principal extension of the observational window – neutrino astronomy.

Neutrinos are the only high energy particles that can carry information from the edge of the universe and from deep inside the most cataclysmic high energy processes. Affected only by the weak force (the gravitational force is negligible), they travel undeflected by magnetic fields and essentially unabsorbed over cosmological distances.

The small cross section that suggests the neutrino as a messenger over large distances and from dense accelerator regions makes it hard to detect at the same time. Therefore large detection areas are required. The benchmark area set by current source models is of the order of 1 km^2 [1]. The construction of underground detectors with these dimensions is excluded by obvious reasons. The remaining solution is the instrumentation of naturally occuring media, like water, ice or air.

Underwater/ice neutrino telescopes consist of a lattice of photomultipliers which detect the Cherenkov light emitted by charged secondary particles from neutrino interactions. AMANDA is the largest of these arrays. It is located at the geographic South Pole and takes data since 1996. After a lot of effort has been invested to construct and upgrade the detector, the last years were needed to develop the understanding of the data. This was a non-trivial task since ice is a very non-homogeneous medium. With the consolidation of the understanding of the atmospheric neutrino signal, the stage has been set for the search for cosmic (i.e extra-terrestrial) neutrinos.

One of the possibilities to detect a flux of cosmic neutrinos is the search for a cumulative, diffuse flux of a population of unresolved sources. Due to the relatively hard spectrum expected from cosmic accelerators, it would be observable as an excess over atmospheric neutrinos yielding a tail at high energies. The search for such a diffuse flux of cosmic neutrinos was the topic of this thesis.

In the following chapter possible neutrino sources and the landscape of flux predictions and limits will be introduced. In chapter three the principle of detection of high energy neutrinos and the existing detectors will be described. Chapter four is focused on the AMANDA detector. In chapter five the Monte Carlo and the methods used later on are introduced. In chapter six the analysis of the atmospheric neutrino sample that was an important input for the high energy neutrino search is discussed. The main results of this thesis, the separation of a high energy neutrino sample and the derivation of an upper limit are described in chapter seven.

Chapter 2

High Energy Neutrino Sources

The main motivation for high energy neutrino astronomy is the search for the origin of cosmic rays. Cosmic rays are observed over many orders of magnitude in energy and in flux. The sources that accelerate protons to energies of 10^{20} eV are still unknown.

Non-thermal gamma ray spectra of active galactic nuclei (AGN), gamma ray bursts (GRBs) or supernova remnants (SNR) indicate populations of relativistic particles suggesting them as cosmic accelerators. Because charged particles are deflected in galactic magnetic fields and absorbed by interstellar media, only neutral messengers are well suited for location of cosmic ray sources.

Photons that travel straight through the magnetic fields however are attenuated due to absorption by dust, and at higher energies by pair production with the infrared and the cosmic microwave background radiation: ($\gamma + \gamma_{IR,CMBR} \rightarrow e^+ + e^-$). Thus the gamma ray horizon is limited. In figure 2.1 the horizon for high energy gammas is shown with the corresponding radiation causing the gamma ray absorption. Further, gamma rays may originate from the decay of neutral pions created in hadronic interactions but can as well be produced by electrons via synchrotron radiation accompanied by inverse Compton scattering.

Alternative messengers are neutrinos. They are exclusively expected from proton accelerators. Because they interact only weakly they are a unique probe into inner regions of an optically thick source or even for regions of space that are hidden to photon astronomy completely. In this sense neutrino astronomy is a new observational window into the universe.

In this chapter candidates for proton acceleration as possible neutrino sources shall be introduced. There is a number of ingredients to the derivation of neutrino flux predictions that are relatively settled. They will be introduced beforehand to prepare the ground for the discussion of the landscape of neutrino flux predictions and limits:

A The commonly assumed acceleration mechanism for cosmic rays is Fermi acceleration. The search for sources of the cosmic rays is a search for cosmic objects that are hosts to shock waves or magnetic turbulences that cause Fermi acceleration (section 2.1).

B The cosmic ray spectrum observed is one of the main motivations and guide line for predictions at the same time. Together with the gamma ray spectrum it serves as the basis for the derivation of bounds on the expected diffuse neutrino background flux. The observation will be discussed in section 2.2 and the limit calculation in section 2.6.

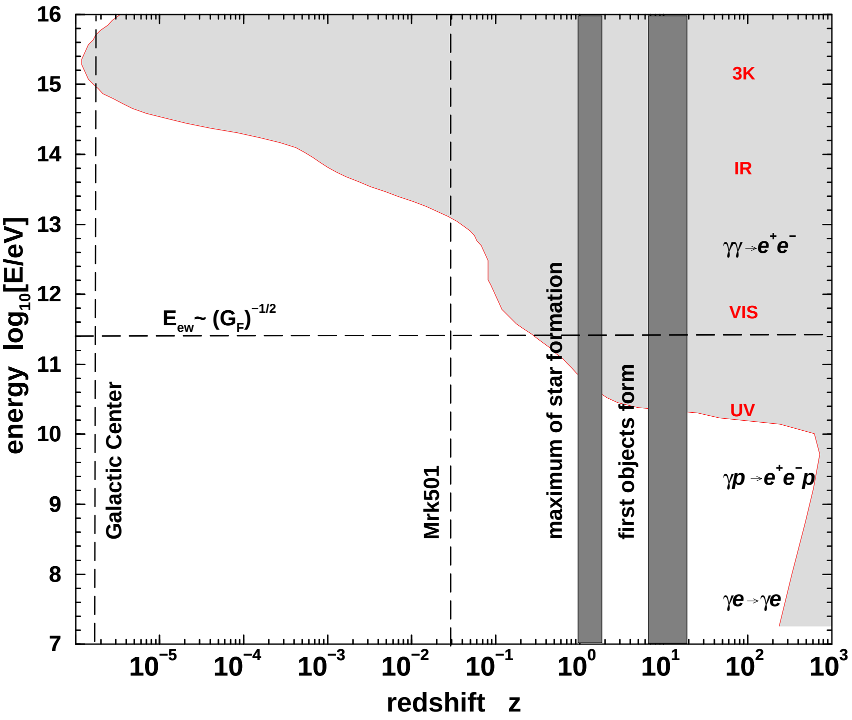

Figure 2.1: Gamma ray horizon. The blazar Makarian 501 is one of the few TeV gamma ray sources observed. The steepening in the spectrum above 10 TeV is explained by absorption due to the diffuse infrared background radiation [2] (figure taken from [3]).

C Neutrino production processes are well understood from terrestrial accelerator laboratory physics. The decays relevant for cosmic neutrino production will be introduced allowing for a classification according to the properties of the proton beam and the target forming the natural neutrino factories (section 2.3).

After the description of the ingredients the possible neutrino sources and flux limits will be introduced in order to understand the motivation for high energy neutrino telescopes (section 2.6). In this chapter it will be shown that the investigation of high energy cosmic neutrinos is a tool to probe cosmic objects with respect to their proton acceleration capabilities. Besides the search for the origin of the cosmic rays there are secondary motivations for neutrino astronomy:

- The experimental test of the neutrino-nucleon cross sections at energies not available from man made accelerators was the motivation for the first proposal by Markov(1960) to observe upward moving leptons in underground detectors.
- If there are exotic particles such as WIMPs or magnetic monopoles they will be detectable with large open medium Cherenkov detectors.
- Frequently mentioned is the fascination that there might be the completely unexpected source as has occurred once in a while when completely new methods or search windows were used to observe nature.

2.1 Cosmic Particle Acceleration

Fermi acceleration [4, 5] is commonly accepted as the most plausible mechanism for cosmic particle acceleration because it explains the power law energy spectrum observed for cosmic rays and gamma rays quite naturally.

The two main elements of Fermi acceleration are the assumption that (i) a particle passes through the acceleration region several times (encounters) gaining a fixed fraction f of its energy every time and (ii) that the escape probability P_{esc} at every encounter is constant. The energy after n encounters can be written as $E_n = E_0(1+f)^n$. The probability to find the particle in the accelerator region after n encounters is $P_n = (1-P_{esc})^n$. Combining the two yields a power law spectrum. The number of particles with energy between E and $E+dE$ is given by

$$\frac{dN}{dE} \propto N_0 \cdot E^{-(\gamma+1)} \quad \text{with} \quad \gamma = \frac{\ln\left[1/(1-P_{esc})\right]}{\ln[1+f]} = 1+\epsilon, \tag{2.1}$$

where ϵ depends on the details of the shock dynamics and density and ranges between 0 and 0.3.

One separates two types of Fermi acceleration named according to the order of β in the energy gain, where β is the speed of the shock front or the magnetic cloud that delivers the energy for the particle acceleration [6].

First order Fermi acceleration is predicted for single shock waves. When a shock wave, i.e. a supersonic flow of matter, propagates into a population of particles with random velocity distribution a fraction of the particles will pass the shock front. The directed flow scatters a fraction of the particles back in front of the shock with on average increased energies. There elastic scattering randomizes the direction again, piping a fraction of the particles back into the shock front again and the whole process starts over again.

Second order Fermi acceleration occurs in turbulent magnetic clouds. In contrast to the infinite plane shock front where the reflection is directed in front of the shock the particle can be expelled in any direction. The average energy gain therefore is proportional to β^2.

Fermi acceleration is often compared to a tennis ball gaining energy from the reflection at a moving wall. The particle however is reflected collisionless by a "magnetic mirror". The reflection is due to the magnetic field changing intensity yielding a change of the pitch angle of the gyration. Collisions would introduce energy loss and reduce the net acceleration.

In both cases there is a finite escape probability due to scattering. The mechanism can be stopped by several causes limiting the maximum energy. A global limit is given by the simple relation $E < BR$: when the gyro radius exceeds the dimension of the confining magnetic field the particle will escape. Another simple limitation are energy dependent energy loss processes or the lifetime of the shock. An important example for this cutoff energy are supernova remnants that will be discussed in the section on potential sources.

Shock wave acceleration has been observed to work in the solar system. Particles with energies in the MeV range, typical for nuclear processes in the sun, were observed to be accelerated up to GeV energies giving empirical support to the theory of acceleration by plasma waves.

Magnetic reconnection at the surface of accretion disks is a less common suggestion for the acceleration mechanism behind the rapid intensity variation observed in gamma rays [7]. Magnetic reconnection in the sun's surface could be the reason for solar flares. The strong directed electric fields perpendicular to the surface eject hot plasma [8]. Protons and electrons can be accelerated to energies of 10^{20-21} eV on shorter time scales than in stochastic acceleration. The protons produce pions and thus gamma rays and neutrinos. While gamma rays will cascade neutrinos will escape. In contrast to other models this one predicts strong neutrino fluxes for sources with gamma ray spectra that do *not* extend to TeV energies.

2.2 The Primary Cosmic Ray Spectrum

Cosmic rays (CR) have been observed for the first time by Victor Hess in 1912. Today the observation extends over many orders of magnitude in energy involving a variety of observation techniques ([9] and references therein): from GeV to ≈ 10 TeV they are detected directly with satellites and balloon born detectors. At higher energies these detectors are flux limited. Single atmospheric muon spectra at sea level are used to measure the CR spectrum up to 100 TeV energies. Air shower experiments measure CR with energies above ≈ 2 TeV to the highest observed energies. The intensity ranges over 20 orders of magnitude from 1 particle$/cm^2s$ at energies of about a GeV to 1 particle$/km^2y$ for energies of about 10^{10} GeV ($\approx 10^{19}$ eV).

The energy spectrum closely follows a power law: $dN \propto E^{-\alpha}dE$ (see figure 2.2). The spectral index remains nearly constant over the entire energy range leaving two slight changes in slope as the only features of the spectrum: at about $E_{knee} \approx 10^{16}$ eV the index changes from 2.7 to 3.0 creating the so called knee. Above $E_{ankle} \approx 10^{18}$ eV it flattens again forming the so called ankle [6]:

$$\frac{dN(E)}{dE} \sim E^{-\alpha}, \quad \text{where } \alpha \approx \begin{cases} 2.7 & \text{for} \quad E \leq E_{knee} \\ 3.0 & \text{for} \quad E_{knee} < E < E_{ankle} \\ 2.7 & \text{for} \quad E \geq E_{ankle} \end{cases} \tag{2.2}$$

The three ranges of different spectral index are associated with different processes powering it.

The CR below the knee are believed to be of galactic origin. The leading source candidate are supernova remnants (SNR). These are powerful blast waves from the supernova explosion expanding into the interstellar medium or progenitor stellar winds. They qualify as proton accelerators for several reasons [3]:

- They show strong non-thermal power law photon spectra indicating the presence of relativistic electrons.
- The amount of power needed is just about the same provided by the observed supernova rate of three per century in the galaxy.
- The chemical composition of cosmic rays meets the one expected from supernovae after correction for spallation processes during propagation.

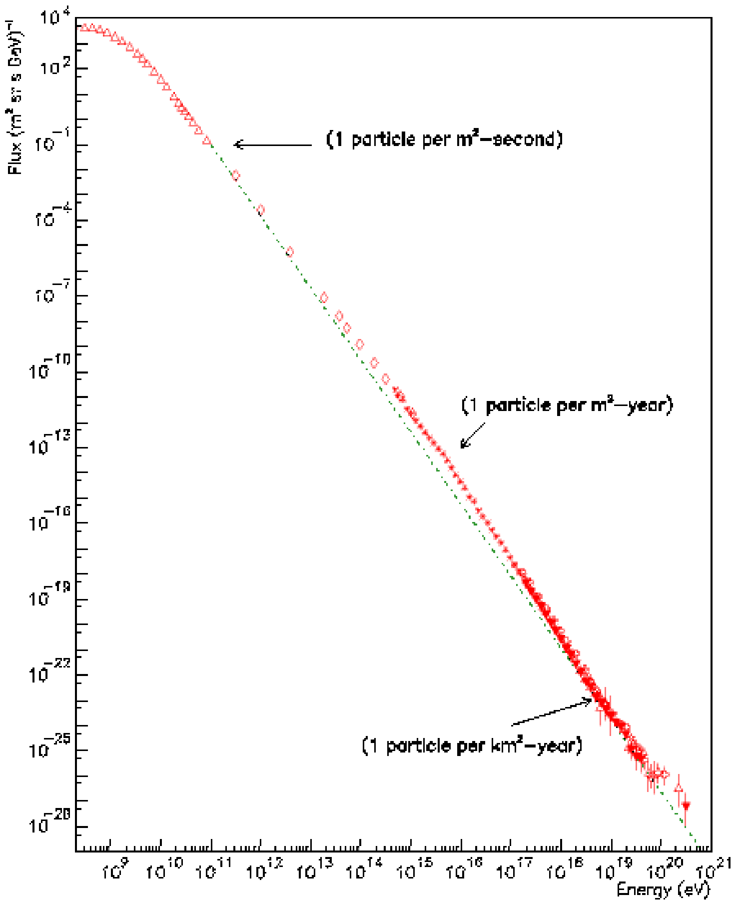

Figure 2.2: Primary cosmic ray spectrum (taken from [10]).

- Finally, the position of the knee is consistent with a cutoff energy in the range of 100 TeV due to the limited lifetime of the shock wave.

The only uncertainty about the role of SNRs as standard galactic CR accelerator arises from the missing TeV gamma ray observation [11] and [12]. The few established TeV sources are explained by synchrotron radiation and inverse Compton scattering from relativistic electrons [13]. The detection of neutrinos would confirm their role as proton accelerators.

The difference between the spectral index observed (2.7) and the one expected from Fermi acceleration (2.1-2.3) is explained by an energy dependent escape probability from the galaxy: $P \propto E^{\delta}$. Particles with higher energies have larger gyro radii and therefore are more likely to escape, resulting in a steepening of the spectrum (leaky box model). From relative abundance measurements of spallation products in the galaxy one can derive a value for $\delta \approx 0.6$ well consistent with $\epsilon \approx 0.1..0.3$ at the source.

The range above the ankle is believed to be of extragalactic origin. The magnetic field of

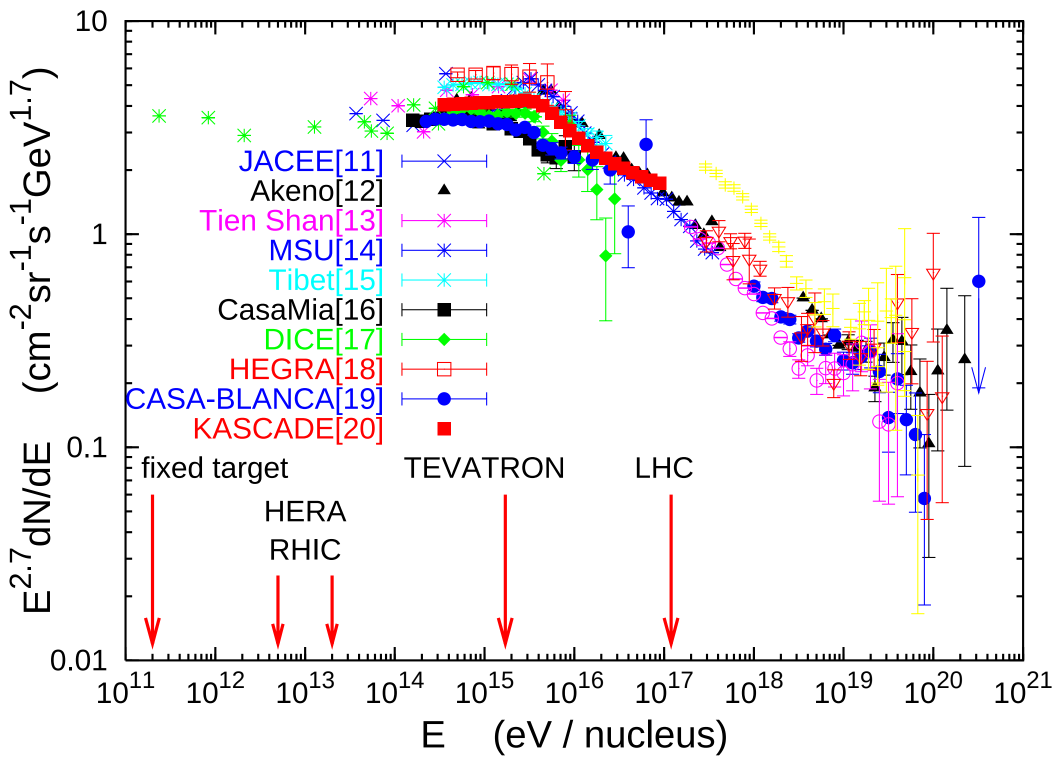

Figure 2.3: Primary cosmic ray spectrum (taken from [9]). The two changes in slope become visible when the flux is scaled with $E^{-2.7}$. For comparison the energies reached with terrestrial accelerators are shown.

the galaxy would not suffice to confine particles of this energy. Further there is the observation of a change in the composition at about 10^{18} eV and the hardening spectrum itself indicates a change in the origin [9]. Another support for this assumption is an observed indication of an anisotropy in the CR at 10^{18} eV showing a slight (4%) but significant excess from the direction of the galactic center [14, 15]. This anisotropy disappears for higher energies supporting the extragalactic origin. The spectrum above the ankle has therefore been used to normalize the expected neutrino fluxes from extragalactic acceleration candidates (see section 2.6).

Whether or not SNR turn out to be the source of CR, somewhere in space nature accelerates protons to incredibly high energies. With an appropriate target nearby a proton accelerator turns into a neutrino source as well.

2.3 Neutrino Production

The generic model of neutrino production is a power law proton beam hitting a target, producing pions and heavier mesons in large quantities. The charged mesons decay into leptons with the emission of neutrinos. The typical targets are ambient matter (for example accretion discs of black holes) or dense photon fields (for example thermal photons or photons with a power law spectrum from electron synchrotron radiation). Along with neutrinos from charged pions, gamma rays are produced from the decay of neutral pions:

$$\begin{array}{l} p+\gamma \rightarrow p + \pi^0 + X \\ \qquad\qquad\qquad \llcorner\!\!\rightarrow 2\gamma \\ \\ p + X \rightarrow \pi^0 + Y \\ \qquad\qquad \llcorner\!\!\rightarrow 2\gamma. \end{array} \tag{2.3}$$

In contrast to neutrinos, gamma rays can be generated by synchrotron radiation and inverse Compton scattering of relativistic electrons as well. They thus do not proove the existence of proton acceleration. Neutrinos are expected from beam dumps of proton beams only. The most important contributions come from pions and kaons:

$$\begin{array}{l} p + X \rightarrow \pi^{\pm} + Y \\ \qquad\quad \llcorner\!\!\rightarrow \mu^{\pm} + \nu_\mu(\bar{\nu}_\mu) \\ \qquad\qquad\quad \llcorner\!\!\rightarrow e^{\pm} + \nu_e(\bar{\nu}_e) + \bar{\nu}_\mu(\nu_\mu) \\ \\ p + X \rightarrow K^{\pm} + Y \\ \qquad\quad \llcorner\!\!\rightarrow \mu^{\pm} + \nu_\mu(\bar{\nu}_\mu) \\ \qquad\qquad\quad \llcorner\!\!\rightarrow e^{\pm} + \nu_e(\bar{\nu}_e) + \bar{\nu}_\mu(\nu_\mu) \\ \\ p + X \rightarrow K_L^0 + Y \\ \qquad\quad \llcorner\!\!\rightarrow \pi^{\pm} + \mu^{\pm} + \nu_\mu(\bar{\nu}_\mu) \\ \qquad\quad \llcorner\!\!\rightarrow \pi^{\pm} + e^{\pm} + \nu_e(\bar{\nu}_e) \end{array} \tag{2.4}$$

The targets (X) may be photons or hadrons, the decay products (Y) differ accordingly.

Intensity and spectrum of the neutrino beam are determined by the properties of the proton beam and the target properties, such as energy distribution and density. Besides the primary spectrum it is the competition between the decay in flight and (inelastic) interaction of the meson in the target medium that determines the secondary spectrum. Typical astronomical targets are dilute enough to allow all secondaries, including muons, to decay in flight. In this case the neutrino spectrum follows the primary spectrum closely. However, in dense targets absorption of the mesons rises with energy because of the longer path length of the meson. The free decay of higher energy mesons therefore is suppressed and the spectrum steepens.

Applying these conditions one can distinguish three classes of neutrino spectra typical for their production sites

> **At the accelerator** dilute targets allow free decay in flight, and the spectral index follows the hard primary spectrum as it comes from the accelerator ($\gamma \approx 2.1 - 2.3$).
>
> **In the galaxy** the interstellar medium is still dilute enough to allow free decay in flight. However, the proton beam spectrum is steeper due to the energy dependent leakage from the galaxy. The neutrino spectrum follows the CR spectrum in the galaxy ($\gamma \approx 2.7 - 3.1$). This component is analogous to the diffuse gamma ray background from the galactic disc.
>
> **In the atmosphere:** Compared to interstellar targets the earths atmosphere is relatively dense. The competition between decay and absorption steepens the spectrum by about one power in energy ($\gamma \approx 3.7$). The details depend on the energy and the proper life time of the intermediate meson. The combined effect will be discussed in the next section.

It is this difference in the spectrum that allows to distinguish extraterrestrial diffuse fluxes from locally produced neutrinos. They carry the harder initial spectrum of the cosmic rays and should create an excess flux at high energies. The three classes are shown in the summary plot of neutrino fluxes (figure 2.5).

2.4 Guaranteed Neutrino Sources

Guaranteed sources are important test beams and background to the detection of candidate neutrino sources at the same time.

2.4.1 Atmospheric Neutrinos

The strongest among the guaranteed sources are atmospheric neutrinos. They are produced in showers induced by cosmic rays hitting the earths atmosphere. Neutrino production in dense media can be written as [16]:

$$\frac{dN_\nu}{dE_\nu} = \frac{N_0(E_\nu)}{1 - Z_{N,N}} \left(\frac{A_{\pi,\nu}}{1 + B_{\pi,\nu} \cos\Theta \cdot \frac{E_\nu}{\epsilon_{\pi\pm}}} + \frac{A_{K,\nu}}{1 + B_{K,\nu} \cos\Theta \cdot \frac{E_\nu}{\epsilon_{K\pm}}} + \ ... \right) \tag{2.5}$$

The parameters A and B normalize the contributions of the different mesons and their zenith angle dependence (θ = incident angle of the primary). Z characterizes the primary interaction.

The first term in the brackets describes the pion and the second the kaon contribution. The third term (dots) stands for heavier mesons. The formula shows that different channels contribute to the total flux and each channel has its own energy and angular dependence.

The zenith angle dependence is called the secant theta effect and is due to the fact that showers that hit the atmosphere under a larger angle have more time to develop in the dilute upper layers of the atmosphere. Therefore more pions and kaons can decay in flight. So more neutrinos are produced at the horizon than under vertical impact.

The balance between decay and absorption depends on the density of the target, i.e. the atmosphere, and the energy of the meson. The energy where the two processes are equally likely is called the critical energy. It is specific for the target and the meson type. For pions it is $\epsilon_{\pi^\pm} = 115$ GeV, for kaons $\epsilon_{K^\pm} = 850$ GeV and for charmed mesons $\epsilon_{D^\pm} = 4 \cdot 10^7$ GeV. Far below this energy the mesons decay without absorption and the neutrino spectrum follows the primary spectrum. Far above this energy the absorption probability rises with energy, i.e. range, and the spectrum steepens by about one power of energy.

Heavier mesons have shorter decay lengths and therefore decay. Absorption sets in at higher energies. Therefore the atmospheric neutrino flux is dominated by different components at different energies. The flux from pions and kaons is called conventional. It dominates the atmospheric spectrum from GeV to PeV energies. Because of the instant decay of the charmed mesons their contribution is called the **prompt component**. Since absorption is negligible its spectral index follows the primary spectrum and its zenith angle dependence sets in at much higher energies.

The absolute normalization uncertainty for conventional neutrinos at TeV energies is of the order of 30% whereas the shape of the spectrum is known as precise as 5% [17, 18]. The uncertainty is mainly due to the extrapolation of the cross sections over several orders of magnitude. The prompt neutrino flux at PeV-energies is known to an order of magnitude only. The energy where the prompt component starts to dominate is expected between 20 TeV to 1 PeV [19, 20, 21]. The total flux at these energies is too small to be detected with the data from the AMANDA-B10-detector analyzed in this work. The prompt component however, is a serious background for larger detectors because it shows the same spectral index as is expected from cosmic sources.

The final shape of the spectrum is given by a power law with spectral index 2.7 for energies smaller than 100 GeV where is steepens to 3.7. Somewhere between 20 TeV and 1 PeV the contribution of the prompt component with a spectral index of 2.7 is expected. The combined flux is shown in figure 2.5.

The parameterization for the conventional atmospheric neutrino flux discussed here was given in [16, 6]. The Monte Carlo used in this analysis, however, uses the parameterization given by Lipari [22]. The prompt component is neglected.

2.4.2 Galactic Neutrinos

Similar to the atmospheric neutrinos there is a neutrino flux expected when cosmic rays contained in the galaxy interact with interstellar gas. Because of the low matter density all secondaries (including muons) decay and produce neutrinos. The spectrum therefore is expected to follow the primary spectrum with $\gamma = 2.7$. The expected flux is shown in figure 2.5. It will be detectable with a km^2 effective area. For the AMANDA-B10 analysis it is negligible.

2.4.3 Cosmological Neutrinos

Cosmic rays with energies of up to 10^{20} eV have been observed. At these energies the GZK-mechanism [23, 24] predicts an enhanced absorption of protons by the cosmic microwave background radiation. The absorption process should produce neutrinos at very high energies. The expected fluxes for upgoing neutrinos are much too small for AMANDA-B10 since the earth is opaque at these energies. However, events from a neutrino with this energy could be seen in the down-going muons just by its outstanding energy. Investigations for AMANDA are underway [25].

2.5 Possible Neutrino Sources

The final object of interest are sources that are not guaranteed but might be there and that are more closely linked with the accelerators. Just for orientation the sources are divided in galactic and extragalactic.

The predictions for single sources are too low to be detected with AMANDA-B10. Even with km^2 scale detectors only the most optimistic models can be probed. The combination of many single sources, however, is expected to produce a diffuse flux detectable with much smaller detectors, with a harder spectrum than atmospheric neutrinos. The focus of this work is therefore the search for a diffuse excess of neutrinos at high energies. Even though a positive detection is not expected for AMANDA-B10, the various sources shall be introduced in order to motivate the development of the search technique. The combined flux is subject to the limits derived from gamma ray background and cosmic ray flux (at energies above the ankle). The sources will be introduced in this section and the associated fluxes and limits in the next section.

2.5.1 Galactic Sources

Even though the bulk of cosmic rays is believed to be produced in our galaxy, the predicted neutrino fluxes are generally very small. The main reason is the non-observation of the TeV gamma ray flux at a level expected from neutral pion production.

Supernova Remnants

As discussed in section 2.2 supernova remnants (SNRs) are the leading candidate for CR production in our galaxy. The only weakness of the picture is the missing TeV gamma rays expected from neutral pion decays in a proton accelerator [11] and [12]. Positive observations as for the Crab Nebula, SNR 1006 and Cassiopeia A can be explained with inverse Compton scattering of synchrotron photons from the relativistic electron-positron plasma. Even the optimistic fits to the Cassiopeia A observation [26] yield fluxes at the scale detectable with km^2 class detectors only.

Young SNRs could form a double shock front structure that could accelerate protons [27]. However, the decay time of the double shock front is between 1 and 10 years, limiting the numbers of source candidates. Besides that no indication for this scenario was observed from SN1987A.

Suggestions to solve the problem of missing TeV gamma rays from SNRs are discussed: for example the primary spectrum at the acceleration site may be steeper. Together with a smaller energy dependence of the leakage from the galaxy that would be consistent with the observed CR spectrum and result in a steeper γ-ray spectrum, i.e. a lower γ-ray flux at high energies. Another possibility is a selection effect of the observation. If the observed SNRs are younger than average and the spectra of young SNRs are steeper than average, for example due to the limited life time, there would be no TeV-γ rays yet but still SNRs could be the source of the galactic CR.

Pulsars

Pulsars are rapidly spinning neutron stars with extremely high magnetic fields ($P_{ns} \geq 1ms$, $B \approx 10^{12}G$). The resulting static electric field could accelerate iron nuclei ripped from one pole of the star to up to 10^{18} eV [3, 28]. Another possibility for proton acceleration could be a shock wave of electrons and positrons driven by the magnetic dipole radiation of the pulsar. But still pulsars are generally not believed to be strong CR accelerators because the protons would suffer adiabatic losses in the turbulent magnetic field an dense outer belt of electrons, positrons and synchrotron photons (plerion). A model suggested for the pulsar inside the Crab nebula by Protheroe and Bednarek [29] circumvents these losses by intermediate neutrons that are produced by pγ and "tunnel"the plerion. They then interact inelastically or decay in the outer SN shell under production of neutrinos.

X-ray Binaries and Micro Quasars

Another possible candidate for detectable neutrino fluxes are X-ray binaries. They consist of a black hole or neutron star with a companion. The first can accrete matter from the latter forming an accretion disk and jets very similar to active galactic nuclei (see section 2.5.2), just with about eight orders of magnitude less mass. They therefore are also referred to as "micro quasars"i.e. mini AGN. Acceleration may take place as for AGN and they might show electrostatic and dipole acceleration as discussed for pulsars. The model was motivated by a high flux measurement of Cygnus X3 [30]. The flux was corrected one order of magnitude down. Together with revised calculations the neutrino fluxes are below detection level [1].

2.5.2 Extragalactic Neutrino Sources

Active Galactic Nuclei (AGNs)

The most promising extra galactic neutrino candidates are active galactic nuclei (AGN). They are the most powerful single objects observed in the cosmos, as bright as an entire galaxy but extremely compact: A variability of flux doubling within days is common and a flux increase of an order of magnitude within hours has been observed [13, 31]. This degree of variability limits the size of the emission region to a volume of the size of the solar system. The spectrum ranges from radio to TeV gamma rays, with a prominent thermal luminosity peak in the ultra violet (peak at 40 eV) called the *blue bump*. The shape corresponds to a black body with surface temperature of $\sim 10^5$ K.

The small size and the high luminosity support the picture of gravitational power released by accretion. The unified AGN model therefore involves a super-massive black hole (10^8 solar masses) accreting matter from the host galaxy. The released energy of the infalling matter heats the inner part of the accretion disk resulting in the strong thermal emission. Along the rotation axis of the disk matter is ejected in so called jets (see figure 2.4). In these jets and in the accretion disk close to the black hole shock waves can form and accelerate particles. In the case of electron acceleration the gamma rays are explained by synchrotron radiation and inverse Compton scattering of the synchrotron photons. In the case of proton acceleration they are due to primary gammas from resonant neutral pion production ($p\gamma \rightarrow \Delta \rightarrow p\pi^0 \rightarrow p2\gamma$) and secondary electron-positron pair cascades in the dense photon field of the shock. However, if AGN accelerate protons along with the electrons they are good candidates to be the source of the high energy cosmic rays observed up to energies of 10^{20} eV. And if there are high energy protons they will produce charged pions as well ($p\gamma \rightarrow \Delta \rightarrow n\pi^+$) and thus neutrinos (see formula 2.4).

According to the possible locations of shocks two classes of models for neutrino production in AGN are distinguished: core models and jet models.

Core models (spherical accretion models) developed in the early nineties predicted relatively high neutrino fluxes [33, 34, 35, 36] of up to $4 \cdot 10^{-5}\ E^{-2}\ \mathrm{cm}^{-2}\mathrm{s}^{-1}\mathrm{sr}^{-1}\mathrm{GeV}$ between 1 and 100 TeV [35]. Generic core models consist of a black hole with spherical accretion at the Eddington limit where radiation pressure and gravitational pressure of infalling matter are in balance. The weakness of generic core models is a contradiction of the predicted X-rays to observation. Because of the intense UV field the acceleration region is optically thick to the gamma rays from resonant neutral pion production. The high energy gammas would create $e^{\pm}$-pair cascades. At energies below pair production threshold the core gets transparent and the photons escape. The result would be a non-thermal X-ray spectrum below the pair production threshold of about 500 keV. This contradicts the observation of a thermal X-ray spectrum with peak intensity at about 100 keV. Extensions to the generic models have been proposed but natural solution is the shift of the acceleration sites from the inner engine to the jets.

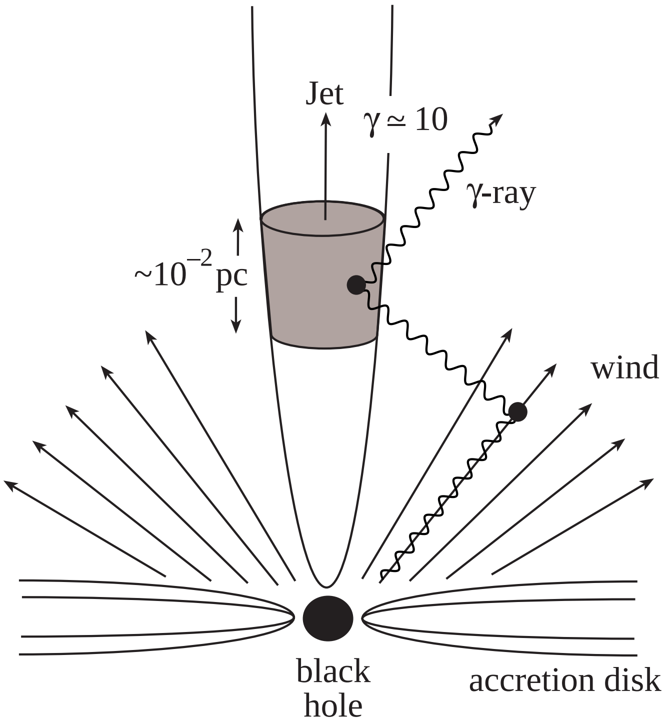

Figure 2.4: The blueprint of an active galactic nucleus (AGN) (taken from [32]).

Jet models: More recent models concentrate on shock acceleration in the jets. There is a large variety of combinations of primaries, target, shock location along the jet, and jet temperature: There are relativistic jets with coherent matter outflow as opposed to relatively slow matter flow that is accelerated by relativistic shocks running through the jet matter (hot/cold beams). As target thermal photons close to the accretion disk, synchrotron photons further down the jet or protons are discussed. Finally, one part of the models assume a Poynting flux driven electron-positron wind of the envelope of the black hole or a hydrodynamic flow of electron proton plasma from the relativistic inner accretion disk.

A recent review ([37] and references therein) is based on the discussion of observed properties such as

- the fraction of blazars among gamma ray sources
- the ratio of gamma ray to radio luminosity
- the spectrum features as breaks
- the cut off at TeV energies
- the variability of the luminosity.

It comes to the conclusion that only the hadronic models can explain all phenomena. Especially the observation of TeV gammas is hard to explain with electron-only models. Electrons are efficiently cooled by synchrotron radiation. A magnetic field low enough to fit the ratio of the low energy (radio to soft X-ray) intensity to the TeV intensity contradicts estimates from the size of the emission region. Another advantage of proton models is the efficient transfer of energy in the presence of magnetic fields from the central engine to the outer disk.

A special sub-class of AGN (~10%) are blazars: These are AGN with a jet pointing towards the earth, beaming a large fraction of their luminosity. Prominent examples are the nearby sources Mrk-501 and Mrk-421. Both have been observed as radio loud and up to TeV gamma energies but are relatively weak emitters. The observation at TeV energies constrains the acceleration regions to be Lorentz boosted by $\Gamma \approx 10$. A source with the same morphology but $\Gamma \approx 1$ would be opaque to gamma rays and protons that are both trapped by the intense photon field: it would be - transparent for neutrinos only - a hidden source. Other examples such as 3C-273 and 3C-279 are further away but stronger sources. A fit of blazar models to the observed CR spectrum is introduced in [38]. The associated neutrino fluxes for three different assumptions of the corresponding cosmic ray production are shown in figure 2.5.

Relative merits of proton and electron acceleration are a matter of debate - a detection of neutrinos would settle the issue. If blazars are the source of UHE CR, they most likely would resonantly photoproduce pions with the intense photon field at the source. In this case they would be visible in the neutrino sky.

Gamma Ray Bursts (GRBs)

Gamma ray bursts are often referred to as the most cataclysmic events observed in the cosmos. The discovery that the energy released by GRBs is just about the same as needed for the highest energy CR has lead to the speculation that GRBs could be the source of UHE CR [39] .

The signature are gamma ray flares (keV to MeV) that last between milliseconds and a few seconds. The typical time structure is a rise time as short as 10^{-4} s followed by an exponential decay. They are randomly distributed. Only recently optical counterparts have been identified. The powering process is widely unknown giving room to speculations. The short rise times limit the extension of the central object to tens of kilometers. This leads to the assumption that neutron stars are involved. The fusion of neutron stars or super-massive star collapses, so-called "hypernovae" are proposed as power supply [3].

Independent of the inner engine, the dynamics of the evolving shock wave are believed to be understood quite well and described by the so called fireball model [40]. It involves the ultra-relativistic ($\gamma \approx 10^2 - 10^3$) expansion of an electron-positron plasma that forms a shock wave, with the possibility of Fermi acceleration allowing for proton acceleration, pion production and finally high energy neutrinos. One remaining question is the origin of the accelerated protons if GRBs are sources for the high energy CRs.

2.5.3 Other Neutrino Sources

Electron Neutrinos - Glashow Resonance Besides the detection of muon neutrinos cascades of electron neutrinos can be detected. Because of the smaller mass the electron penetration power is much smaller compared to muons. Therefore the shower develops on much shorter longitudinal extension resulting in a nearly spherical light emission when observed from a distance of a few tens of meters. The angular reconstruction therefore is less precise. The main background are catastrophic energy losses of downgoing atmospheric muons. However, if there is a source of $\bar{\nu}_e$ with energies up to several PeV there is a prominent signal predicted. If the center of mass energy of the $\bar{\nu}_e$ with electrons at rest in the target matter reaches the W mass a resonance causes a strong increase of the cross section three orders of magnitude over the $\bar{\nu}_e - N$-cross section.

WIMP Annihilation A prominent class for dark matter candidates are weakly interacting massive particles (WIMPs). Because of their mass they are expected to accumulate in the center of cosmic objects such as the earth or the sun where they eventually annihilate. According to Supersymmetry models some of the decays include neutrinos. Depending on the WIMP-mass, the neutrinos may have energies large enough to be detected via vertically upward going muon tracks. The signature would be an excess of relatively low energy neutrinos close to the vertical direction.

Magnetic Monopoles Magnetic monopoles are particles that carry only one of the magnetic charges. These exotic objects may have been produced at the boundaries of phase transition regions during cosmological inflation. The magnetic moment influences the Cherenkov light intensity resulting in a factor 8300 more light compared to a single muon. The signature in an open Cherenkov detector would be extremely bright events with very continuous emission.

2.6 Diffuse Fluxes and Limits

It is certainly impossible to predict or constrain fluxes for hitherto unknown classes of sources only visible in the neutrino sky. The fluxes from candidate sources, however, can be constrained from gamma ray and cosmic ray observations. Even though individual sources are unlikely to be visible with detectors smaller than km^2, the cumulative flux might be detectable with much smaller detectors, especially since sources from the entire cosmos contribute and AGN at higher redshifts are thought to be more active.

Limits from gamma rays: In the case of proton acceleration neutrinos and gamma rays are produced in parallel. While neutrinos escape the source gamma rays cascade to lower energies in the source or scatter with the cosmic infrared background. However, the integral energy released in gamma rays and neutrinos is the same up to a factor two given branching ratio and kinematics at production. The diffuse gamma ray background above 30 MeV is observed to be $E_\gamma^2 dN_\gamma/dE_\gamma = (1.37 \pm 0.06) \cdot 10^{-6} \cdot E_\gamma^{-(0.1\pm0.03)} \mathrm{cm}^{-2}\mathrm{s}^{-1}\mathrm{sr}^{-1}\mathrm{GeV}$ [41]. With the factor two the neutrino flux is limited to a level of the order of $10^{-6} \cdot E^{-2}\ \mathrm{cm}^{-2}\mathrm{s}^{-1}\mathrm{sr}^{-1}\mathrm{GeV}$. In figure 2.5 this limit is represented by the horizontal upper edge of the shaded area.

Limits from cosmic rays: A similar energetic argument can be applied to the cosmic ray flux. For optically thick sources protons and neutrons are trapped in the intense photon field and only the gamma ray limit applies. Even if the source is optically thin protons will suffer adiabatic energy losses and do not constrain the neutrino flux anymore. However, neutrons may escape the source without energy loss and inversely β-decay outside. Waxman and Bahcall [42] assume $dN/dE \propto E^{-2}$ up to the GZK-cutoff and normalize at the ankle. As a result the energy released in neutrinos is limited to $E_\nu^2 d\Phi_\nu/dE_\nu \approx 10^{-8}\mathrm{cm}^{-2}\mathrm{s}^{-1}\mathrm{sr}^{-1}\mathrm{GeV}$.

Mannheim et.al. [43] argue that this is only valid stringently for sources that accelerate to energies around the ankle. Sources with lower energy cut off may contribute to the neutrino flux at lower energies without constraint from the CR flux at the ankle. Further they include evolution of AGN. The resulting limit is shown as the curved upper edge of the grey shaded region in figure 2.5.

Experimental limits to neutrino fluxes at energies above 100 GeV are rare. The only underwater Cherenkov detector operational is the BAIKAL telescope NT-200 [44]. Limits for electron and muon neutrinos have been derived at $E^2 dN(\nu_\mu)/dE \leq 1.4 \cdot 10^{-5}\mathrm{cm}^{-2}\mathrm{s}^{-1}\mathrm{sr}^{-1}\mathrm{GeV}$ (90% C.L.) [45, 46] and $E^2 dN(\nu_e)/dE \leq 1.9 \cdot 10^{-6}\mathrm{cm}^{-2}\mathrm{s}^{-1}\mathrm{sr}^{-1}\mathrm{GeV}$ (90% C.L.) [47]. Only recently a flux limit for muon neutrinos has been reported by the MACRO collaboration [48, 49] at $E^2 dN(\nu_e)/dE \leq 4.5 \cdot 10^{-6}\mathrm{cm}^{-2}\mathrm{s}^{-1}\mathrm{sr}^{-1}\mathrm{GeV}$ (90% C.L.). Together with limits presented from Frejus [50] and Flyes Eye [51] they are shown in figure 2.5.

The hidden source Finally there are suggestions for hidden sources (see [52] for example) where gammas as well as protons are trapped in a dense envelope of low energy photons. Due to their transient nature (1 year typical duration) they do not contribute to the diffuse gamma ray bound.

A lower limit: As opposed to all the limits discussed so far there is a lower limit to extragalactic neutrino fluxes as well. Storage of cosmic rays in galaxy clusters may lead to multiple interactions of the cosmic rays with intergalactic matter and photons. The result of an estimation given in [53] is shown as the lower edge of the grey shaded area in figure 2.5.

Averaging the logarithm of the two upper limits derived by Mannheim et.al. [43] and Waxman and Bahcall [42] one gets a flux of

$$\frac{d\Phi_\nu}{dE} \approx 10^{-7} \cdot\ E^{-2}\ \ \mathrm{cm}^{-2}\mathrm{s}^{-1}\mathrm{sr}^{-1}\mathrm{GeV} \qquad . \tag{2.6}$$

This may be taken as a *benchmark* flux where neutrino telescopes start to contribute to the understanding of cosmic accelerators.

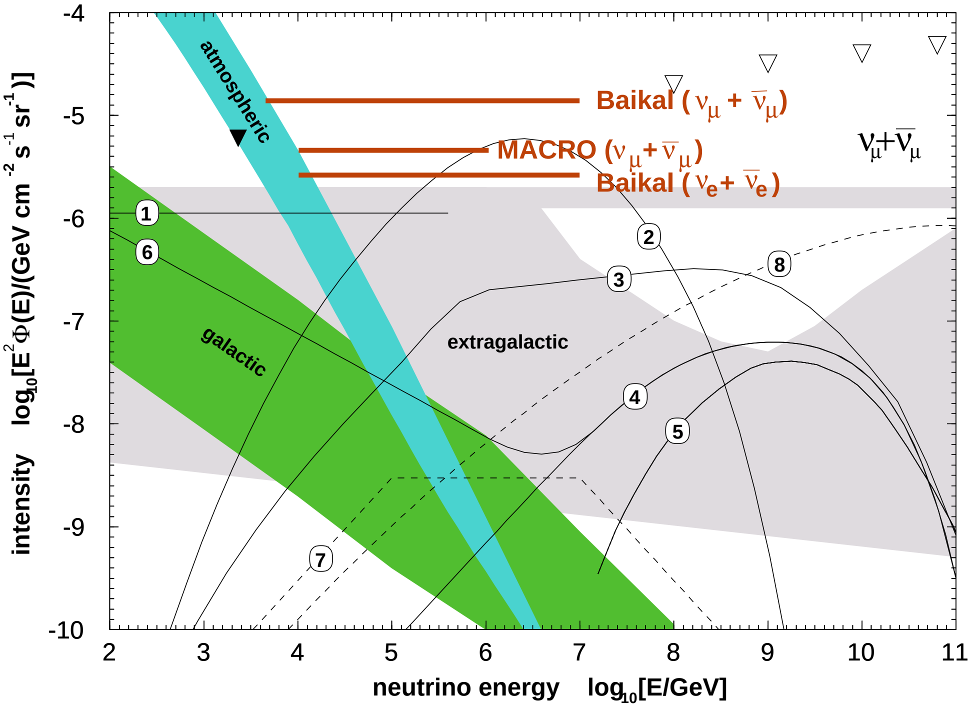

Figure 2.5: **Muon neutrino fluxes and limits** (taken from [3], for details see text). The shaded regions represent secondary fluxes. The graphs represent emission models. **Shaded bands:**The upper/lower bound of the atmospheric neutrino band represents horizontal and vertical direction. The upper/lower bound of the galactic band represents the intensity from the center / the poles of the galaxy. The upper/lower edges of extragalactic band represent the upper limits from gamma rays (straight upper edge), cosmic rays (curved upper edge) and the lower(!) limit derived from cosmic rays in galaxy clusters (lower edge). **Models:** AGN core models (1 = pp [36], 2 =pγ [34]), AGN jet (blazars) models (3,4,5,6 = [38]), GRBs (7 = [39]) and topological defects (8 = [54]). **Experimental limits:** BAIKAL limit for ν_μ [46], BAIKAL limit for ν_e [47], Frejus (filled triangle = [50]) , Flyes Eye (open triangle [51], MACRO limit for ν_μ [49]).

Chapter 3

Detection of High Energy Neutrinos

3.1 The Detection Principle

High energy neutrinos can be detected by the observation of upward moving leptons in underground detectors. Only neutrinos can cross the entire earth and produce upward going leptons. Since it turned out that detectors in underground laboratories are too small to detect the feeble fluxes of extraterrestrial high energy neutrinos, expandable detectors in open media like water or ice are built. Here muons generated in charged current interactions are detected by the Cherenkov light they emit. Far above the threshold energy, the emission angle is constant, resulting in a Cherenkov light cone around the track. By reconstructing the cone the direction of the muon can be measured. For high energies the muon is nearly collinear to the neutrino. This allows to distinguish between muons created by primary cosmic rays hitting the atmosphere above the detector and muons created by upward moving neutrinos. The energy can be estimated from the amount of light due to secondary processes. This way relatively hard spectra due to cosmic accelerators can be distinguished from neutrinos created in the earths atmosphere.

Neutrinos create charged leptons in a charged current reaction as

$$\begin{aligned} \nu_l + N &\longrightarrow l^- + X \\ \bar{\nu}_l + N &\longrightarrow l^+ + X \quad . \end{aligned} \tag{3.1}$$

At high energies the lepton carries about half the energy of the neutrino. Therefore the direction of the lepton is close to the direction of the initial neutrino. The square root of the mean scattering angle is given by

$$\sqrt{< \theta^2_{\nu\mu} >} = \sqrt{m_p/E_\nu}[rad] \tag{3.2}$$

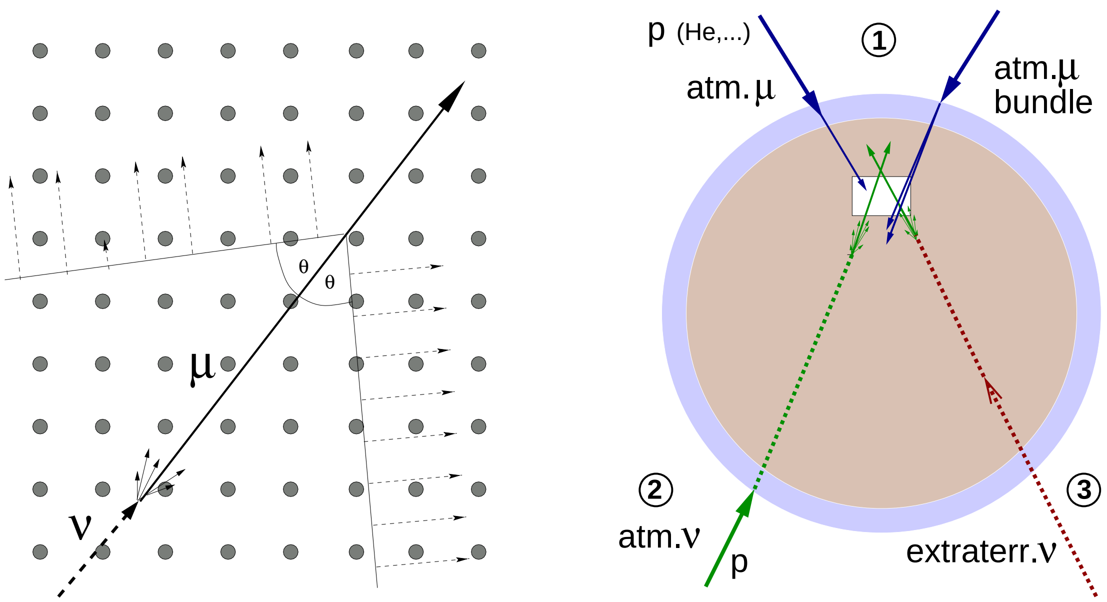

Figure 3.1: Left: A relativistic muon emits Cherenkov light, creating a cone that can be measured with a grid of photo-multipliers. Right: Event classes in underground muon detectors: 1. downgoing atmospheric muon background, 2. neutrinos created in the atmosphere and 3. cosmic (extraterrestrial) neutrinos.

corresponding to about 1° at $E_\nu = 3$ TeV.

The reconstruction of the light cone can be done by recording the arrival times of the wave front of the Cherenkov cone with a lattice of photo sensors in a transparent target medium. This is sketched in two dimensions in figure 3.1 .

High energetic muons are extremely penetrating. Even in water or ice at TeV energies they reach path lengths in the order of kilometers. Up to a few TeV the range rises linearly, afterwards logarithmically. The long path length allows to observe not only muons created in the detector volume but as well tracks created before the detector. Further the long track allows a good angular reconstruction. Therefore muons are the generic candidates for neutrino astronomy at TeV - PeV energies.

3.2 The Cherenkov Effect

If a charged particle moves in a medium with speed larger than the speed of light in the medium ($\beta \geq 1/n$) it emits Cherenkov light. The light is emitted under a characteristic angle. In this way the particle creates a moving light cone that points in the direction of the particle.

The emission angle follows as the ratio of the speed of light in the medium and the particle speed:

$$\cos\alpha = \frac{1}{\beta \cdot n} \quad , \tag{3.3}$$

where n is the refractive index. For water, and in the range from 300 to 600 nm, it can be treated as constant, n = 1.33. For ultra relativistic particles the expression reduces to 1/n and the Cerenkov angle is constant, $\alpha = 41.2^\circ$. The velocity condition can be written as energy condition. The threshold energy is

$$E_{Ch} = \frac{m}{\sqrt{1 - 1/n^2}} \quad , \tag{3.4}$$

where m is the mass of the charged particle. For the muon mass of 105.7 MeV the threshold energy is 162 MeV. This energy corresponds to a track length of about 80 cm. For all tracks of interest this condition is always fulfilled. The number of emitted photons is given by

$$\frac{d^2N}{dxd\lambda} = \frac{2\pi\alpha z^2}{\lambda^2}(1 - \frac{1}{\beta^2 n^2}) \quad . \tag{3.5}$$

In the range of 300 to 600 nm this is about 214 photons per cm track length. The energy loss due to the Cherenkov effect is

$$\frac{d^2N}{dxdE} = \frac{\alpha z^2}{hc}\sin^2\theta_c \tag{3.6}$$

For muons with z=1 this is $\approx$ 400 eVcm^{-1}. This is less than a percent of the minimum energy loss due to ionization of about 2 MeVcm^{-1}. The amount of light emitted is independent of the energy of the lepton. Therefore the energy cannot be measured by the amount of light from the single track but only from additional light from secondary tracks and showers.

3.3 Neutrino Cross Section

The detection probability for neutrino induced muons depends on the neutrino-nucleon cross section and the energy transfer to the muon because this determines the range of the muon and therefore the observed volume.

The neutrino converts to a muon in a charged current interaction. The cross section for a muon neutrino of energy E_ν and a nucleon of mass M_N is given by [55]

$$\frac{d^2\sigma_{\nu N}^{cc}}{dxdy} = \frac{2G_F^2 M_N E_\nu}{\pi} \cdot \left(\frac{M_W^2}{Q^2 + M_W^2}\right)^2 \cdot \; [xq(x,Q^2) + x(1-y)^2\bar{q}(x,Q^2)] \; , \tag{3.7}$$

where $-Q^2$ is the invariant four-momentum transfer, $q(x, Q^2)$ and $\bar{q}(x, Q^2)$ the parton distributions for quarks and anti-quarks, G_F is the Fermi constant and M_W is the mass of the W-boson. x and y are the Bjorken scaling variables. x is the fraction of the nucleon momentum carried by the quark and y fraction of the neutrino energy transferred to the quark:

$$x = \frac{Q^2}{2M_N(E_\nu - E_\mu)} \quad \text{and} \quad y = \frac{E_\nu - E_\mu}{E_\nu}\ , \tag{3.8}$$

The neutrino-nucleon cross section as a function of the neutrino energy is shown in figure 3.2. The cross section rises with energy up to about 10^4 GeV where the four-momentum transfer reaches the order of M_W^2 in the denominator, causing a smaller increase of the cross section. At low energies the cross section for anti-neutrinos is about a quarter of the one for neutrinos, but at high energies the cross section is dominated by interactions with sea quarks rather than valence quarks and the cross sections become equal. The energy transferred to the muon is given by $1 - y$. The energy dependence of the average momentum transfer to the quark $< y >$ is shown in figure 3.2. For energies $-Q^2 >> M_W^2$ it starts to fall, corresponding to an increase of the momentum transfer to the muon. This results in a longer muon range, compensating the reduced rise in cross section slightly. For the simulation of neutrino-nucleon interactions in this work the cross sections as given in [56] are assumed.

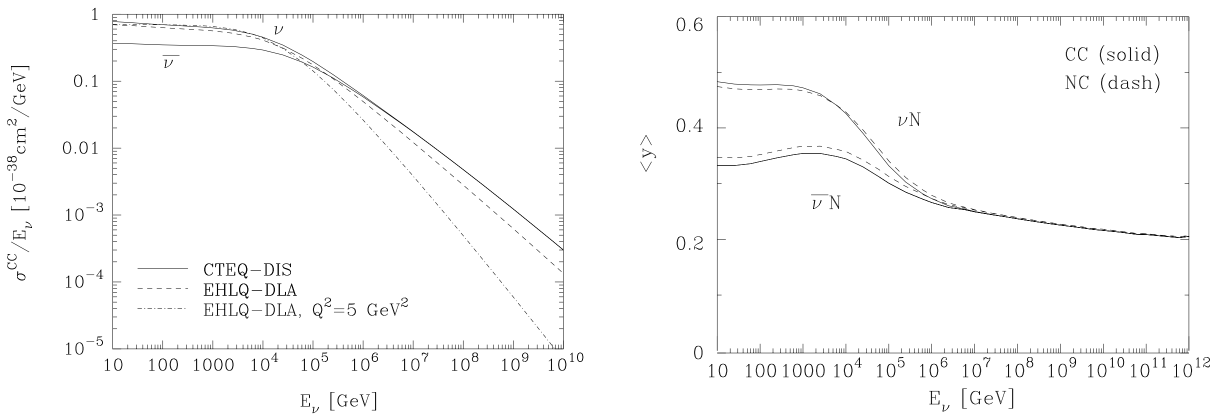

Figure 3.2: Left: Charged current cross section for neutrinos and anti-neutrinos. Right: Average energy transfer from the neutrino to the quark. Figures taken from [55].

3.4 Muon Detection

The energy loss of the muon during propagation is important for the detection in two ways: First it determines the muon range and therefore the effective volume of the detector: tracks produced far before the detector can range into the instrumented volume where they are detected. And second the energy loss processes create secondary particles that emit additional Cherenkov light.

3.4.1 Energy Loss

A muon passing through matter looses energy due to four interaction processes: Ionization (including δ-electrons), bremsstrahlung, pair production and hadronic interactions. The energy loss due to ionization is nearly independent of the muon energy and occurs continuously along the track. The energy loss due to the other three effects is about proportional to the muon energy. Their deposition fluctuates strongly up to catastrophic energy losses, i.e. deposition of almost the complete energy of the muon in one interaction. The energy loss can be approximated by

$$\begin{aligned} -\frac{dE}{dx} &= \left(\frac{dE}{dx}\right)_I + \left(\frac{dE}{dx}\right)_{B+P+N} \\ &= a(E) \quad + \quad b(E) \cdot E \end{aligned} \tag{3.9}$$

where x is the path length in g $\cdot$cm^{-2}. The coefficient a(E) describes the energy loss due to ionization including delta electrons and is given by the Bethe-Bloch formula (for example [57]). For minimum ionizing particles $a(E)$ is about 2 MeVg^{-1}cm^2, corresponding roughly to 2 GeV m^{-1} for ice. The coefficient $b(E)$ describes the three types of stochastic energy losses:

$$\begin{aligned} b(E) &= b_B + b_P + b_N \\ &= (1.7 + 1.3 + 0.4) \cdot 10^{-6} \mathrm{g}^{-1} \mathrm{cm}^2 \end{aligned} \tag{3.10}$$

For a muon of about one TeV energy in ice, this is about 3 GeVm^{-1}. The critical energy is defined as $E_c = a(E)/b(E)$, i.e. the energy where the stochastic energy loss exceeds the continuous one. Since the Cherenkov energy loss is constant above a threshold energy, the critical energy marks the energy where an excess in light can be used to determine the energy of the particle. In ice it is about 600 GeV for muons. Below this energy the range rises linearly, above logarithmically.

3.4.2 Light Production

The number of secondary tracks and therefore the amount of light emitted by a shower scales about linearly with the energy of the shower. Since the Cherenkov angle is constant and the secondaries are strongly boosted in the direction of the muon, the Cherenkov light from secondaries is emitted with about the same angular dependence. That means it is peaked at the Cherenkov angle.

Below the critical energy the light production is about constant at $\approx$ 220 photons per cm. The light production due to small showers from delta electrons increases the number of photons to 250 photons per cm. There is no way to measure the energy by means of light intensity. However, above 1 TeV the light from secondary processes exceeds the amount of light emitted from the single muon. The increased amount of light increases the distance from where a track can be observed. The fit of the light radius allows an energy estimate. Another more simple measure for the energy is the number of hit OMs. Energy estimators will be discussed in detail in chapter 6 and 7.

Another way to measure energies could be the measurement of the track length. However, this method is limited by the extension of the detector to energies close to the threshold of the detector.

3.4.3 Background

The main background for muons from neutrino interactions are down going atmospheric muons. They are produced by cosmic rays hitting the atmosphere above the detector and penetrate several kilometers in the earth shell. At sea level, there are about 10^{11} times as many atmospheric muons as upward going neutrino induced muons. At 1000 m water equivalent, the ratio reduces to 10^6 and at 4000 m.w.e. it is 10^4. Therefore neutrino telescopes are buried deep underground.

Another unavoidable background to extraterrestrial neutrinos are neutrinos created by cosmic rays in the atmosphere (at the other side of the earth). Being a background to the astronomical measurement they are an important test beam at the same time. Their angular distribution is nearly the same as expected for diffuse extraterrestrial fluxes.

Together with the extraterrestrial signal, the two background classes are shown in figure 3.1. The separation of neutrino induced events from atmospheric neutrinos is achieved by selecting only upward moving tracks (zenith angle cut). The extraterrestrial diffuse neutrino fluxes can be separated from atmospheric neutrinos only by their energy: the latter have a steeper spectrum ($\gamma \approx 3.7$) while a generic accelerator spectrum is assumed to have a spectral index $\gamma \approx 2$ (see section 2.4.1). This requires an energy estimator. For point sources the direction can be used as additional separation.

For extremely high energies (PeV) the separation scheme changes again. At these energies the earth becomes opaque and neutrinos can only be observed in horizontal direction. The fluxes at these energies are so small that this is not relevant for AMANDA-B10. However the proposed km^2 scale detector IceCube will be affected by the shadowing effect of the earth.

3.5 Existing Detectors

The principle of water Cherenkov detectors has successfully been used to detect neutrinos by a number of experiments. Kamiokande and IMB are two of the experiments that observed neutrinos from the Supernova SN1987A [58, 59] and are based on Cherenkov detection in a water tank. Super Kamiokande and SNO precisely measure solar and atmospheric neutrinos establishing neutrino oscillations [60, 61] and thus a finite neutrino mass. The separation of neutrino induced events from cosmic ray muons is based on the selection of contained events as well as upward going muons entering the detector from outside.

However, even the most optimistic models expect an excess of extraterrestrial neutrinos over atmospheric neutrinos only for energies of a few TeV. There, the fluxes in total are so low that closed detectors are just too small to collect enough events. On the other hand the long path length of muons allows to build much more sparsly instrumented detectors with a much larger detection volume. Open Cerenkov detectors in water or ice have typical OM-spacings of O(10 m). This is a compromise between detection accuracy and observed volume. The detection principle in an open medium has been investigated first by DUMAND [62, 63]. After a test phase and the successful detection of down-going events it was terminated in 1996 due to technical reasons.

Atmospheric neutrinos with energies between tens of GeV and a few TeV have been isolated from down-going background by the Baikal-collaboration [44, 64]. The Baikal-detector is located in the Siberian Lake Baikal. It is operational since six years and consists of 192 optical modules in eight strings. Flux limits on high energy electron and muon neutrinos have been derived (see section 2.6).

AMANDA is the largest detector currently taking data. It uses the Antarctic ice as target medium and has a detection area of a few 10^4 m^2. Being the topic of this thesis - the detector will be described in the next chapter in detail.

Two other detectors with instrumented volumes similar to AMANDA are ANTARES [65] and NESTOR [66]. They are planned to be installed in the Mediterranean. ANTARES has conducted first data taking with a demonstrator string. The deployment of a first stage detector with 10 strings is planned for 2002-2004.

The largest detector currently under consideration is IceCube. It is planned to have a physical extension of a cubic kilometer at the same location as AMANDA. The expected performance of this detector has been investigated and is presented in [67, 68, 69, 70]. Based on these results a more detailed analysis has been developed by H. Wissing. It is described in [71, 70, 72, 73].

Chapter 4

The AMANDA-B10 detector

The AMANDA detector is located at the geographic South Pole. It uses the Antarctic glacier ice as target material. It consists of a matrix of optical sensors (optical module, OM) mounted along so called strings that consist of cables for power supply and signal transmission. By now AMANDA consists of 19 strings. The detector used in this analysis is the first subdetector of ten strings at a depth of 1500 to 2000 m.

In spite of the impressive extension of the detector, one of the main goals is to investigate the feasibility of a much larger detector. While probing only the most optimistic models, the focus is on the test of a variety of technical solutions. The heterogeneous design of the detector is a result of this purpose.

4.1 Deployment History

The structure of AMANDA reflects the stages of installation. During the austral summer 1993/94 the first four strings with 20 modules each were deployed at a depth of 810 to 1000 m. The ice at this depth turned out to contain much more bubbles than expected, making track reconstruction impossible. This part is referred to as AMANDA-A and is used in coincidence with AMANDA-B for systematic studies.

The next 4 strings with 20 modules each were deployed in 1995/96 at depth between 1520 and 2000 m (AMANDA-B4). The ice quality at this depth is much better allowing track reconstruction, and first neutrino events could be separated [74]. In 1996/97, six additional strings with 36 OMs each were deployed, forming AMANDA-B10. This detector consists of 302 optical modules. The total hight is about 400 m and the radius 60 m. The vertical distance between modules of the same string is 10 m. The data taken with this detector in 1997 were used for the analysis presented in this work.

Until now two more extensions have been built: in 1997/98 three more string at a radius of about 100 m were deployed. In 1999/00 the last six strings were added. The 19 strings between 1400 and 200 m form the detector AMANDA-II that is currently taking data. A schematic drawing is shown in figure 4.1.

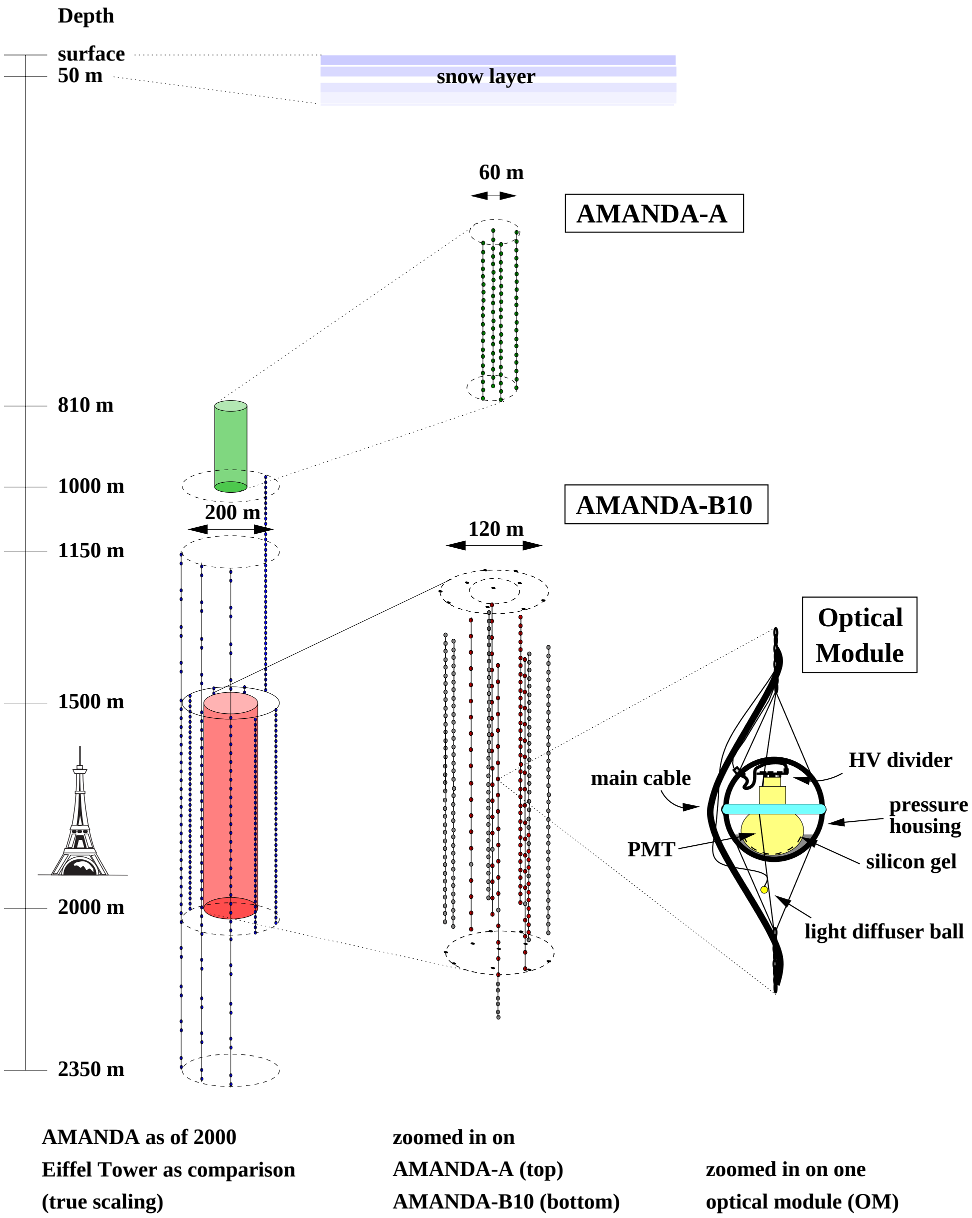

Figure 4.1: Schematic view of the AMANDA detector.

4.2 The String Structure

The largest substructure of the detector is a string. It consists of a super-cable that supports the optical modules. The super-cable consists of a set of cables, one for each module. Besides the electrical cables for power supply there are optical fibers for time and position calibration. The currently used module type is supplied with high voltage from the surface. The signal is transported to the surface as short pulse on the same cable. Dispersion in the cable leads to a smearing of the pulse. Near pulses therefore merge together and result in a bad double photon resolution. Newer designs intend to use optical fibers for signal transmission. As test for the optical transmission, the last eight strings have been equipped with optical and electrical transmission electronics. An alternative is the signal digitization in the OM. This requires much more electronics in the ice and therefore long term stability of the components. The Digital Optical Module (DOM) has been chosen as the IceCube baseline technology in March 2001. Lasers in the ice are used to investigate the ice quality.

4.3 The Optical Module

The basic structure of the detector is an optical module (OM). It consists of a glass pressure vessel containing a photo multiplier (PMT) and basic electronics. AMANDA uses 8-inch photo tubes with 14 dynodes in order to reach a gain of 10^9. For the first generation optical module there is no amplification in the module but the pulse is picked from the HV-supply cable at the surface. Even though the pulse is smeared out to 600 ns (FWHM) and a rise time of about 180 ns, a time resolution of about 5 ns is reached. The dark noise rate of the module is 0.6 (1.2) kHz for string 1-4 (5-10) caused mainly by the Potassium content of the glass sphere. The PMT is glued with a gel to the housing in order to establish good optical contact.

4.4 Electronics and Data Acquisition

Electronics

The digitization of the data happens at the surface. The pulse is separated from the HV, amplified and multiplexed three-fold with one copy with a defined delay. The first of the prompt copies enters a discriminator that is fed into a multiplicity trigger logic. The second is fed into a time to digital converter (TDC) for time measurement. The delayed signal is read out by an analog to digital converter (ADC) that delivers the pulse height. The delay time is tailored to fit the trigger decision time.

Trigger

The array is triggered by a simple multiplicity trigger, 14 or more hits are required within 2.5 μs. This time is chosen close to the time a muon needs to cross the detector. If released, the trigger causes a common stop. TDCs and ADCs are blocked from new hit information and read out. Afterwards they are reset and freed for reading the next event. The trigger rate is dominated by down-going atmospheric muons and is about 100 kHz. A few percent of the events are due to triggers from experiments on coincident observations such as SPASE [75], an air shower array on the ice surface, and RICE [76], a radio antenna array, and AMANDA-A.

Data Acquisition

The TDCs register leading and trailing edges for up to eight pulses. The amplitude of the highest pulse is digitized. Each event gets a global time stamp. The time collection time window is 32 μs, and the ADC collection time window 4.2 μs centered around the trigger time. The data stored on magnetic tape sum up to over a terra byte per year. Only a fraction is transferred via satellite. The complete data is transported to the northern hemisphere after opening of the station in the austral summer.

4.5 Calibration

In order to reconstruct the Cherenkov cone, the position of the optical module and the arrival time of the photon are needed. The latter requires the exact knowledge of the transit time of the signal starting with the photon arrival time and ending with the digitization. These calibrations are referred to as geometry calibration and time respectively. For both calibrations a variety of light sources at the surface and in the ice are used.

Time Calibration

For the time calibration, every module of the first four strings and every second module of the strings later deployed is equipped with a diffuser ball (about 1 cm in diameter) that can be illuminated through fibers from a YAG-laser at the surface.
The round trip time can be measured and the light propagation time in the cable and the ice is subtracted. The fiber transit time is determined from reflections at the connection between fiber and diffuser. The threshold crossing time depends on the amplitude of the pulse. This is corrected for using the ADC-information ($\approx 1/\sqrt{ADC}$). The time calibration reaches an accuracy of a about 5 ns.

In an alternative approach, down-going muons are reconstructed using all strings but one. The light arrival time for modules in the unused string is compared to expectation based on the initial t_0 values, and a correction to these values is applied. This correction procedure is repeated over several iterations. It results in considerably improved t_0 values. This methods is especially of interest for Ice Cube because it requires no extra data taking, can be done continously over the year and allows to calibrate strings over much larger distances than the method based on artificial light sources.

Geometry Calibration

The position of the modules can be inferred from the deployment information, inter-string light measurements and from the analysis of down-going muons.

The first method is based on the logs of the drilling and deployment. The nozzle of the drill is equipped with tiltmeters that register the direction of the drill. Together with the depth-information, the hole position is known to an accuracy of a few tens of centimeters. During deployment the depth of the modules is recorded yielding a seed for the latter methods.

The second method is the standard procedure until now. The diffuser balls mentioned above can be used to emit light at a known position that can be seen from the modules in the same string and modules in neighboring strings. From the arrival time the distance between strings and between modules along a string can be inferred. The accuracy of this method reaches a few tens of centimeters corresponding to the same order of accuracy as the time information.This method has proven to be reliable but requires dedicated measurements causing an effort feasible only during summer.

ADC Calibration

Since pulses with only one photo electron by far outnumber the down-going muon background minimum bias data can be used to fit the one p.e. position of the individual OM. At present the dynamical range is limited to 5-10 photo electrons due to the high gains used.

4.6 Optical Properties of the Ice

The optical properties of the detection medium determine the track reconstruction algorithms and their accuracy. They are characterized by the scattering length, the mean scattering angle, and the absorption length. In AMANDA, these parameters are derived from the distribution of the arrival times of single photoelectron pulses over distances of a few tens of meters. The light sources used for these measurements are the diffuser balls as well as other dedicated light sources in the ice. These sources emit light at different wavelengths (some with tunable wavelength). They allow to determine the optical properties as a function of wavelength and of depth.

Averaged over depth, and for wavelengths below 450 nm, the absorption length λ_{abs} is about 95 m. The scattering length is usually normalized to the case of isotropic scattering, yielding an *effective* scattering length $\lambda_{eff} = \lambda_{scatt}/(1 - cos\theta)$ (where θ is the mean scattering angle). Averaged over all depth, $\lambda_{eff} = 24m$ for AMANDA (but strongly varying with depth, see figure 4.2). The decrease of the photon density with increasing distance from the light source is described by the attenuation length, which is derived from both the effect of scattering and absorption. For AMANDA it is about 27 m.

Compared to water (as the alternative target material for an open Cherenkov detector) ice has a short scattering length and a long absorption length, whereas water has nearly no scattering but a higher absorption. Generally speaking this leads to a better direction reconstruction in water because the direction information is contained longer, and a better energy reconstruction in ice because the path length in the detector is larger. However, the attenuation lengths differ by a few percent only.

The scattering delays photons and results in a non-Gaussian, asymmetric distribution of the arrival time, with long tails toward large delays. Therefore the simple χ^2 reconstruction is replaced by a likelihood fit, with a likelihood function which takes into account the delays. This function was tailored to the "average"parameters, and does not take into account the variations of parameters as shown in figure 4.2 (For details see section 5.2.2). The vertical variations have been however included – in an approximated way – in the detector simulation. For more details see section 5.1.4.

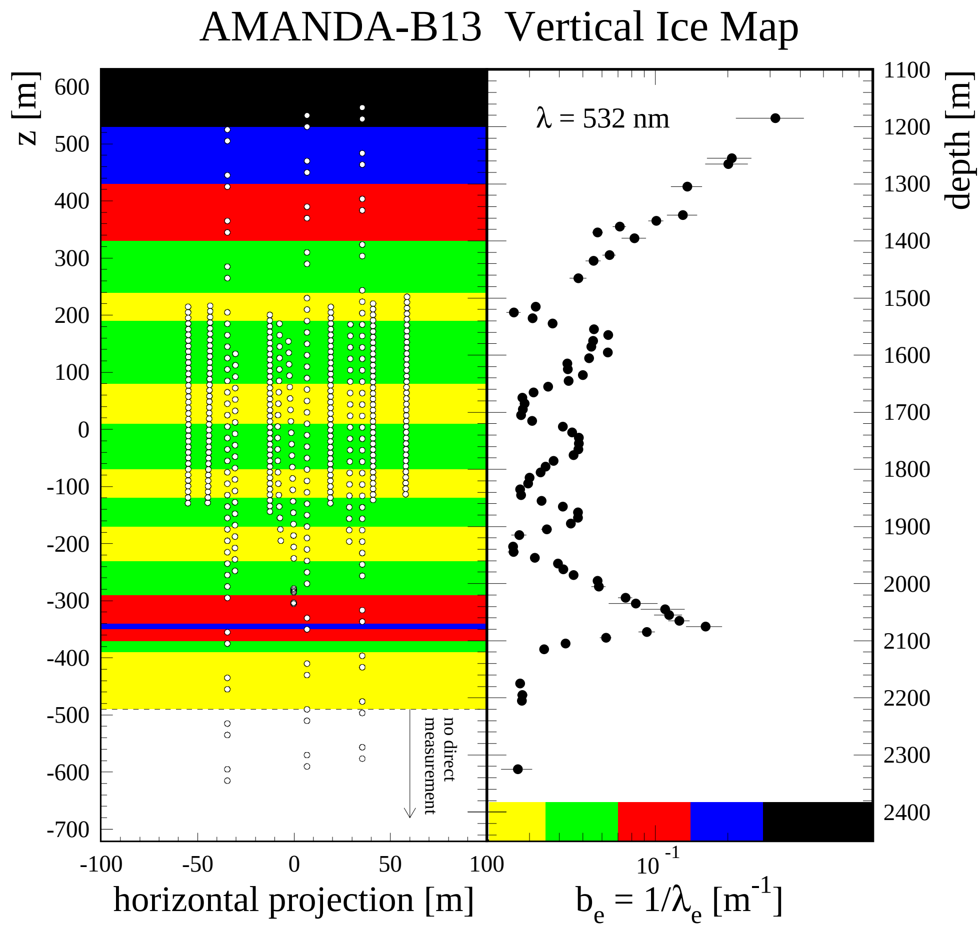

Figure 4.2: Depth dependency of the effective scattering length of the ice. For comparison the position of the optical modules is plotted left. Clearly visible are layers of increased scattering, three of which within the instrumented depth.

4.7 Experimental Data Set

The data used in this analysis were taken in 1997 between April 5th (day 95) and November 15th (day 319). The total data taking time sums up to 202 days. The run selection is based on the number of stable modules. A module is considered stable if its noise rate is within two (OM #1-80) or four (OM #81-302) standard deviations of its whole year average noise rate. The array consists of 302 modules. About 260 of them have stable periods. A run is considered stable if 220 or more out of the 260 modules are stable. Only stable runs were used in this analysis. After dead time subtraction and run selection 130.1 days uptime remain.

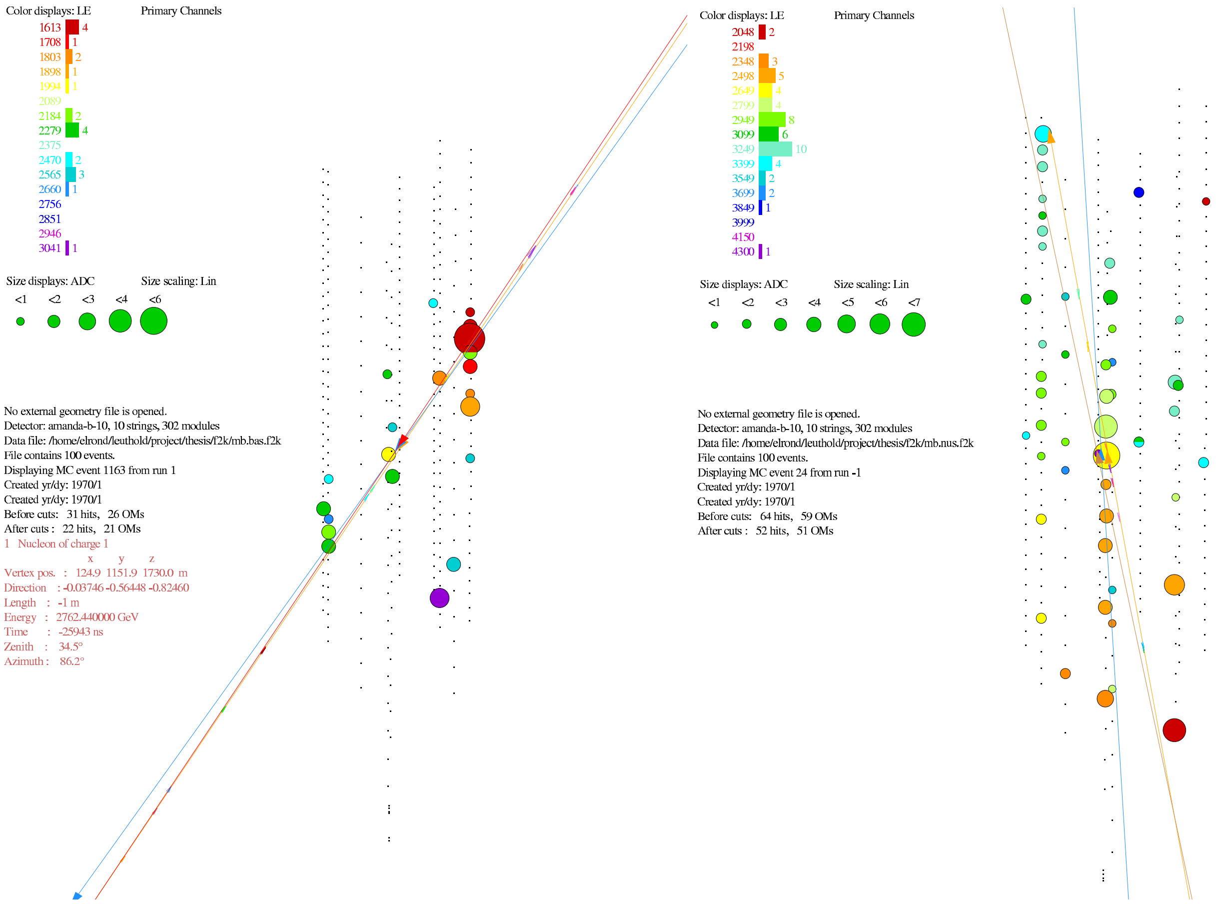

Figure 4.3: Typical events in AMANDA. The arrival time of the photons is coded in rainbow colors. Early hits are represented in red, late hits in blue. The straight lines represent the true track and the result of two different track reconstructions. Left: Typical down going event. The time flow points clearly downward. Right Typical high energy (500 GeV) upgoing event.

For illustration two typical MC events are shown in figure 4.3. The sparsely instrumented detector registers on average 20 hits for neutrino events. For track reconstruction the number of unscattered photons is more important, being about one third of the total number of hits (for details see section 5.2.2).

Chapter 5

Analysis Tools and Methods

After the detector and the data set have been introduced in the previous chapter, the technical aspects of the analysis will be discussed in this chapter. The application of the tools and methods to separate neutrinos and search for a high energy component, will be described in the two subsequent chapters.

In order to understand the complex detector response signal and background were simulated with high statistics. The used simulation packages along with their underlying physics principles are described first. After that, the used reconstruction methods and the typical cut parameters will be described. For the development of the higher filter levels a cut optimization tool was used. It will be introduced in section 5.3. The final cut on the energy parameter determines a limit or a flux measurement. In order to avoid an observers bias, the last cut was placed according to the method of average upper limits. The method will be discussed in the last section of this chapter.

5.1 Monte Carlo Simulation

For the modellation of the detector response large amounts of Monte Carlo (MC) data were used. However, with 10^9 triggers per year it has not been possible to simulate as many events as have been registered. In order to describe the background at higher cut levels importance sampling techniques were used. A total of about 10^8 triggers have been simulated. Due to the zenith angle and energy dependence of the importance sampling the precise simulated uptime depends on the selection level. It is in the order of days.

The signal MC includes weights that allow to describe the atmospheric neutrino response as well as the response to various other energy spectra, as expected from extraterrestrial sources. At final cut levels the precision of signal MC is much higher than that of the background MC, because the background MC is much more strongly filtered (10^{-6}).

In order to investigate systematic uncertainties, a set of signal MC variations have been produced. Due to computing time limitation it was not possible for background MC.

5.1.1 Event Generation

Muon Background

The main background are downgoing muons created by cosmic rays in the atmosphere above the detector. This may be single muons or muon bundles from a single air shower. Two generators were used: for the majority of the statistics the fast generator `basiev` [77], for a systematic comparison the detailed and time intensive generator `corsika` [78].

- With `basiev` about $8 \cdot 10^7$ triggers were generated. As primaries only protons are taken into account introducing an approximation in the muon multiplicities. An isotropic flux with differential spectrum $dN/dE \propto E_\mu^{-2.67}$ is assumed. The maximal simulated energy of the primary is 1 PeV. Important sampling was used to improve the precision on higher cut-levels.
- With `corsika` about 10^7 triggers were generated. This generator was developed for the air shower experiment KASCADE [79]. The isotope composition of the primary spectrum and the different spectral indices of the individual components are taken into account as input to `corsika`. The hadronic interaction of the primary particle with the atmosphere is simulated in detail, yielding a more precise muon multiplicity and momentum distribution. Further, primary energies of up to 10^{20} eV can be simulated. However, the detailed simulation requires more computing time. Therefore, a relatively low statistics sample is used, mainly for comparison to the results obtained with the `basiev`-sample at low filter levels.

The simulated muons are propagated to the ice surface.

Neutrino Signal

Atmospheric and extraterrestrial neutrinos were generated with the generator `nusim` [80]. A number of signal variations have been simulated for systematic checks.

- With `nusim` about 10^6 triggers with neutrino energies between 10 and $10^{5.5}$ GeV and $5 \cdot 10^5$ triggers with energies between $10^{5.5}$ GeV and 10^8 GeV were generated. This generator provides weights that allow to reweight the events, in order to consider different source hypotheses. This way the same sample can be used to describe the atmospheric neutrinos and the extraterrestrial neutrino spectra. In the case of atmospheric neutrinos the angular dependence of the neutrino generation process is taken into account. The flux as given by Lipari [22] was simulated. The neutrino-nucleon interaction is simulated according to the cross section as given in [56]. Absorption and neutral current scattering of neutrinos in the earth is taken into account. For the extraterrestrial neutrinos an E^{-2}-spectrum was assumed. For convenience in the documentation the simulated flux was chosen relatively high: $dN/dE_\nu = 10^{-5}\ E^{-2}\ \ \mathrm{cm}^{-2}\mathrm{s}^{-1}\mathrm{sr}^{-1}\mathrm{GeV}$.

The muons are stored for propagation at their production vertex, if it is in the ice. If the vertex location is in the rock below the ice, the mouns are propagated to the border between bed rock and ice.

5.1.2 Muon Propagation

After generation the propagation of the muons is simulated with `mudedx` [81]. The propagation starts at the ice surface or the bed rock, and tracks the muon to the detector and through the entire instrumented volume. Stochastic energy loss is taken into account, in order to model the fluctuations in muon range and in light production. The following processes are considered:

- delta electrons
- bremsstrahlung
- e^+e^--pair production
- hadronic interactions

Energy losses larger than 0.5 GeV are stored for further simulation of the light output. Interactions with smaller energy deposition are treated as continuous. Their light production is assumed to be purely Cherenkov like. The energy range is limited to muon energies smaller than $10^{5.5}$ GeV. For higher energies an alternative code by Lipari and Stanev [82] was used. Muons of all simulated energies can be propagated, but the light output of the stochastic processes with energies smaller then 1% of the muon energy are simulated in approximation only. Systematic studies of the influence of the used propagation code are underway [83].

5.1.3 Photon Propagation

The light propagation and photo electron production is simulated with the program `PTD` [84]. The photons are not treated individually. Instead the light intensity is stored in tables as a function of distance and orientation of the optical module to the emitter. As emitters, muon tracks and secondary showers are distinguished, because of their different emission characteristics: the light emission of a track with stochastic energy losses is composed during detector simulation of the light of a minimum ionizing muon, superimposed with the light of showers from the stochastic energy losses. The following processes are simulated:

- emission characteristics of track and showers
- optical ice properties as scattering and absorption
- transmissivity of the glass pressure sphere
- spectral and angular dependence of PMT quantum efficiency

The light density is stored in form of the mean number of photo electrons per square meter of cathode area. The delay of photons due to scattering in the ice is stored in a distribution of the photon arrival times, from which is sampled in the detector simulation. For showers the light intensity is approximated to scale linearly with the shower energy.

As described in section 4.6 the optical properties of the ice are depth dependent. The full implementation of the depth dependency requires an additional dimension in the tables and is underway. Meanwhile an approximation is used. The detector is split up in layers with constant optical properties. The layers are described by separate sets of tables. Each module is treated according to the layer it is located in, as if this layer would be infinitely thick. This approximation neglects the change of optical ice properties along the photon path. That is justified by the fact, that most detected photons originate from sources closer than the dimension of the layers.

5.1.4 Detector Simulation

The detector response is simulated with the program `amasim` [85, 86]. For each module the mean number of photo electrons from the track and from the showers, are read from the photon tables. The actual number of photo electrons is randomized according to Poisson statistics. The arrival time of each photon is derived by sampling the arrival time distribution given in the tables. For each photo electron a pulse is generated. The pulse height is sampled from a characteristic distribution. The pulse form is taken from a library of typical pulse shapes, that represent the different types of signal transmission: coax cable, twisted pair cable and optical fiber. Finally the wave form is assembled as the superposition of all pulses on the module. As in experimental data the threshold crossing time (leading edge of the pulse), the time over threshold and the pulse hight is stored. In analogy to experimental data, the trigger requires a minimum number of hits in a gliding time window (multiplicity trigger).

The individual propperties of the modules are represented by a number of parameters such as: location, individual sensitivity, noise rate, typical pulse height, signal transmission technology, threshold level. After-pulsing and time jitter were simulated the same way for all modules.

5.2 Event Reconstruction

The neutrino separation is organized in filter levels (cut levels). The lower filter levels are based on fast and approximate fits, which yield parameters, that allow to reject the clearly downgoing majority of the events. At higher filter levels more precise and time intensive reconstructions are applied. The primary goal is the correct reconstruction of the zenith angle, in order to reject the vast majority of events, caused by atmospheric muons.

Photon scattering in the ice delays a fraction of the photons. The photon arrival time distribution becomes asymmetric. Therefore a simple least square fit is not applicable. Instead likelihood reconstructions were developed.

5.2.1 First Guess Fits

The name for this class of fast fits developed from the need to initialize the track reconstruction with a “first guess” about the track parameters. These “guesses” are analytic expressions that characterize the hit pattern and can be calculated without (time consuming) iterations. They have proven effective for the low level filtering.

The Linefit

A first guess fit for a track is the so called linefit [87]. It is based on the assumption that the hit location is given by $\vec{r_i} = \vec{r_0} + \vec{v}(t_i - t_0)$, with the hit time t_i and hit (module) position at $\vec{r_i}$. Note that this approximation neglects the Cherenkov emission angle.

The minimization of $\chi^2 = \sum_i (\vec{r_i} - \vec{r_0} - \vec{v} \cdot t_i)^2$ gives the solution

$$\vec{v} = \frac{< \vec{r_i} t_i > - < \vec{r_i} >< t_i >}{< t_i^2 > - < t_i >^2} \qquad and \qquad \vec{r} =< \vec{r_i} > -\vec{v} < t_i > \quad . \tag{5.1}$$

where brackets stand for the mean value over all hits. The resulting values $\vec{r_0}$, t_0 can be taken as the coordinates and $\frac{\vec{v}}{v}$ as the direction of the muon.

Cut parameters: Most important selection parameter of the linefit is the **zenith angle**,

$$\cos\theta_{LF} = -\frac{v_z}{|\vec{v}|} \quad . \tag{5.2}$$

The resolution is about 10°. Another cut parameter is the absolute value v of the velocity, the so called **"velocity of the linefit"**. It characterizes the speed of the development of the light pattern in the direction of the track. For a minimum ionizing muon one expects a relatively narrow but elongated hit pattern, that develops with a speed close to the speed of light. Such a pattern provides a clear direction. If there is no clearly directed time development, the direction information is poor and the velocity parameter is small. However, a clearly directed time development is missing as well, if a muon creates a lot of light and scattered photons obscure the directionality. This is the case for high energy events. The effect of a cut on this parameter for high energy events will be discussed in section 6.4 (see figure 6.6).

Tensor of Inertia

A first guess fit for a cascade like event is the tensor of inertia. It is defined as

$$I^{k,l} = \sum_{i=1}^{N_{hits}} a_i \cdot (\delta^{kl} \cdot (\vec{r_i}^{\,2}) - r_i^k \cdot r_i^l) \tag{5.3}$$

where $\vec{r_i}$ is the distance of hit i to the center of gravity of all hits and a_i an amplitude weight.

Cut parameters: The ratio of the three eigenvalues I_1,I_2,I_3 characterizes the hit topology of the event. The smallest eigenvalue, I_1, corresponds to the longest axis of the event, its eigenvector points in the direction of the track. For spherical events, the three eigenvalues should be of approximately equal size. For track-like events, one expects a clear difference between I_1 and I_2,I_3. High energetic electrons or photons in ice create a cascade (shower) of just a few meters length. Scattering in the ice isotropizes the light, creating a nearly spherical hit pattern, without clear development direction. Such events are hard to reconstruct and yield a relatively high fake rate. With a cut on the **sphericity**, $3 \cdot I_1/(I_1 + I_2 + I_3)$, these events can be rejected.

5.2.2 Likelihood Reconstructions

There is a variety of likelihood reconstructions. All are based on the optimization of the likelihood function $\mathcal{L}(R \mid H)$ that describes the probability to observe a response R of the detector given a hypothesis H for the emission process. This may be either a muon-track or a cascade. Scattering introduces large tails in the arrival time distribution, making a simple χ^2-fit inappropriate.

Likelihood Track Reconstruction

The best reconstruction accuracy is obtained with the likelihood track reconstruction [88]. The track is assumed to be a single, straight muon track of infinite length. The track has five degrees of freedom and can be described by spatial coordinates (x, y, z) and direction (θ, ϕ). The track likelihood function $\mathcal{L}(R|H)$ describes the probability to observe a detector response $R = \{r_i\}$, where r_i stands for time and location of the ith hit, given the track hypothesis $H = (x, y, z, \theta, \phi)$. It is given by the product of the individual likelihoods $\hat{p}_i(r_i|H)$ to observe the hit r_i given H. The track is reconstructed by maximizing the (logarithm of the) event likelihood

$$log[\mathcal{L}(R \mid H)] = log\left(\prod_{i=1}^{N_{hits}} \hat{p}_i\right) = \sum_{i=1}^{N_{hits}} log(\hat{p}_i) \overset{!}{=} max\ . \tag{5.4}$$

The likelihood function represents the knowledge about the hit arrival time. The light emission is assumed to originate from a straight muon track emitted under the Cherenkov angle. It takes into account the influence of the optical ice properties and the PMT jitter. Noise is represented by a finite probability to register a hit independent of the track hypothesis. The light distribution is parameterized as an analytical expression [89].

The standard seed to the likelihood track fit (LH) is the line fit result. However, it has proven useful to start a number of LH fits with random seeds in order to avoid the convergence to local minima. The method is called **iterative likelihood fit** (LHi).

Another variation of the likelihood track fit is the introduction of a Bayesian bias. The *a priori* knowledge, that the overwhelming number of tracks are down going, is translated to: any given event is much more likely caused by a misreconstructed atmospheric muon than by a neutrino induced up going muon. Accordingly any down going track hypothesis is much more likely than any up going. A zenith angle dependent global weight is multiplied to the likelihood. The resulting fit is called **Bayesian fit**.

The standard likelihood defined above is based on the expectation of the hit arrival times only. The probability to observe a hit at a given distance at all, is not taken into account. This may lead to fit results with unlikely hit patterns: modules close to the hypothetical track, that do not register a hit, and hits observed far away from the track, are not taken as evidence against this hypothesis. This additional information is used by a reconstruction that combines the hit arrival time probability and the hit probability (LHphit). The highest reconstruction accuracy was reached with a likelihood that accounts for the in average earlier arrival time, if one out of multiple photons is considered. According to *multiple photo electrons* it is called **mpe-fit** (LHmpe).

Cut Parameters for Likelihood Track Reconstructions

All the likelihood track reconstructions yield the same parameters. The possible cuts and cut concepts are therefore the same.

Zenith angle θ The most important cut parameter is the zenith angle since it separates downgoing tracks from up-going neutrino induced tracks. All other cut parameters serve for the rejection of tracks that are badly reconstructed.

The likelihood parameter: The absolute value of the likelihood at the extremum can be used as goodness of fit parameter. In analogy to a reduced χ^2 the likelihood parameter L is defined as the logarithm of the likelihood divided by the number of degrees of freedom

$$L \equiv -log(\mathcal{L}(x, y, z, \theta, \phi))N_{hits} - 5 \tag{5.5}$$

If the hit pattern observed can be produced by the hit pattern expected from the track hypothesis a good likelihood is reached. Note that a small absolute value of the likelihood parameter represents well reconstructed tracks.

Direct observables: The number of hits with a small time residual is a measure for the reliability of the track fit. The time residual is defined as

$$t_{res} = t_{hit} - t_{geo} \tag{5.6}$$

where t_{geo} is the arrival time expected for an unscattered photon emitted under the Cherenkov-angle from the reconstructed track. Hits are defined to be *direct* with respect to the track and a time window. Accordingly the **number of direct hits**, $N_{dir,LH}^{-15..20ns}$, is defined as the number of hits with -15 ns $\leq t_{res} \leq +20$ ns, where t_{res} is the time residual for the hit, with respect to the result of the likelihood track reconstruction (LH). In analogy the **direct length**, $L_{dir,LH}^{-15..20ns}$, is defined as the length of the reconstructed track between the two most distant direct hits, projected onto the track.

If the reconstructed track is close to the true track, direct hits represent unscattered photons. They carry most information about the track. A large number of direct hits is an indication of an emitter according to expectation. A large direct length indicates elongated, i.e. track-like, emission. Further, tracks with large direct length are reconstructed with good angular precision.

The smoothness parameter S The smoothness of an event characterizes the homogeneity of the hit distribution along the reconstructed track. In analogy to a Kolmogorov-Smirnov-test, the smoothness measures the distance between a constant hit density along the track($S = 0$) and the observed accumulation of hits along the track. The strongest discontinuity is the concentration of all hits (except one that marks the end) at the beginning of the track ($S = -1$), or all except one hits at the end of the track ($S = 1$). A variety of so called “flavors” of smoothness have been developed and described in [90]. The flavors used later on shall be introduced shortly:

$\mathbf{S_{van}}$ The “vanilla”-flavor is the simplest version of smoothness based only on the hit distribution along the track.

$\mathbf{S_{phit}}$ For this flavor weights were applied to the hits according to their probability to be caused by the muon track (for definition see next paragraph). This includes modules that do not measure a hit but were expected to measure one. The inclusion of this information complements especially the likelihood that is based on the time probabilities only.

$\mathbf{S_{phdir}}$ This flavor is similar to the previous one but is based only on direct hits, as defined above.

$\mathbf{S_{rl}}$ This flavor includes all hits that can be associated, i.e. fulfill the very weak time residual requirement -1000 ns $< t_{res} <$ 2000 ns.

A number of smoothness parameters were derived from the flavors introduced. For example the geometric average of pairs of flavor: $S_{phvan} = \sqrt{S_{van}^2 + S_{phhit}^2}$ for *vanilla* and *phit*, S_{phph} for *phit* and *phdir* and S_{vnrl} for *vanilla* and *rl.*

Likelihood Energy Reconstruction

The energy reconstruction is based on the hit probability as a function of the track energy. With increasing energy the light output due to secondary processes increases. More light gives rise to an increased probability to register a hit at a given distance or respectively increase the radius where a given hit probability is reached. The energy reconstruction can be understood as the fit of this radius. Typically one talks of the illumination radius where the hit probability reaches 50%, or the 1 photo electron radius where 90% of the modules are hit.

Technically speaking orientation and position of the track are fixed, f.e. according to the result of a previous track fit. Then the total (energy dependent) likelihood of the hit modules to be hit and the non hit modules to be not hit is maximized. The total hit likelihood is given by

$$log[\mathcal{L}(R|H, E_\mu)] = \sum_{hit\ OMs} log(P_\epsilon^{hit}) \ + \sum_{not\ hit\ OMs} log(P_\epsilon^{no\ hit}) \ \overset{!}{=} \ max\ . \tag{5.7}$$

The hit probability for a given light density ρ_{ph} can be written as a function of the probability for *one* photo electron P_1^{hit}

$$\begin{aligned} P_\epsilon^{no\ hit} &= (1 - P_1^{hit})^\epsilon && (5.8) \\ P_\epsilon^{hit} &= 1 - (1 - P_1^{hit})^\epsilon \quad , && (5.9) \end{aligned}$$

where ϵ is proportional to the light density and accounts for the PMT sensitivity $\epsilon \propto \rho_{ph}$.

The hit probability is parameterized as a function of the OM's distance and orientation with respect to the track. The individual OM sensitivity is corrected for. The light output is approximated as continuous along an infinite track. The continuity is justified by the scattering in the ice that smears out the shower profile after tens of meters already. The infinite track is justified by the fact that the range of the high energy muons is on average much longer than the detector dimension.

A natural extension of the use of the *hit probability* is the use of the probability to measure a given *amplitude*. As a part of this work a reconstruction based on the observed amplitudes was implemented but abandoned later on. For a detailed discussion see section 6.2.

Cut parameters: The **reconstructed energy**, E_{phit}, can be used as energy selection parameter for the separation of high energy events. In analogy to the track reconstruction the **likelihood parameter** is defined as

$$L_{phit} \equiv -\frac{log(\mathcal{L}(x,y,z,\theta,\phi,E_\mu))}{N_{OM,operating}-1} \quad . \tag{5.10}$$

Further the geometric average of the hit probability of all hit modules, P_{hit}, and the probability for all non hit modules to be not hit, P_{nohit} are defined as

$$P_{hit} = \left(\prod_{i=1}^{N_{OM,hit}} P_i^{hit}\right)^{1/N_{OM,hit}} \qquad P_{nohit} = \left(\prod_{i=1}^{N_{OM,nohit}} P_i^{nohit}\right)^{1/N_{OM,nohit}} \tag{5.11}$$

These parameters test whether all hits/non hits are according to expectation making up a topological test parameter. The correlation of the hit probability with the energy proved powerful as well. If the energy is larger, the ratio of modules with hit probabilities close to unity, to modules with low hit probabilities gets large, i.e. the volume to surface ratio of the illumination cylinder. This results in a larger average hit probability.

Likelihood Cascade Fit

One of the major backgrounds after low level filtering are nearly spherical events. Most likely they are caused by single high energetic cascades [1] from down going muons. They have bad directional information and are therefore reconstructed upward in fraction. It has proven useful to fit this background hypothesis explicitely and compare its likelihood to the one for the track hypothesis. The likelihood function for the shower fit was taken over from the search for electron-neutrino induced cascades [91]. The expected light pattern is well approximated by a spherically symmetric emission, because scattering in the ice isotropizes the light after tens of meters.

Cut parameters: The likelihood parameter for the cascade fit is defined as $L_{casc} \equiv -\frac{log(\mathcal{L}_{casc})}{N_{hits}-4}$. Rather than the absolute value of the likelihood parameter, the **ratio of the likelihood parameters of cascade and track reconstruction** is used as cut parameter: L_{casc}/L_{track}, where L_{track} is defined in equation 5.5.

---

[1] Cascades and shower are used synonymic in this work.

5.3 Cut Selection and Optimization

The final cut level for the atmospheric neutrino analysis and the high energy analysis was developed with the cut optimization tool `cuteval` [92, 93]. It is based on a downhill simplex minimization with simulated annealing. An optimization function, that depends on the number of signal and background events after cuts, is maximized with respect to the applied cuts. Common optimization functions are the ratio of signal to background (SIG/BG) or signal to square root background ($SIG/\sqrt{BG}$). The optimization yields the position of the optimum in the cut parameter space and the value of the optimization function at the optimum. The value allows to compare different sets of cuts. The necessary number of minimization steps and the instability (oscillation) increases strongly with the number of dimensions, i.e. cut parameters. Up to six cuts have been optimized simultaneously.

First a set of cut parameters was selected. After that the cuts were extrapolated for a systematic analysis of the passing rates as function of cut position, i.e. event quality. Different classes of events require different sets of cuts. Accordingly, different optimization functions were used. They are referred to as *modes* as well.

Cut Selection

The ideal cut parameter set is a minimal complete set of independent parameters. A cut set is supposed to be *minimal* in the sense of including no redundant cuts, *independent*, in order to simplify systematics and *complete*, in order to extract as much signal as possible. For the selection of the best possible cut set the following strategy was chosen:

In order to extract as much information as possible, a large variety of cuts was analyzed. The cuts were evaluated concerning their selection power with respect to a chosen optimization function. In a first approach pairs of cuts were optimized. The pair of cuts that yielded the best value of the optimization function, e.g. signal to background ratio, was combined with each of the remaining cuts. The triples of cuts were optimized again, and the best one combined with each of the remaining cuts. Iteratively cut parameters are added as long as they yield a gain in e.g. the signal to noise ratio. The procedure is stopped if no cut is left that improves the optimization result. That means, the cut parameter set is complete with respect to the list of cuts investigated.

Cut Extrapolation

The main motivation for cut extrapolation was the limited amount and precision of the background MC. However, the obtained cut parameterization proved to be also useful for the systematic analysis. Based on the development of the cut positions in that part of the cut space, where the background is well described by MC, the cut positions are parameterized. They may be extrapolated to the region in cut space, where the background MC is cut away or has low statistics. The cut parameterization was developed with the cut optimization tool `cuteval`.

For a given set of cut parameters the optimization finds the best set of cut positions, with respect to the optimization function. The set of cut positions corresponds to one point in the cut space. The cut parameterization was obtained from the change of this point with a varying background rejection level. Therefore the cuts were optimized at a series of background rejection levels. This was done by constraining the optimization, to keep a minimum of background MC events. If the cut set is optimized n times with the constraint to leave $N_{bg,n}$ events of background MC in, one obtains a set of cut positions c_n for each cut parameter C. From the correlation to the number of background events N_{bg} and cut position a parameterization $c = c(N_{bg})$ can be derived. For independent cuts and exponentially falling background the cut position is expected to scale with the logarithm of the number of background events. With the fit the number of background becomes a parameter, that defines the cut position. The combination of all cuts as a function of background parameter N_{bg} can then be combined to one quality requirement Q that depends only on the background parameter N_{bg}:

$$\begin{aligned} Q(N_{bg}) &= C_1 > c_1(N_{bg}) \\ &\& \ C_2 > c_2(N_{bg}) \\ &\& \ C_3 > c_3(N_{bg}) \\ &\& \ \ldots \end{aligned} \tag{5.12}$$

where C_i denotes the i-th cut and $c_i(N_{bg})$ the cut position. With the event quality Q all requirements for an event are defined in one parameter and can be expressed any rejection level, independent of the actual number of events left in the background MC.

5.4 The Method of Average Upper Limits

Construction of Upper Limits

The commonly accepted method for the derivation of an upper limit is the Neyman construction of confidence intervals [94].

Given a small mean number of expected background events $\langle n_b \rangle$ and a small mean number of signal events $\langle n_s \rangle$, the probability to observe n events is given by a Poisson probability for signal in the presence of background:

$$P(n \mid \langle n_b \rangle + \langle n_s \rangle) = \frac{(\langle n_b \rangle + \langle n_s \rangle)^n}{n!} e^{-(\langle n_b \rangle + \langle n_s \rangle)} \quad . \tag{5.13}$$

The measurement of a number of events n_{obs} for a known number of expected background events $\mu_b = \langle n_b \rangle$, fixes a mean number of signal events $\mu_s = \mu_{s,\alpha}(n_{obs}, \mu_b)$, such that the probability to observe n_{obs} events or less, equals the *error probability* α

$$\sum_{n=0}^{n_{obs}} P(n \mid \mu_b + \mu_s) = \alpha \quad . \tag{5.14}$$

For any mean number of signal events higher than μ_s, a measurement of n_{obs} or less events, has a smaller probability than α. Thus the probability to make an error by rejecting the hypothesis of a higher signal than μ_s is smaller than α. The quantity $1 - \alpha$ is called *confidence level.* The maximal mean number of signal events that is not excluded is called the *event upper limit* and is given by $\mu_{s,\alpha}$. The *flux upper limit* is obtained by rescaling the simulated flux Φ_{MC} by the ratio of events predicted from MC, n_s, and the event upper limit, $\mu_{s,\alpha}(n_{obs}, \mu_b)$:

$$\Phi_{1-\alpha} = \Phi_{MC} \ \cdot \ \frac{\mu_{s,\alpha}(n_{obs}, \mu_b)}{n_s} \tag{5.15}$$

Cut Motivation using Average Upper Limits

If data are used to place cuts at the same time as they are used in order to make a measurement there is a danger of biasing the result by selecting fluctuations of the data. This is especially the case for limit calculations where few or no events are used for a statement. Guidelines as cutting on the last event or signal to background ratio may lead to incomplete exploitation of the information available. Even worse, they may lead to too stringent limits.

In order to solve this problem Feldman and Cousins [95] have proposed an alternative construction principle for confidence belts based on the probability ratio

$$R = P(x \mid \mu)/P(x \mid \mu_{best}), \tag{5.16}$$

where $P(x \mid \mu)$ is the probability to observe x in case of a true mean μ and $P(x \mid \mu_{best})$ is the probability to observe x in case of the best-fit physically allowed mean. The numerical values they derive for event upper limits $\mu_{s,\alpha}$ as they give in [95] were chosen for the derivation of upper limits in this work.

Another problem of upper limits is, that a lower observation than the average background expectation leads to a more stringent upper limit than expected from an observation according to the background expectation. In order to quantify the fluctuation of the observation from the expectation they define a parameter called *experimental sensitivity* that allows to quantify the goodness of the fit for the background. This sensitivity or *average upper limit* $\bar{\mu}(n_b)$ is given by the average over all possible limit outcomes $\mu(x_0)$ weighted by their Poissonian probability $P(x_0 \mid \langle n_b \rangle)$ to occur in the absence of a true signal:

$$\bar{\mu}(n_b) = \sum_{x_0=0}^{\infty} \mu(x_0) \frac{\langle n_b \rangle^{x_0}}{x_0!} \ e^{-\langle n_b \rangle}. \tag{5.17}$$

The difference between the average upper limit and the obtained upper limit characterizes the probability of the observation.

As can be seen from the definition the average upper limit is based on the MC prediction for background only. It can therefore be used to motivate cuts, especially the final cut, in a data-independent way. In the limit of many experiments it results in the best exploitation of the information in the data. For the derivation of a limit in this work the position of the final cut was defined in advance to be placed according to maximal sensitivity, i.e. at the point of the lowest average upper limit (for details see [96]).

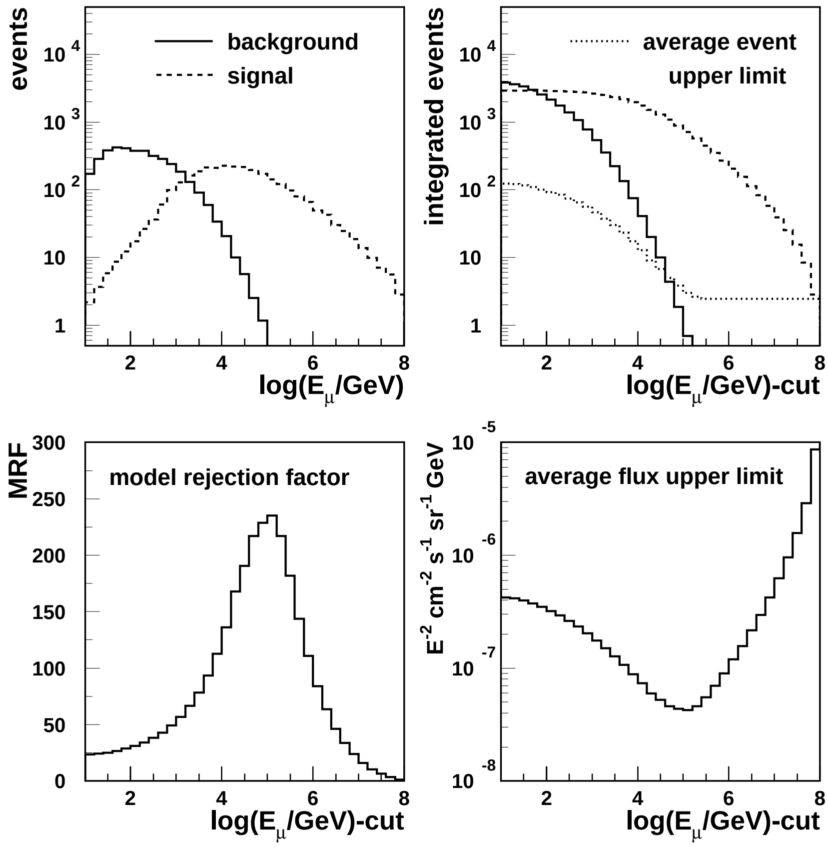

Figure 5.1: Motivation of the final cut according to maximal sensitivity. Top left: Signal and background distribution. Top right: Integrated signal and background distribution together with the average event upper limit. This is the smallest mean number of signal events, that is excluded, when precisely as many events are observed as expected from background. The ratio of the signal to this event upper limit is the model rejection factor (MRF, bottom left). Bottom right: The average flux upper limit as a function of the final cut position.

Figure 5.1 illustrates the steps from a given signal and background distribution to the construction of an average upper limit. As a best case estimate the true muon energy distribution at trigger level was used. Atmospheric neutrinos were assumed as the only background and high energy neutrinos from a E^{-2} spectrum with a flux of $E^2 d\Phi/dE = 10^{-5}\mathrm{cm}^{-2}\mathrm{s}^{-1}\mathrm{sr}^{-1}\mathrm{GeV}$ were taken as signal. The upper left plot shows the two energy spectra. The upper right shows the same distribution integrated up from the right. This way the height at a given energy corresponds to the number of events passing a cut at that energy. Together with the integrated distributions the so called *average event upper limit* is plotted, i.e. the average upper limit as defined in 5.17 in terms of the number of signal events. It represents the maximum mean number of signal events that is consistent with a measurement of precisely as many events as expected from background. Note that this parameter is independent of the signal assumption. For the background free case this is 2.44. The lower left plot shows the *model rejection factor*: this is the ratio of the number of predicted signal events to the average event upper limit. The initial flux assumed has to be reduced by that factor if no signal was observed. The result of this operation is shown in the lower right plot: the *average flux upper limit* [2]. The position of the final cut according to the highest sensitivity corresponds to the position where the lowest flux upper limit is reached.

The average upper limit reached in this toy-analysis can be seen as a very idealized sensitivity: this choice represents the assumption of a perfect energy reconstruction and a perfect neutrino event separation. Any realistic separation will yield a higher upper limit.

This concept was mainly chosen to fix the problem of the setting of the last cut. However, it is applicable for any number of cuts. The optimization of the sensitivity in several dimensions with the cut optimization procedure discussed in section 5.3 is a very powerful combination.

---

[2] Sensitivity and average flux upper limit are used synonymic in this work, but with the notation, that a high sensitivity corresponds to a low average upper limit.

Chapter 6

Flux Limit based on the Atmospheric Neutrino Selection

The topic of this work is the search for high energy neutrinos with focus on the investigation on a possible diffuse high energy component that may originate from extraterrestrial sources. According to the Fermi acceleration mechanism [5] and gamma ray background observations [41] a generic E^{-2}-spectrum with an example flux of $dN/dE = 10^{-5}\ E^{-2}\ \ \mathrm{cm}^{-2}\mathrm{s}^{-1}\mathrm{sr}^{-1}\mathrm{GeV}$ will be assumed in the following.

The first step towards the observation of high energy neutrinos was the separation of atmospheric neutrinos in order to proof the detection capabilities af the detector. This was done in a group effort together with A. Biron and C. Wiebusch [97, 98]. Afterwards a variety of further advanced atmospheric neutrino searches was conducted [93, 99, 100, 101]. Therefore, in the following, the result of a more recent analysis [101] will be used.

The second step was to find a good energy sensitive parameter for the separation of high energetic events where an excess of neutrinos from an E^{-2}-spectrum over atmospheric neutrinos would be expected. For this purpose, an energy reconstruction method developed for the Baikal experiment [45] was modified for the application to AMANDA data and compared to an existing energy reconstruction. The sensitivity reach with the achievable resolution was compared to the reach with basic topological cut parameters.

The analysis of the atmospheric neutrino sample with respect to an additional high energy component, led to the development of a separate high energy neutrino separation, which is presented in chapter 7. The most important intermediate results from the analysis of the atmosopheric neutrino sample are presented in this chapter, in order to document the development and as input to future data analysis in AMANDA. The reader interested in the final high energy analysis only may skip the current chapter. The main results are summarized in section 6.5.

6.1 Neutrino Separation

The neutrino separation is organized in filter levels (cut levels). The lower filter levels are based on fast and approximate fits that yield parameters which allow to reject the clearly downgoing majority of the events. The remaining samples are small enough to apply more time consuming reconstructions that use as much information as possible. There have been a number of iterations including two MC mass productions in order to derive the final cuts.

Already at the second cut level it turned out that an unsimulated background class outnumbered the simulated background. This background appeared to cluster in depth of the center of gravity of the hits. Three clear peaks were observed at top, middle and bottom of the array. The background is therefore named the cog_z background. For the atmospheric neutrino analysis a number of rejection methods were developed. These methods will be used in the high energy neutrino selection again.

The cuts of level three and above, especially the cuts against the unsimulated cog_z-background were derived with the cut evaluation tool `cuteval` as described in section 5.3.

Preprocessing: The preprocessing consists of all steps to prepare the data for reconstruction, i.e. run selection, calibration and hit cleaning. The run selection is based on the number of stable modules in the run: Only runs with more than 220 stable OMs were used (for details see section 4.7). The calibration includes time (leading edge, LE), amplitude (ADC) and time over threshold (TOT) calibration. The leading edge is corrected for the amplitude dependence of the rise time. The amplitude is converted to the number of photo electrons correcting for individual 1 p.e. levels of the PMTs. Hit cleaning is the removal of all hits that are obviously not good for track reconstruction. This may be hits that are independent of the track such as dark noise or hits due to technical artefacts as cross talk or afterpulsing. Dark noise and afterpulses are removed by a cut on the arrival time relative to the trigger time. Uncorrelated noise and some of the cross talk is reduced with an isolation criterion. Cross talk typically produces short pulses. Unphysical pulses from the electronics may be extremely long or high. The following cuts are applied:

- time window: $0 \leq \mathrm{LE} \leq 4500$ ns with a trigger peak at about 2000 ns
- raw ADC > 50 mV
- calibrated ADC between 0.1 and 1000 p.e.
- isolation: hits are required to have a neighboring hit within 100 m in a time window of 500 ns.
- width: $125 \leq \mathrm{TOT} \leq 2000$ ns

In addition hits from dead or unreliable OMs and hits from OMs with missing or bad calibration information are removed.

Level 1 (filtering): The filter level 1 is based on the fast and approximate linefit. Cuts are placed on the zenith angle and the velocity given by the linefit. A Gaussian fit to the zenith angle mismatch yields a width of $\sigma_{\Delta\theta LF} \approx 9^\circ$. The zenith cut is placed 20° above horizon, the cut on the velocity given by the linefit at 0.1 m/ns:

$$\begin{aligned} \theta_{LF} &> 70^\circ \\ v_{LF} &> 0.1 \text{ m/ns} \quad . \end{aligned} \qquad (6.1)$$

The total number of events in experimental data is $1.18 \cdot 10^9$. Atmospheric muon MC predicts $0.903 \cdot 10^9$ events and atmospheric neutrino MC 8980 events. The level-1 cuts reduce the data to 5.3%, the downgoing muon background MC to 3.6%. The atmospheric neutrino signal passes with 34%. The difference between data and downgoing muon background MC is due to the cut on the velocity given by the linefit v_{LF}. This cut turned out to remove a large fraction of high energetic events too. Details will be discussed in the motivation for the high energy selection in the next section.

Level 2: Filter level 2 is based on the likelihood track fit (LH) and the six fold iterative likelihood track fit (LHi6). Cuts are placed on the zenith angle, the likelihood parameter, the number of direct hits and the total number of hits after cleaning. The zenith angle mismatch of the likelihood track fit is $\sigma_{\Delta\theta_{LH}} \approx 3.8^\circ$. The zenith cuts are again placed about 2 σ above horizon.

$$\begin{aligned} N_{ch}^{clean} &> 11 \\ \theta_{LH} &> 70^\circ \\ \theta_{LHi6} &> 80^\circ \\ L_{LHi6} &< 9.5 \\ N_{dir}^{-20..+25ns} &> 3 \quad . \end{aligned} \qquad (6.2)$$

The cuts [1] reduce the data to $4.5 \cdot 10^{-4}$, atmospheric muon MC to $4.3 \cdot 10^{-4}$ and atmospheric neutrino expectation to 15%.

Level 3: Filter level 3 is based on a likelihood track fit with 16 iterations (LHi16), a likelihood fit of the energy (E_{phit}) that uses hit probabilities, the tensor of inertia (ToI) and a likelihood cascade fit (Casc). Two sets of cuts with different focus were applied. The first set is based on a reinforced zenith angle cut and cuts on the likelihood parameter for the iterative track fit, the likelihood parameter of the energy fit and the ratio of the likelihood parameters for the cascade fit compared to the one of the track fit. Zenith and track likelihood cut are just reinforced and straight forward. In contrast to the track fit likelihood, that is a measure for the agreement between observed and expected time structure of the event, the likelihood parameter of the

---

[1] Due to a processing bug some reconstructions had to be redone and cuts were applied twice. The details are avoided here because the principle of the neutrino selection is not affected.

energy fit measures the probability to observe hits at all as a function of energy of the track, distance and orientation of the optical module. The cut on the ratio of cascade and track fit is motivated by the fact that at this reduction level a major fraction of fakes is caused by spherical events. They originate most likely from energetic secondary processes of downgoing muons. The topology is compatible with the one for ν_e-cascades. If events are fitted better by a cascade fit than by a track fit they are most likely background and removed:

$$\begin{aligned} \theta_{LHi16} &> 90^\circ \\ L_{track} &< 8.7 \\ L_{phit} &< 6.0 \\ L_{casc}/L_{track} &> 0.95 \end{aligned} \tag{6.3}$$

The second set of cuts was developed for the reduction of the unsimulated cog_z-background. The reduction of this background will be further developed in cut level 4. The following are just a loose set of preparing cuts:

$$\begin{aligned} -100\text{ m} &< cog_z < +170\text{ m} \\ 3 \cdot I_1/(I_1+I_2+I_3) &< f_{inert}(\theta_{LHi16}) \\ L_{dir,LHi16}^{-15..+75ns} &< f_{L_{dir}}(\theta_{LHi16}) \end{aligned} \tag{6.4}$$

where

$$\begin{aligned} f_{inert}(\theta_{LHi16}) &= MIN\left(140\text{m}\ ,\ \frac{w + 2 \cdot L_v \cdot |\cos\theta_{LHi16}|}{\sin\theta_{LHi16}}\right) \\ f_{L_{dir}}(\theta_{LHi16}) &= MIN(\ 0.8\ ,\ 2.0 - 1.6 \cdot |cos\theta_{LHi16}|\ ) \end{aligned}$$

with $w = 60$ m and $L_v = 10$ m.

The first of the three cuts reduces so called corner clippers, events with the muon crossing the detector in the very top or bottom or even missing the detector volume. The incomplete light cone is hard to reconstruct yielding only poor quality tracks. The second cut is an angle dependent cut in the sphericity as introduced in the last section. The third criterion cuts on the direct length but again with an angular dependence in order to account for the detector geometry: horizontal tracks pass much less instrumented volume than vertical events.

All level-3 cuts reduce the data sample to $1.3 \cdot 10^{-4}$, atmospheric muon MC to $0.8 \cdot 10^{-4}$ and atmospheric neutrino expectation to 6.9%.

Level 4: The final i.e. neutrino separation cut level is based mainly on a likelihood track reconstruction that takes the modified arrival time for multiple photons per optical module and the hit probability into account. Further reconstructions were applied that were not used in the final cut set: A likelihood track reconstruction with a Bayesian weight, energy reconstructions

that are based on the latest track reconstructions and a dipole fit.
The final cut set was developed with the help of the cut optimization tool `cuteval` introduced in chapter 5. First a minimal complete set of independent cut parameters was selected. In a second step cuts were extrapolated for a systematic analysis of the passing rates as function of cut power i.e. event quality. The details of the procedure can be found in [92, 101]. The following set of cuts was determined:

$|S^{van}| < 0.28$: The smoothness of the hit pattern. The subscript “van” for vanilla indicates that no additional weights are applied. This parameter measures the homogeneity of the hit distribution along the track. It assumes -1 for all hits at the beginning of the track, 0 for completely equidistant hits and 1 for all hits at the end of the track. A small smoothness parameter indicates a continuous light emission along the track. Discontinuous light patterns are caused by downgoing tracks with noise faking a upward going time flow.

$|S^{phit}|/(\theta - 90^{\circ}) < 0.01$: This variation of the smoothness takes the hit probability (as function of the distance and orientation from the hypothetical track) into account. The zenith dependence accounts for the larger background close to the horizon which requires a more stringent cut.

$(N_{dir}^{(-15..75ns)} - 2) \cdot L_{dir}^{(-15..75ns)} > 750$ m: The number of direct hits times the direct length. The product results in either a long lever arm or many good hits which are both quality parameters.

$\log(\mathcal{L}_{up}/\mathcal{L}_{down}) > 7.7$: The best likelihood reached for a fit with upward going result compared to the best likelihood reached among downward going results. Similar to the Bayesian track fit this cut takes into account that the hypothesis of a downward going track is *a priori* more likely than the hypothesis of an upward going track.

$\Psi(LHmpe, LF) < 35^{\circ}$: The spatial difference between the direction of the best likelihood fit and the linefit approximation is a sign of clear time flow if both directions are about the same. This cut is especially efficient for cross talk events. While single cross talk hits may confuse the likelihood track fit the linefit reflects the overall time flow.

$\sqrt{{S_{dir(-15..75ns)}^{van}}^2 + {S_{dir(-15..75ns)}^{phit}}^2} < 0.55$: This combination of the two flavors of the smoothness is a varied *or*-combination. From visual inspection it was found that events from uncorrelated coincident muons were efficiently rejected with this cut.

Result: With this set of cuts 223 neutrino candidates were separated. The background MC predicts (7.5±4.8) events. Including neutrino oscillation (10% effect for $\Delta m^2 = 0.003$ and $\sin 2\theta^2 = 1.0$) the standard atmospheric neutrino MC predicts (335±3.4) events. This are just about 4% of the triggered events. The low recovery efficiency is partly due to the low trigger requirements. Another reason is that AMANDA-B10 is a just prototype detector. With its few strings it is much taller than wide and therefore only sensitive to nearly vertical tracks.

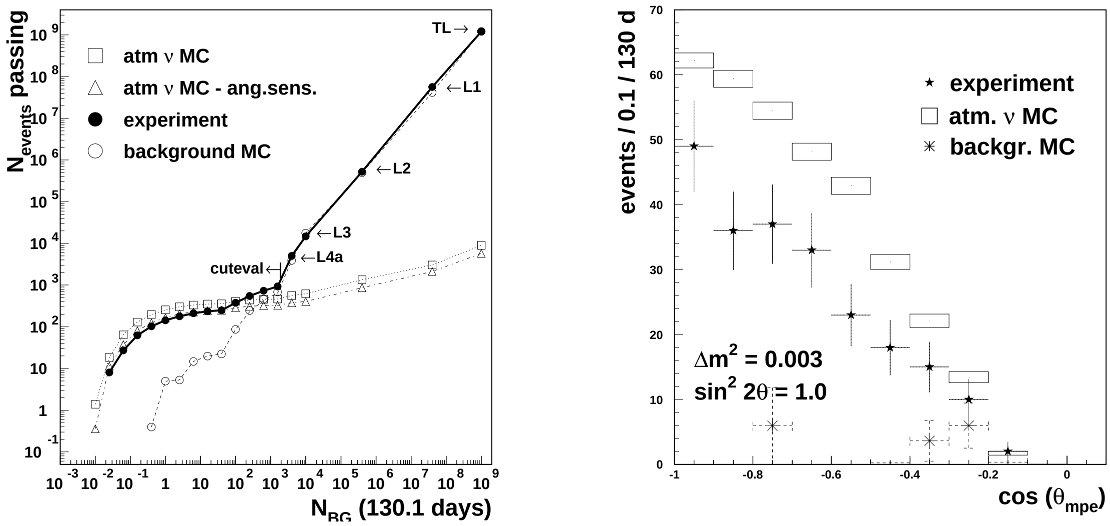

Figure 6.1: The atmospheric neutrino selection: Left: The development of the number of events in each sample as function of the background parameter. Right: The cosine distribution of the zenith angle ($\cos\theta_{LH,mpe}$). The signal MC prediction takes neutrino oscillation into account. Both plots show the over-prediction of atmospheric neutrinos in the standard signal MC (both figures taken from [101]).

Systematics: The most difficult part of the search for neutrinos is the proof of a detection of neutrinos in a natural environment detector that can not be tested in the lab and that has no test beam. At low cut levels the rejection of background is described by background MC. At higher cut levels the precision of the MC is not sufficient to describe all backgrounds. Here the comparison of the data with signal MC is more powerful because it is much less reduced by cuts compared to the background MC. Further the visual inspection of the events has proven powerful to identify background classes that are not described by the MC.

One of the strongest argument that the selected events are neutrinos is the development of the passing rates of data and MC with increasing cut strength. As shown in figure 6.1 at low cut levels the data clearly follow the background MC. From cut level four on data start to show a larger resistance against cuts and follow the prediction from signal MC. Even though the cut resistivity is a strong indication that another class of events starts dominating in the data the total number of events in data and atmospheric neutrino MC differ. Above cut level four the ratio of MC and data remains constant at about 2/3 of the signal prediction from the standard MC. Some part of the discrepancies disappears with a recently developed MC with a modified angular sensitivity of the OM (labeled *ang. sens.*). At the time of the following considerations on energy cut parameters and limit calculation (section 6.2 and 6.3) it was not yet available.

As one example of the fundamental observables the zenith angle distribution is shown in figure 6.1. Regardless of the different rate, the shape of the zenith angle distribution is well

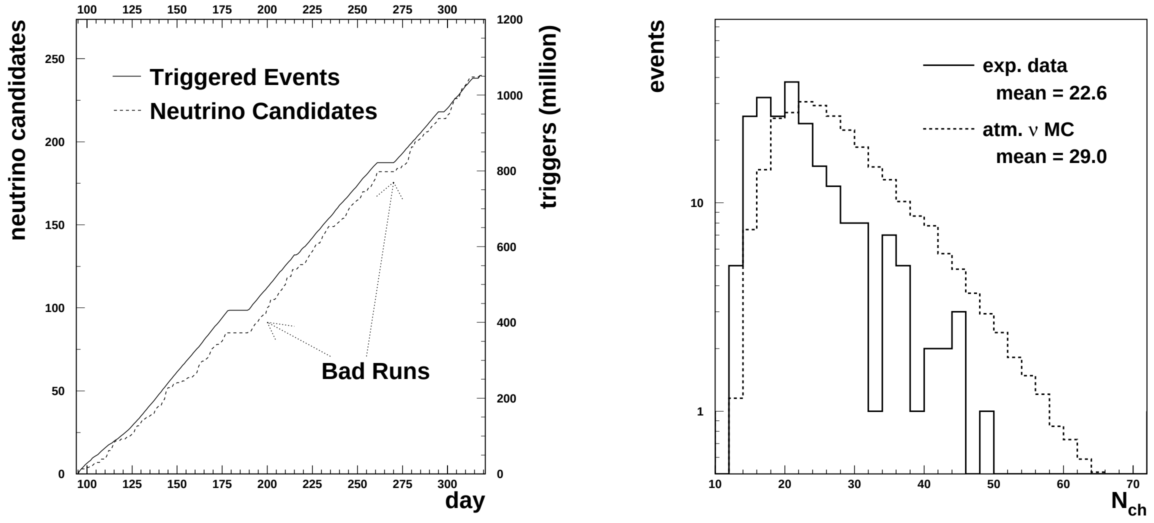

Figure 6.2: Left: Luminosity of the atmospheric neutrino selection. The upper line (solid) indicates the cumulative number of triggers the lower the cumulative number of neutrino events (dashed). The cumulated neutrino events follow the number of events triggered closely. Clearly visible are two periods with bad run quality. (numbers taken from [101]). Right: The number of hit channels N_{ch} at cut level 4. The mean for the MC distribution is shifted upward by 6.4 channels.

reproduced. Another fundamental systematic test is the detection time over the year. The number of neutrino candidates and the number of triggers over the year is shown in figure 6.2. The neutrino events accumulate over the year proportional to the total number of events.

The good agreement found between experimental data and signal MC for most observables is a clear indication that the selected events are neutrinos. However, the multiplicity distribution for the standard MC shows a significant shift in the mean and a harder spectrum than the experimental data (see figure 6.2 right plot). This discrepancy has implications for the derivation of a limit and will be discussed in more detail after the energy sensitive parameters.

Background estimate: Besides the proof, that the selected events behave as expected from signal, it is important to show how much background events may be left in the sample. Several independent estimates were done: background MC, visual inspection, fit of the background-typical distribution of cog_z and a background extrapolation method. For this method all cuts but one were applied and the cut parameter left was plotted. The extrapolation from the rejection region of this cut to the acceptance region gives an estimate how much background may be left in the final sample. The average result of the methods yields a background contamination of less than 20% [101]. However, the total flux normalization and the muon propagation are uncertain to 30% each.

Filter level	experiment	atm. μ BG MC	atm. ν MC
Trigger	$1.18 \cdot 10^9$	$9.03 \cdot 10^8$	8978.8
ϵ Level 1	$0.5 \cdot 10^{-1}$	$0.4 \cdot 10^{-1}$	0.34
ϵ Level 2	$0.4 \cdot 10^{-3}$	$0.4 \cdot 10^{-3}$	0.15
ϵ Level 3	$0.1 \cdot 10^{-4}$	$0.7 \cdot 10^{-5}$	0.07
ϵ Level 4	$0.2 \cdot 10^{-6}$	$0.5 \cdot 10^{-8}$	0.04
# events final level	223	7.5 ± 4.8	335.3 ± 3.4

Table 6.1: The atmospheric neutrino selection: number of triggers, cut efficiencies ϵ and final number of events in experimental data, atmospheric muon background MC and atmospheric neutrino MC for 130 days of life time. The details of the filter levels are discussed in the text (numbers taken from [101]).

6.2 Energy Selection Parameter

After the neutrino selection, an energy parameter is needed to test if there is an excess at higher energies. In case of consistency of data with the atmospheric neutrino expectation a limit will be placed. The problems of a data-motivated last cut have been discussed in section 5.4 and an alternative method was proposed. The method is purely Monte Carlo based. It scans through all possible cut positions and calculates the average upper limit at every cut position under the assumption that exactly as many events are observed as expected from background only. The minimal average upper limit corresponds to maximal sensitivity to a possible signal. The final cut will be placed at the position of the lowest average upper limit.

Energy reconstruction: There is one energy reconstruction available that is based on the hit probability as a function of the distance from a given track (E_{Phit}). An energy reconstruction that uses amplitude information was developed for the BAIKAL-detector by Streicher [45]. One major part of the work for this thesis was the extension of this method for the needs of AMANDA (E_{Pamp}). For MC events a resolution of $\sigma_{gauss}(log10(E_{Pamp}/E_{\mu,true})) \approx 0.4$ was reached. However, the simulation of the amplitudes did not describe the experimental data. After an analysis of the error contributions it turned out that for AMANDA-B10 the fluctuation of the light output already generates 0.3 in the logarithm of the energy error. That means that for B10 the theoretical precision of a method based on light intensity is limited to $\sigma(log10(E_{Pamp}/E_{\mu,true})) \geq 0.3$. As a consequence of the limited improvement potential, the further development of the amplitude-based energy reconstruction method was abandoned.

Instead, the existing energy sensitive parameters were investigated. The average upper limit was used to quantify the selection power of the cut parameters. A variety of parameters that are correlated with the true neutrino energy were tested: the reconstructed energy based on the hit probability (E_{phit}), the number of hit channels (N_{ch}), the number of hit channels per track length, the number of direct hits per direct length and more (for definition see section 5.2.2). The main result of this comparison is shown in figure 6.3. For the neutrino separation level given in [93], the average upper limit for N_{ch} is compared to the one for the reconstructed energy, the true muon energy and the true neutrino energy. Further, the true muon energy was smeared with a Gaussian of 0.1..0.5 in width. The sensitivity for 0.3 and 0.5 are shown as well.

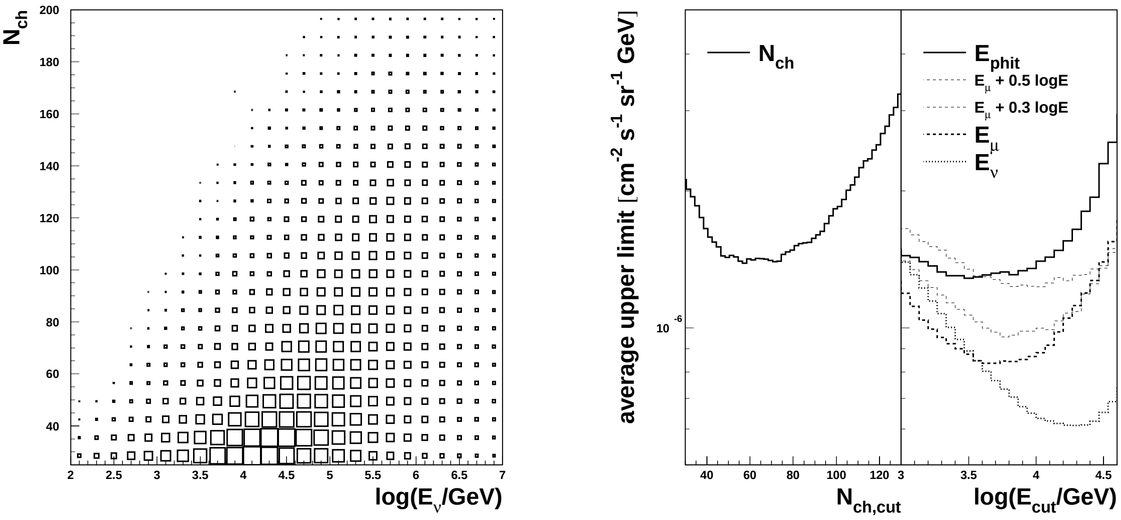

Figure 6.3: Comparison of N_{ch} and reconstructed energy E_{phit}. Left: The correlation between the number of hit channels and the true neutrino energy. Right: The average upper limit as function of N_{ch} and different energy parameters. The lowest limit was derived for the ideal but unrealistic case that the true neutrino energy would be measured. In order to see what could be reached under ideal conditions, the second lower limit was derived with the true muon energy. The thinner lines indicate what limit would be reached with a reconstruction of Gaussian error of 0.3 and 0.5 on the log of the muon energy (see text for definition). The upper line finally is derived with the reconstruction on hand. It turns out that the maximal possible gain in sensitivity ($E_\mu \pm 0.3 \log E$) is ≈33% from a simple N_{ch} estimate.

The true muon energy was used to set the stage what can be reached with an ideal energy reconstruction. The true muon energy smeared out by ±0.3 in $\log E$ marks the best possible sensitivity taking stochastics in the light production into account. The hit probability-based energy reconstruction yields about the sensitivity as the true muon energy with a Gaussian error of 0.5 in log E. The comparison to simple topological parameters showed that already the pure number of hit channels N_{ch} is a good energy parameter. The correlation between N_{ch} and the true neutrino energy is shown in the left plot of figure 6.3. The reachable limit is only 10% above the limit to be expected from the energy reconstruction. Further it turns out, that for the given selection the best possible energy reconstruction, with $\sigma(log_{10}(E_{rec}/E_\mu)) \geq 0.3$, is just one third more sensitive than the one based on N_{ch}.

Even if the true neutrino energy were accessible, the sensitivity would be only a factor 2.4 better than the one based on N_{ch}. Compared to the reconstructed energy parameter E_{phit}, the number of hit channels is a directly accessible and very simple observable. This parameter was used in an analysis presented by the BAIKAL collaboration [46] and by G. Hill to derive a preliminary upper limit [102] [2]. An analysis with a multidimensional cut optimizer revealed the

---

[2] However, the shift in the mean of the N_{ch} distribution used for that analysis makes the upper limit system-

same result: N_{ch} and E_{phit} turned out to be mostly parallel.

As a result of the comparison of the energy parameters the number of hit channels N_{ch} was chosen as energy cut parameter and analyzed systematically. The main results of the analysis of the N_{ch}-distribution will be discussed in the next section.

Another important result is that the improvement in sensitivity by the optimization of the reconstruction is very limited. Therefore the potential of a refined event selection was investigated. The result will be discussed after the analysis of the N_{ch}-distribution in section 6.4.

6.3 Data - MC Discrepancies and Limit Calculation

The comparison of the distribution of hit channels for MC and experimental data (figure 6.2) showed that the MC predicts a higher mean than observed: the mean number of hits in data is 22.6 while the atmospheric neutrino MC predicts a mean of 29.0 hit channels. Further, the tail of high multiplicities falls off faster in data than predicted. The extent of this discrepancy varies for different selections and MC versions but was confirmed by an independent analysis [100]. This discrepancy between data and MC makes a limit calculation impossible. If one places the last cut according to the highest sensitivity (lowest average upper limit) one obtains a cut position of $N_{ch} > 52$. The atmospheric neutrino MC predicts 10.1 events where none is observed in data. The probability to observe this as a downward fluctuation is $P_{pois}(0|10.1) = e^{-10.1} \approx 4 \cdot 10^{-5}$.

In order to find the underlying reason for the discrepancy, the N_{ch} distribution was analyzed in some detail [103]. The aim was to identify the source of the discrepancy in order find an appropriate way to normalize the MC to the atmospheric neutrinos observed. The following results were found:

The neutrino flux uncertainty was excluded. The 30% uncertainty of the atmospheric neutrino flux may lead to a discrepancy in the event rate. The shape of the N_{ch} distribution and the mean is not expected to change. The effect of remaining background with typically lower multiplicities could shift the mean in data to lower values. Neglecting the minor difference in the slope of the trailing edge, the ratio at multiplicities above the mean was found to be $N_{data}/N_{MC}(N_{ch} > 27) = 0.37$. This exceeds the uncertainty of the flux normalization. The flux uncertainty is therefore excluded as the source of the disagreement.

Dead or hyperactive channels: Hits in the MC that are not in data could shift the mean systematically. In order to produce a shift in N_{ch} of about one fifth of the mean it must be a strong source. The channel-based comparison between MC and data excludes individual channels as source of additional hits. The excess rather distributes over all modules.

Cut-off or filtering artefacts: The filtering procedure may reduce high multiplicity events in the data stronger than in MC. A MC sample filtered with the same quality cuts but with inverted zenith cuts was analyzed. Limited only by statistics, good agreement between

---

atically problematic.

data and MC was found up to multiplicities of 130 channels. Events up to 200 hit channels were observed. A cutoff or artefacts of the filtering procedure are therefore unlikely.

Depth-dependent optical properties could partially increase the attenuation. The comparison of MC with depth dependent optical properties to data and to an earlier MC version without depth dependency shows that even on level four the hit multiplicity reflects the depth dependence of the optical properties. However, there is no significant net effect.

Selection dependency: If the selection is based on a parameter that is not well described by the MC and correlates with N_{ch}, the shift in the mean of N_{ch}, would depend on the filter level. Experimental data, background MC, atmospheric neutrino MC and high energy neutrino MC were compared at all cut levels. A clear excess of atmospheric neutrino MC over the data at high multiplicities was already found at level 2. Here, a difference in absolute fluxes would not be visible, since the sample is dominated by atmospheric muons. The difference between MC and data therefore must have a multiplicity dependent influence, i.e. create long tails in the N_{ch} distribution of the atmospheric neutrino MC.

The sensitivity of the optical module or optical properties of the ice determine the light detection efficiency. A reduced sensitivity may result in a lower average channel multiplicity. Further, high multiplicity events will loose more hits than low multiplicity events. The reduced number of hits would distribute evenly over all depths and channels, consistent with the observation above. An overpredicted sensitivity in the MC was therefore considered the most likely source of the shift in the mean number of channels.

In order to probe the hypothesis of a too high sensitivity in MC, the N_{ch} per event was scaled with the ratio of total numbers of hits observed at level 4 by the total number of hits predicted. The ratio was found to be 0.75. The distribution of the reduced multiplicity i.e. $0.75 \cdot N_{ch}$ is shown in figure 6.4. The approximation to reduce the multiplicity of the individual event linearly is motivated by the fact that most hits ($\approx$90%) have only one photo electron. Even though this manipulation of the MC forbids stringent conclusions it serves as guide line which effects a reduced sensitivity may have. The hypothesis was supported by two results:

- The N_{ch} distribution at level four is reproduced much better (see figure 6.4).
- The contradiction between atmospheric neutrino MC prediction and data for low filter levels and high multiplicities disappears (not shown).

The scaled atmospheric neutrino MC may be seen as a likely distribution for the detector response to atmospheric neutrinos. The best guess for the detector response to a flux of $dN/dE = 10^{-5}\ E^{-2}\ \ \mathrm{cm}^{-2}\mathrm{s}^{-1}\mathrm{sr}^{-1}\mathrm{GeV}$ is given by the application of the same scaling to the high energy neutrino MC. Even though the manipulation is no basis for any further conclusions a limit was derived as a benchmark what sensitivity *could* be reached. The integrated N_{ch}-distributions are shown in figure 6.5. The average event upper limit is plotted as well. The best sensitivity is predicted for a cut at $N_{ch} > 40$. The atmospheric neutrino MC predicts 6.4 events where 7 are measured in data. The prediction for a high energy neutrino flux of $dN/dE = 10^{-5}\ E^{-2}\ \ \mathrm{cm}^{-2}\mathrm{s}^{-1}\mathrm{sr}^{-1}\mathrm{GeV}$ is 46.0 events. The upper limit therefore is

$$dN/dE \leq 1.35 \cdot 10^{-6}\ E^{-2}\ \ \mathrm{cm}^{-2}\mathrm{s}^{-1}\mathrm{sr}^{-1}\mathrm{GeV} \quad . \tag{6.5}$$

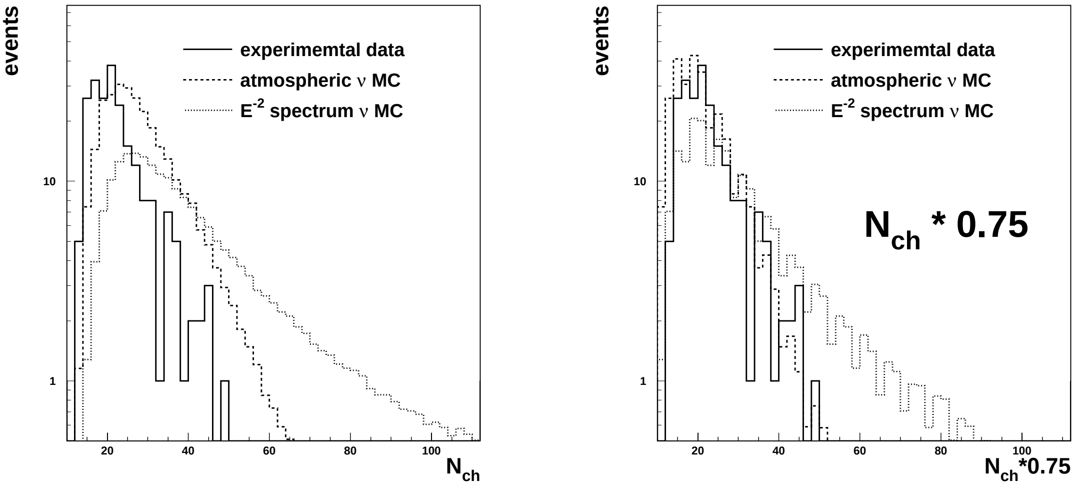

Figure 6.4: The distribution of the number of channels at neutrino separation level (level 4). Left: The number of channels N_{ch} for experimental data (continuous line), atmospheric neutrino MC (dashed line) and for a diffuse flux of $dN/dE = 10^{-5}\ E^{-2}\ \text{cm}^{-2}\text{s}^{-1}\text{sr}^{-1}\text{GeV}$ (dotted line). Right: The distribution of the scaled number of channels $0.75 \cdot N_{ch}$. The scaling moves the distribution for atmospheric neutrinos MC closer to the data. The high energy prediction is reduced accordingly. The oscillation of the scaled distribution is a binning effect due to the scaling.

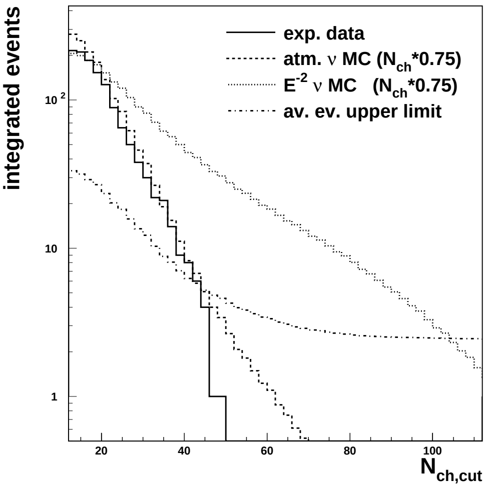

Figure 6.5: The integrated number of events for the scaled number of channels $0.75 \cdot N_{ch}$ at neutrino separation level (level 4): experimental data (continuous line), atmospheric neutrino MC (dashed line) and for a diffuse flux of $dN/dE = 10^{-5}\ E^{-2}\ \text{cm}^{-2}\text{s}^{-1}\text{sr}^{-1}\text{GeV}$ (dotted line). The dash-dotted line indicates the average event upper limit. The cut is placed where the ratio of high energy prediction and the average event upper limit is maximal.

6.4 Selection Optimization

As mentioned above, the improvement potential in the energy reconstruction was found to be limited to about 33%. Therefore, the possibility to improve the event selection instead was investigated. The analysis of the cut efficiencies shows that the first-level cut already reduces high multiplicity events to less than 20% (see figure 6.6 left plot). The cut on the velocity given by the linefit $v_{LF} > 0.1$ m/ns removes high energy events (see figure 6.6 right plot). This effect is understood: high energy events have a larger radial extension. The radial time development is relatively strong compared to the light field of a relatively faint minimum ionizing muon, which is much longer than wide. The time development of the hit pattern in direction of the track that influences the velocity of the linefit is therefore less directed. Even at cut level-4 atmospheric neutrinos are reduced by 22% and high energy neutrinos by 36% *exclusively* due to this filter cut. In other words, the omission of the v_{LF}-cut increases the selection efficiency at cut level-4 by roughly one quarter for atmospheric neutrinos and by one third for high energy neutrinos.

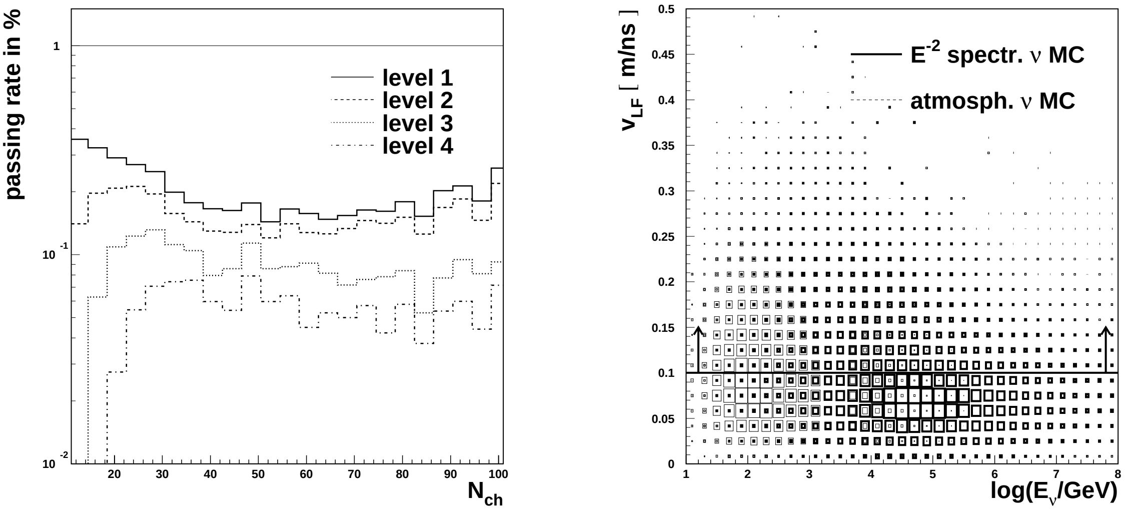

Figure 6.6: The effect of the cut on the velocity given by the linefit: Left: The passing rate for high energy signal (E^{-2}-spectrum) as a function of hit multiplicity for the four cut levels. Already the first cut level reduced the sample especially at multiplicities larger than 30. Right: The distribution of the velocity given by the linefit against the logarithm of the true neutrino energy. The cut at 0.1 reduces a large fraction of both samples. At the final cut level the reduction due to the v_{LF} cut is 22% for atmospheric neutrinos and 36% for high energy neutrinos.

6.5 Conclusion

The comparison of possible energy selection parameters yields N_{ch} as a simple and efficient cut parameter. However, following the atmospheric neutrino selection, it can not be used to derive a limit because the mean is systematically shifted to higher multiplicities in MC. Due to the strong correlation of N_{ch} with the muon energy, the choice of another parameter does not solve the problem. From the analysis of the shift at all cut levels, a too high simulated sensitivity was proposed as reason. This hypothesis is supported by a later analysis with varied simulated sensitivities [104] and a newly developed MC with a changed angular dependence of the sensitivity of the optical modules [105].

In order to quantify the potential for a limit based on the atmospheric neutrino selection and the number of hit channels as energy parameter a *"benchmark limit"* was derived with a manipulated MC. Atmospheric neutrino MC and high energy MC were scaled the same way, according to the total number of hits at final cut level. After that good agreement between atmospheric neutrino MC and experimental data was found. From the scaled high energy prediction a limit of $d\Phi/dE \leq 1.35 \cdot 10^{-6}\ E^{-2}\ \ \mathrm{cm}^{-2}\mathrm{s}^{-1}\mathrm{sr}^{-1}\mathrm{GeV}$ was derived.

The analysis of the acceptance for high energy neutrinos shows that especially high multiplicity events are poorly recovered. Already the first cut level contains a cut that affects the final sample size considerably. The maximum gain from an improved energy reconstruction at atmospheric neutrino selection level is only 33%, but this selection is not efficient for high energy events. Therefore a dedicated high energy event selection was developed.

Meanwhile a MC with varied angular sensitivity that reduces the systematic discrepancies was available. The further analysis is therefore based on this MC.

Chapter 7

Flux limit based on high energy ν selection

7.1 Motivation

It is obvious that an optimization on the total number of events for a steeply falling energy spectrum is dominated by the large low energy fraction of the events. The acceptance for the high energy tail of the spectrum may be sacrificed for the sake of the low energy majority. For the atmospheric neutrino analysis this was clearly the case. An analysis of the losses showed that a very early cut, the cut on the velocity given by the linefit, v_{LF}, reduced the high energy signal expectation considerably. A separate dedicated high energy separation was therefore performed starting with an alternative filter which did not contain this cut.

Cross talk cleaning A problem that turned out during the atmospheric neutrino analysis was unsimulated background. Because it most clearly peaks in the z component of the center of gravity it was baptized the cog_z-background. The analysis of this background yielded a number of explanations, none of them able to explain the full picture.

- Artefacts as sparking modules were disfavored by the cascade fit. For sparks it is expected to converge to single module locations but yielded locations outside of the detector.
- A fraction of the cog_z-events was successfully simulated by the introduction of depth-dependent ice properties [98, 86]. Rejection for this fraction of the background could be documented with the MC.
- Another fraction was found to be cross talk together with bright shower events, most likely from down going muons [106]. The intense light signal causes cross talk, possibly due to pick-up signals in the cable to the surface. It arrives at the surface simultaneously with the initial pulse and is shifted by the calibration, faking the timing pattern of an upward moving particle.

For the last class of events a dedicated hit filter was developed in [100]. It is based on the characteristic small width-to-height-ratio of cross talk hits. The filtering of the suspicious hits avoids a possible confusion of the reconstruction. The background then is reduced with a cut on the correctly reconstructed zenith angle. The cross talk hit filter was applied to the high energy event selection before higher level reconstructions.

7.2 High Energy Neutrino Filter

In the following four samples are distinguished. For convenience the following naming is used: experimental data - short data, downgoing atmospheric muon background MC - short background MC or BGMC, atmospheric neutrino MC, and extraterrestrial high energy neutrino MC for a diffuse isotropic (2π) flux of $d\Phi/dE = 10^{-5}\ E^{-2}\ \ \mathrm{cm}^{-2}\mathrm{s}^{-1}\mathrm{sr}^{-1}\mathrm{GeV}$ - short high energy MC. Of course all neutrinos considered in this analysis have high energies compared to e.g. solar neutrinos. However, the naming high energy neutrino is used in contrast to the relatively low energetic majority of the atmospheric neutrinos.

Filter (Level 1)

As shown in the previous chapter, the atmospheric neutrino selection rejects a large fraction of the high energy events already at the first cut level. The high energy neutrino selection is therefore based on another filter developed in Berkeley [107] that did not contain the cut on the velocity given by the linefit but just three filter cuts:

$$\begin{aligned} \theta_{LF} &\geq 50^\circ \\ \theta_{LH} &\geq 80^\circ \\ N_{dir}^{-15..20} &\geq 3 \end{aligned} \tag{7.1}$$

These cuts are passed by 2.1% of the data, 2.0% of the downgoing muon MC, 55% of the atmospheric neutrino MC and 48% of the high energy neutrino MC.

Hit Selection

The further processing was developed in analogy to the experience from the atmospheric analysis, but with focus on the high energy events. The same hit cleaning procedure as described in section 6.1 was applied. Further the dedicated cross-talk cleaning described above was applied. Afterward only events with more than 25 hit channels were considered in order to concentrate on high energy tails:

$$N_{ch} > 25$$

This is a rather strong cut. Compared to the previous filter level, 90% of experimental data and background MC are rejected. At the same time nearly 90% of the atmospheric neutrino expectation is rejected and even the high energy neutrino expectation is reduced to about 50%. However, the cut is well motivated by the fact that only in the very high energy fraction of the events a possible excess of neutrinos from an E^{-2} spectrum is observable. At low multiplicities the number of atmospheric neutrino events exceeds the number of events from an E^{-2}-spectrum. The location where the latter exceeds the atmospheric neutrino events depends on the assumed flux. For the relatively high simulated flux of $d\Phi/dE = 10^{-5}\ E^{-2}\ \ \mathrm{cm}^{-2}\mathrm{s}^{-1}\mathrm{sr}^{-1}\mathrm{GeV}$ it is at about 35 channels (at the present cut level). The cut at 25 is therefore acceptable. It efficiently reduces the data set, because most of the data are taken close to the multiplicity threshold. After the N_{ch} cut the total efficiency for experimental data is $1.7{\cdot}10^{-3}$, for the atmospheric muon MC $1.1{\cdot}10^{-3}$, for the atmospheric neutrino MC 5.9% and 23.6% for the high energy neutrino MC.

Level 2

Filter level 2 is based on a likelihood track fit with six iterations ($LHi6$) that uses only the hits accepted by the two hit filters above. The rejection effect of the cross-talk hit cleaning is mainly based on the now (more likely) correctly reconstructed zenith angle, θ_{LHi6}. Therefore the filter cuts are basically a reapplication of the previous zenith angle cut, with a weak quality cut on the likelihood parameter L_{LHi6} and the direct length of the reconstructed track $L_{dir,LHi6}^{-15..+25ns}$. For high multiplicity events, the track fit yields better likelihood results than for low multiplicity events. The cut on the likelihood parameter can therefore be placed significantly harder than for atmospheric neutrinos.

$$\begin{aligned} \theta_{LHi6} &> 80^\circ \\ L_{LHi6} &< 7.8 \\ L_{dir,LHi6}^{-15..+25ns} &> 75\ \mathrm{m} \end{aligned} \tag{7.2}$$

Level 3

Filter level three is based on a likelihood track fit with 16 iterations. Again, cuts on the reconstructed zenith and the direct length are applied.

$$\begin{aligned} \theta_{LHi16} &> 85^\circ \\ L_{dir,LHi16}^{-15..+25ns} &> 90\ \mathrm{m} \end{aligned} \tag{7.3}$$

Finally, three further fits were applied as basis for the final event selection. A likelihood energy fit, based on the hit probability, was applied for comparison with the N_{ch}-based selection. The tensor of inertia was calculated as a topological parameter to reject spherical events. And finally the likelihood cascade fit was applied, in order to identify spherical events with bad directional information.

After the last filter cuts (cut level 3) 21 508 events were left in data and 14 450 events are predicted from atmospheric muon background MC. From atmospheric neutrinos 162.4 events are expected, and for a flux of $10^{-5}\ E^{-2}\ \ \mathrm{cm}^{-2}\mathrm{s}^{-1}\mathrm{sr}^{-1}\mathrm{GeV}$, 391.2 events. This corresponds to a filtering efficiency of $2.1\ {\cdot}10^{-5}$ for data, $1.6\ {\cdot}10^{-5}$ for background MC, 2.9% for atmospheric neutrinos and 10.9% for high energy neutrinos. The passing rates are summarized in table 7.1.

Note that these efficiencies include the energy dependent preselection already. The comparison to the atmospheric neutrino selection has to take the energy dependence into account. Even the N_{ch} distribution is not comparable because of the more stringent hit selection used in the high energy event selection.

Filter level	exp. data	atm. μ BG MC	atm. ν MC	high energy ν MC $10^{-5}\ E^{-2}\ \mathrm{cm}^{-2}\mathrm{s}^{-1}\mathrm{sr}^{-1}\mathrm{GeV}$
Trigger	$1.05 \cdot 10^{9}$	$9.03 \cdot 10^{8}$	5 677.3	3 574.1
ϵ Level 1	$2.09 \cdot 10^{-2}$	$2.04 \cdot 10^{-2}$	54.9%	48.0%
$\epsilon N_{ch} > 25$	$1.71 \cdot 10^{-3}$	$1.09 \cdot 10^{-3}$	5.95%	23.6%
ϵ Level 2	$6.68 \cdot 10^{-5}$	$5.29 \cdot 10^{-5}$	3.20%	12.7%
ϵ Level 3	$2.06 \cdot 10^{-5}$	$1.60 \cdot 10^{-5}$	2.86%	10.9%
events after filtering	21 508	14 450	162.4	391.2
ϵ Level 4	$6.57 \cdot 10^{-8}$	$2.97 \cdot 10^{-10}$	1.06%	2.99%
events final level	69	0.4 ± 0.3	60.4 ± 1.5	107.2 ± 0.9
$\epsilon N_{ch} > 53$	$2.89 \cdot 10^{-9}$	0.00	$5.49 \cdot 10^{-4}$	1.33%
events $N_{ch} > 53$	3	-	3.12 ± 0.18	47.8 ± 0.52

Table 7.1: The high energy neutrino selection: number of triggers, cut efficiencies and final number of events in experimental data, atmospheric muon background MC, atmospheric neutrino MC and high energy neutrino MC. The MC is normalized to 130 days of life time. The details of the filter levels are discussed in the text.

The further cuts were developed with the cut optimization tool introduced in section 5.3.

7.3 Cut Selection

The cut optimization tool `cuteval` automatically finds the optimum of an optimization function in a cut parameter space. This allows to systematically compare cuts according to their selection power for this optimization function. Common optimization functions are the ratio of signal to background (SIG/BG) or signal to square root background ($SIG/\sqrt{BG}$). It has been used to extract a set of independent (not parallel) cut parameters from a pool of possible parameters. The list of cuts investigated, contained selection cuts, as reconstructed zenith angle and energy, and a variety of quality cuts as the likelihood parameters of the track-, energy- and cascade fits, the ratio of likelihood parameters, direct length, number of direct hits, smoothness parameters and the average hit probabilities. For systematic reasons the true muon energy and neutrino energy were always kept for best case comparisons. For the definition of the cut parameters see section 5.2.

7.3.1 Optimization Functions

For the high energy selection four optimization functions (modes) have been analyzed. Two of them were set up to separate atmospheric neutrinos. The two other modes were developed to optimize the high energy response only. In the following description $DATA$ stands for experimental data, $ATMU$ for atmospheric muon background MC, $ATNU$ for atmospheric neutrino

MC and $AGNU$ for neutrinos from an E^{-2} spectrum of flux 10^{-5} E^{-2} $\mathrm{cm^{-2}s^{-1}sr^{-1}GeV}$.

$ATNU/\sqrt{ATMU}$ As a proof of principle, the signal to square root background ratio for **atmospheric neutrinos** vs. atmospheric muons was optimized. The event classes are represented by the MC samples normalized to 130 days of lifetime. This mode selects cuts that accept events compatible with the predicted signal and suppresses backgrounds that are described by the MC.

$ATNU/\sqrt{DATA - ATNU}$ This mode was developed as systematic comparison of experimental data and MC. Atmospheric neutrino MC is used as signal. The difference between experimental data and signal MC is considered background. This mode finds cuts that select events from experimental data, that are compatible with atmospheric neutrinos and suppress events that are different. It is suitable to identify unsimulated background. The optimization function is maximal, if all events left in experimental data are equal to the atmospheric neutrino prediction. Note that the use of experimental data in the cut development has the potential to optimize on fluctuations. However, by comparing the selected cut parameters to the result of the purely MC based mode above, data and MC can be compared systematically. There is yet another misleading potential in this mode. It may select cuts that separate background events that look like signal only in the observed parameter space. This way the data can be 'shaped' like signal by selecting background classes that are close to signal MC. Therefore, the results of this mode need to be checked independently for background contamination.

$AGNU/\sqrt{ATMU + ATNU}$ The third mode optimizes the sensitivity to events as expected from an E^{-2}-spectrum. The selection suppresses atmospheric muons and atmospheric neutrinos.

$SIGNIF(AGNU)$ The final, most consequent mode optimizes the sensitivity directly. As measure of the sensitivity the ratio $AGNU/FC(ATMU + ATNU)$ is used, where FC stands for the event average upper limit as defined in section 5.4. The difference to the mode above is that the average event upper limit converges to a minimal constant value (2.44) for the case of vanishing background. This way the optimization on very small square roots of background is avoided that may deliver misleadingly good value of signal to square root of background.

7.3.2 Cut Sets

As a result of the optimization, for each mode a minimal complete parameter set and the according cut positions are found. The following list shows the best cut parameters found for each mode. The cut parameters are sorted according to their selection power. For a detailed introduction of the cut parameters see section 5.2.

$ATNU/\sqrt{ATMU}$

1.	θ_{LHi16}	(-)	zenith of the likelihood track reconstruction
2.	L_{casc}/L_{track}	(29.5)	ratio of the likelihood parameters for cascade and track fit
3.	S_{phit}	(56.3)	smoothness weighted with hit probability
4.	$I_1/I_{123}(\theta)$	(62.4)	zenith dependent sphericity parameter (ratio of the eigenvalues of the tensor of inertia)
5.	S_{vnrl}	(63.7)	average of four smoothness flavors

$ATNU/\sqrt{DATA - ATNU}$

1.	θ_{LHi16}	(-)	zenith of the likelihood track reconstruction
2.	L_{casc}/L_{track}	(107.4)	ratio of the likelihood parameters for cascade and track fit
3.	S_{phph}	(131.1)	smoothness weighted with hit probability, averaged for direct hits and all hits
4.	cog_z^{min}	(135.1)	the maximal depth (min. z-position) of the center of gravity

$AGNU/\sqrt{ATMU + ATNU}$

1.	θ_{LHi16}	(-)	zenith of the likelihood track reconstruction
2.	N_{ch}	(12.9)	number of hit channels
3.	L_{casc}/L_{track}	(16.9)	ratio of the likelihood parameters for cascade and track fit
4.	P_{hit}	(18.5)	average hit probability of hit modules
5.	S_{phvan}	(18.6)	smoothness parameter, averaged of two flavors: time only flavor and hit probability weighted flavor

$SIGNIF(AGNU)$

1.	θ_{LHi16}	(-)	zenith of the likelihood track reconstruction
2.	P_{hit}	(16.7)	average hit probability of hit modules
3.	L_{casc}/L_{track}	(22.5)	ratio of the likelihood parameters for cascade and track fit
4.	P_{nohit}	(24.9)	average probability to record no hit of non-hit modules
5.	E_{phit}	(26.4)	reconstructed energy

The number in brackets gives the value of the optimization function when the parameter under consideration and all preceeding parameters are used. The increase of the value is a measure for the additional selection power, gained by the use of this cut, in addition to the previous cuts. The development of the value nicely shows the importance of the second and third cut parameter. The gain by the fifth cut is comparatively small. For three of the four modes the procedure converges after five, or even four, parameters. Any additional cut just reduces the signal without gain in the optimization function. The absolute value depends on normalization details.

The zenith angle of the likelihood track reconstruction was set in advance because it is the most important parameter for any neutrino separation. However, all four modes converge to a zenith angle cut position between 100° and 110° (horizon $= 90^\circ$). The cut just below the horizon is expected and confirms the proper work of the optimizer.

Further, all four modes select the ratio of the likelihood of cascade and track fit as cut parameter. For the two atmospheric neutrino modes it is at second position, i.e. most important after the zenith angle cut, and for the high energy selection it is at position three. This cut rejects spherical events that are much more likely caused by high energetic cascades induced by downgoing muons. Especially the agreement in the purely MC based first mode and the partially data based second mode is a nice confirmation that spherical events are an important background class. The high ranking in all four modes shows that the likelihood ratio is a powerful (muon) neutrino selection cut.

For the high energy modes an energy sensitive parameter is the second most important. This is consistent with expectation but shows nicely how the optimization works. The number of hit channels, N_{ch}, and the hit probability, P_{hit}, are both correlated with the muon energy. The first is obvious: more secondary processes produce more light and more modules can be hit. The second is due to the fact, that a relatively faint track has a small cylinder where the hit probability is saturated (close to unity). The combined hit probability is dominated by modules in the transition region were P_{hit} is neither 0 nor 1. In contrast a brighter track has a relatively large light cylinder. The fraction of modules in the saturated region is relatively large and the average hit probability accordingly high. The selection of the energy sensitive parameters is consistent with the optimization on the high energy tail where the excess of $AGNU$ is expected.

Three of the four modes select smoothness parameters. Both atmospheric neutrinos selections yield a smoothness parameter at third position. The smoothness characterizes the continuity of the hit pattern. A gap-free light pattern is an indication of a continuous emission as opposed to two independent light sources as for example shower plus noise (cross talk, dark noise) or two independent showers. The smoothness parameters have proven very powerful in the atmospheric neutrino analysis. Note that both atmospheric neutrino modes select a smoothness flavor that takes the hit probability into account. The hit probability is not used by the track reconstructions applied here. So the information of the probability was still unexploited.

Finally, the two atmospheric neutrino modes yield different cuts at the fourth position. The data-based mode selects a cut on the center of gravity, where as the MC-based mode selects another sphericity cut, the ratio of the eigenvalues of the tensor of inertia in some zenith angle dependence. This dependence is due to the geometry of the detector. Since it is much taller than wide, horizontal events are bound to be more spherical than vertical tracks. The selection of the cog_z cut in the data-based mode is an indication of an unsimulated background. A background that clearly peaks at top middle and bottom of the detector was found by the (low energy) atmospheric neutrino analysis. The same structure was found here and will be discussed in the next section.

The remaining parameters are smoothness parameters, and in the high energy modes again energy selection parameters. The little gain in selection power of the last cut parameters limits the conclusions that can be drawn.

7.3.3 Cut Extrapolation

Another way to use the optimizer is the cut extrapolation. By constraining the optimization to leave a minimum number of background MC events in the sample, one finds an optimum at a low rejection level. Stepwise, the minimum number of events can be reduced. The path of consecutive optima can be used to inter- and extrapolate cut positions. The development of the sample sizes along this path of strengthened cuts is an instructive systematic check for the behavior of event classes. Furthermore, cut positions can be defined for background levels beyond the simulated level of statistical precision. Even though the cut positions then are not justified by MC, it is a well motivated guess for an increasingly restrictive event selection. The observation of the efficiencies beyond the level of background MC description is especially useful for the comparison of experimental data and signal MC.

For the parameter set selected with the first optimization mode a cut parameterization was derived. The five cuts were optimized at 16 different minimum numbers of background events (N_{BG}). The obtained cut positions are shown as a function of the left background in figure 7.1.

For linearly independent cuts and exponentially falling background one expects a linear dependence of the cut position of $\log(N_{BG})$. For the two most important cuts, zenith angle and the likelihood ratio, this dependence is nicely reproduced. With increasing rejection, i.e. decreasing background expectation (right to left in the plot) the zenith cut (θ_{LHi16}) develops from 10° above horizon to 20° below horizon. As the major background is atmospheric muons leaking below the horizon, a zenith cut harder than 90° is reasonable. For comparison see figure 7.6 top right. For the likelihood ratio (L_{casc}/L_{track}) the cut position develops from 0.9 to about 1.0, corresponding to increasingly track-like and less cascade-like events. For the smoothness (S_{phit}) and the zenith dependent sphericity ($I_1/I_{123}(\theta)$) fluctuations are stronger than the background dependence. The sphericity shows a weak development towards elongated hit patterns consistent with the selection of tracks and rejection of cascade like events. The fifth parameter, the averaged smoothness (S_{vnrl}) depends on the background only for low rejection levels. At higher rejection levels it remains nearly constant. This is consistent with the little cut power which this parameter added in the cut selection procedure discussed in the previous section.

Together with the cut development, the result of a linear fit is plotted in figure 7.1. The fit range was chosen somewhat arbitraryly. Because the final cuts will be close to the highest rejection level, the reproduction of the cuts at higher rejection is more important than the precise description of the cut position over the hole range. The parameterization describes just one possible path to the final cut set.

The combination of all five cuts is used to define a quality parameter that depends only of the number of expected background events. Symbolically one can write:

$$\begin{aligned} Q(N_{BG}) &= \theta_{LH} > \theta_{LH}(N_{BG}) \\ &\& \; L_{casc}/L_{track} > L_{casc}/L_{track}(N_{BG}) \\ &\& \; S_{phit} < S_{phit}(N_{BG}) \\ &\& \; I_1/I_{123} > I_1/I_{123}(N_{BG}) \\ &\& \; S_{vnrl} < S_{vnrl}(N_{BG}) \end{aligned} \tag{7.4}$$

The number of events that pass a given quality requirement are shown in figure 7.2. The number of events in experimental data, background MC, atmospheric neutrino MC and high energy neutrino MC are plotted. Quality 0 is similar to filter level 3. The background MC was renormalized to the number of events in the experimental data. The top panel shows the sample development as a function of the quality requirement. In the middle panel a generic energy cut

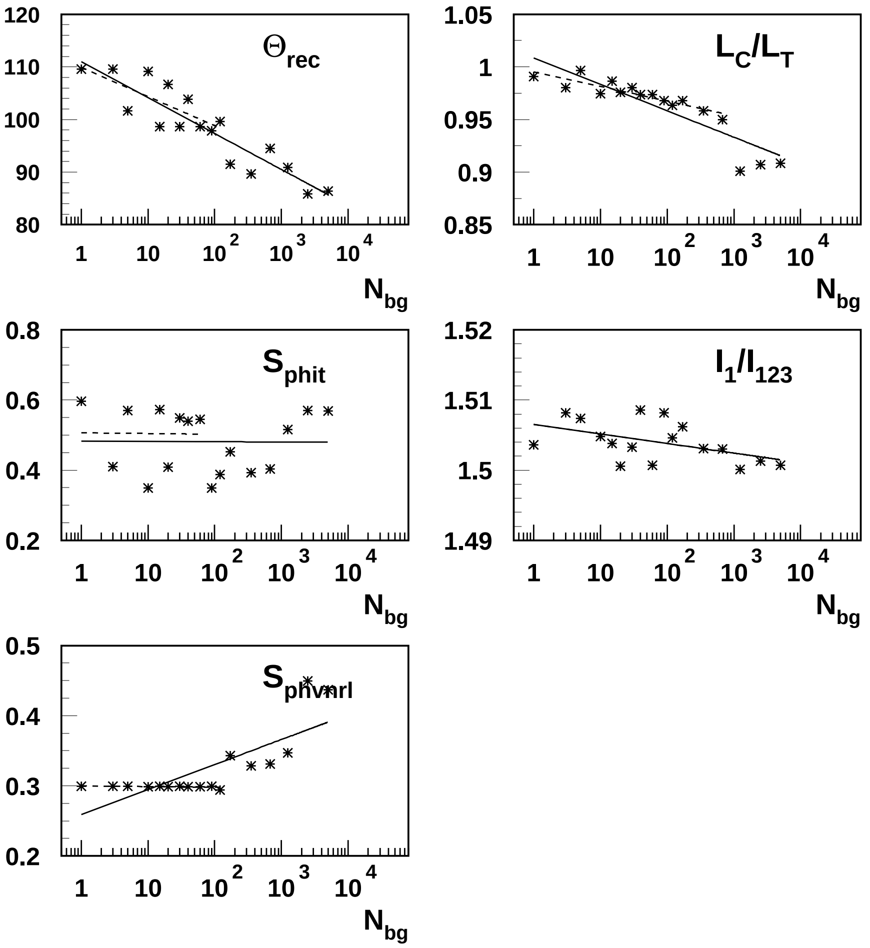

Figure 7.1: The five best cuts for atmospheric neutrino selection as a function of the remaining background (see text for further explanation). The lines indicate the parameterization used for the definition of the quality parameter. The full line indicates the result of a linear fit to all data points, the dashed line indicates the fit used as parameterization of the cut.

was applied. The third panel shows the sensitivity to an *AGNU* signal with *ATNU* and *ATMU* as background.

In the upper plot the background MC falls as expected from definition about exponentially with quality. The small deviation from a pure exponential is due to the imperfect parameterization. Atmospheric neutrino prediction and high energy neutrino prediction fall with increasing quality as well, but at a lower rate. Therefore at a quality of about ten they exceed the number of background events expected. Whereas background keeps falling exponentially they show a higher resistivity against increasing quality requirements. The experimental data now show

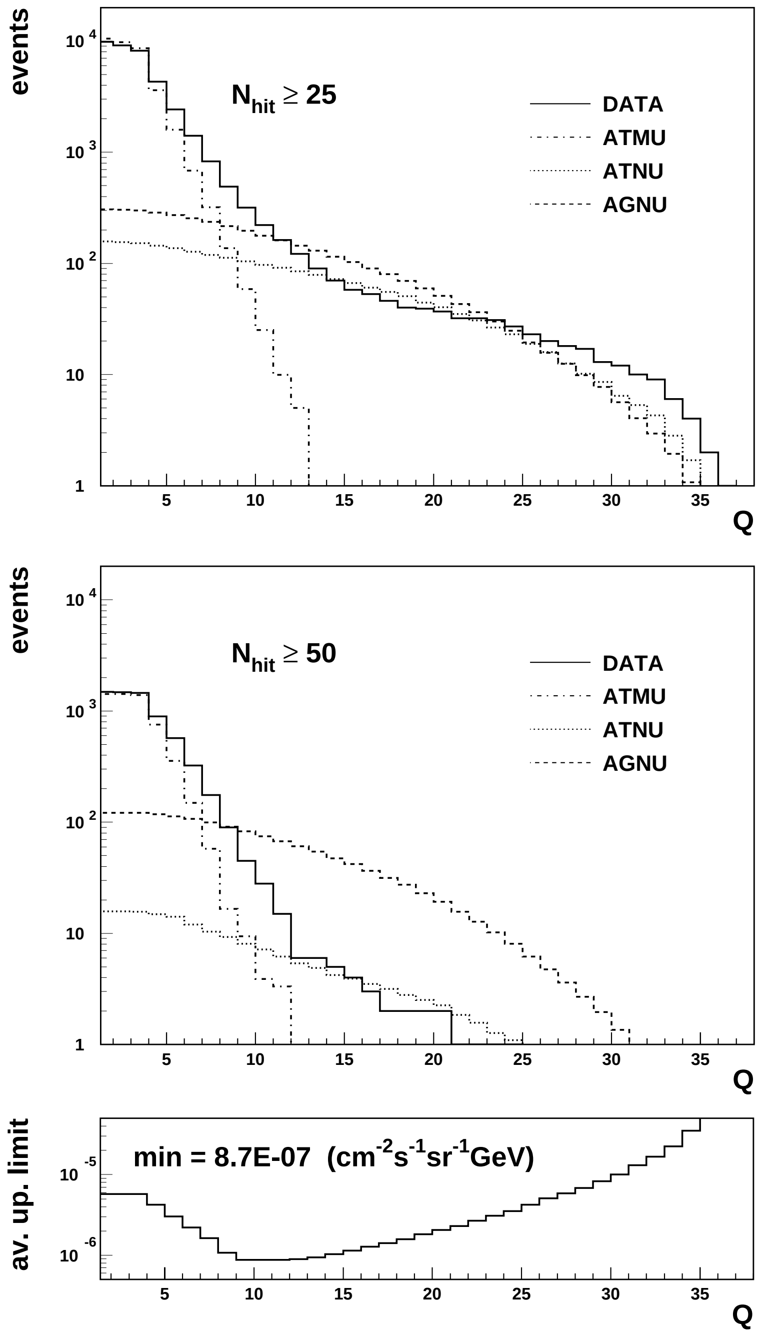

Figure 7.2: Number of remaining events as a function of event quality. The top plot contains no energy cut, therefore atmospheric and high energy neutrinos are expected at the same level. The middle plot contains an generic energy cut at $N_{ch} > 50$: the high energy neutrino prediction exceeds the atmospheric neutrino prediction. The bottom plot shows the average upper limit (sensitivity).

two different quality dependencies. At low quality they follow the background expectation. At about the level where atmospheric neutrinos are expected, they change in slope and start to follow the neutrino prediction. This change in slope is a strong indication for a class of events in experimental data, that have a quality distribution as atmospheric neutrinos. However, there are discrepancies as well: at event quality 10 there are more events in data than expected from background and atmospheric neutrinos. This is an indication of an additional event class. It was found that at this level the experimental data are dominated by an unsimulated background. It will be discussed in more detail in the next section. Another discrepancy between MC and experimental data is observed at high quality levels ($Q = 30..35$). There are again more events in data than expected from atmospheric neutrinos and high energy neutrinos. This excess was observed by one of the atmospheric neutrino analyses as well and is not resolved. The contamination by an unsimulated background is possible but at these quality levels very unlikely. A more likely explanation are systematic uncertainties of the MC in the percent range.

Note, that in the top panel, at no quality level high energy neutrinos exceed the expectation from atmospheric neutrinos. This is simply due to the fact that the cut set was optimized for atmospheric neutrinos and no additional energy selection was applied so far. In the middle plot a generic energy cut at the number of hit channels N_{ch} was applied. While background MC and atmospheric neutrino prediction are reduced by a factor of about ten at all quality levels, the high energy neutrino prediction looses only 50%. Experimental data again are found to follow the background MC and later the atmospheric neutrino MC. At quality levels above 12 the observation is consistent with the prediction from atmospheric neutrinos. No indication for an additional high energy component is observed at this approximate level.

The third of the three panels shows the sensitivity to neutrinos from an E^{-2} flux (average upper limit) that can be reached at this quality level if an additional cut on the number of hit channels is applied at the optimal position. In this case atmospheric neutrinos and the background MC (atmospheric muons) are considered background. The sensitivity clearly dips where the most signal is kept and background is sufficiently suppressed. The best sensitivity of about $0.9 \cdot 10^{-6}\ E^{-2}\ \mathrm{cm}^{-2}\mathrm{s}^{-1}\mathrm{sr}^{-1}\mathrm{GeV}$ is reached at about $Q = 10$. At lower quality levels the background dominates a possible high energy signal, at higher quality levels the signal is reduced, both resulting in a lower sensitivity. However, at the preferred quality region the experimental data are not described by the sum of background and atmospheric neutrino MC.

Conclusions: With a cut parameter set optimized for the selection of atmospheric neutrinos a clear indication of an event class consistent with atmospheric neutrinos was found in data. No indication of an additional high energy component was found so far. With one additional energy-related cut a sensitivity of $0.9 \cdot 10^{-6}\ E^{-2}\ \mathrm{cm}^{-2}\mathrm{s}^{-1}\mathrm{sr}^{-1}\mathrm{GeV}$ is predicted from MC. An indication of an MC-data discrepancy was found at the quality level corresponding to the best sensitivity. Even though for higher energies this discrepancy seems to disappear, data and MC will be compared in the next section and an alternative event selection developed.

7.4 High Energy ν Selection

The class of unsimulated events that dominates the experimental data is most clearly visible in the z-component of the center of the gravity (cog_z). The distributions for experimental data, background MC, atmospheric neutrino MC and high energy MC at filter level 3 are shown in figure 7.3 (lower left). The data clearly show three peaks at top, middle and bottom of the array. The background MC shows a triple peak structure as well, but much less pronounced.

This cog_z-event class was discovered during the atmospheric neutrino analysis and studied in many analyses since. The source is not completely clear. A fraction could be explained by depth-dependent ice properties. Another fraction was identified as shower-like events accompanied by cross talk hits. The dedicated hit cleaning, together with a refit based on the selected hits, rejected a large fraction of these events at filter level 2. However, at filter level 3 there are still enough events to clearly show the characteristic triple peak structure in cog_z.

Together with the center of gravity distribution, distributions of the most important selection parameters found by the cut selection described in section 7.3 are shown in figure 7.3: zenith angle θ_{LHi16} for downgoing muon rejection, the number of hit channels N_{ch} for atmospheric neutrino rejection, and finally the likelihood ratio of cascade fit and 16-fold iterative track fit L_{casc}/L_{track}. Their shape is well reproduced by the sum of background and atmospheric neutrino MC. The background MC has been scaled up by a factor 1.5 to the number of experimental data at filter level 3. This is conservative concerning the background estimation by MC, i.e., the background at higher cut levels is rather over estimated.

The golden way to separate a signal is to identify and reject background event classes based on the different nature of their source. However, an upper limit can be derived as well based on a phenomenological rejection of background and the non-observation of a predicted signal. Again, the signal prediction can be tested most reliably with a guaranteed source. The strategy therefore will be to reduce the cog_z events by their topology and maintain the atmospheric and high energy neutrino prediction as well as possible in order to see that the detector is sensitive to the test beam of atmospheric neutrinos.

The likelihood ratio ($L_{casc}/L_{track} > 1.02$)

It turns out that the cog_z events tend to have more spherical hit patterns. The likelihood ratio of cascade and track likelihood fit was found efficient for shower (cascade) like events during cut selection. The distribution of the likelihood ratio is shown in figure 7.5. There is a clear change of slope at 1.05. The huge bump to the left is described by background MC. The tail to the right only by signal. The correlation between cog_z and the likelihood ratio is shown in figure 7.4. The triple peak structure in data, as well as all simulated backgrounds is clearly concentrated at small likelihood ratios.

Atmospheric and high energy neutrino MC extend to likelihood ratios larger unity at all depths. At about a ratio of 1.05 the range in cog_z is limited by the detector geometry. Events with most hits close to the detector bottom are most likely horizontal tracks, since vertical

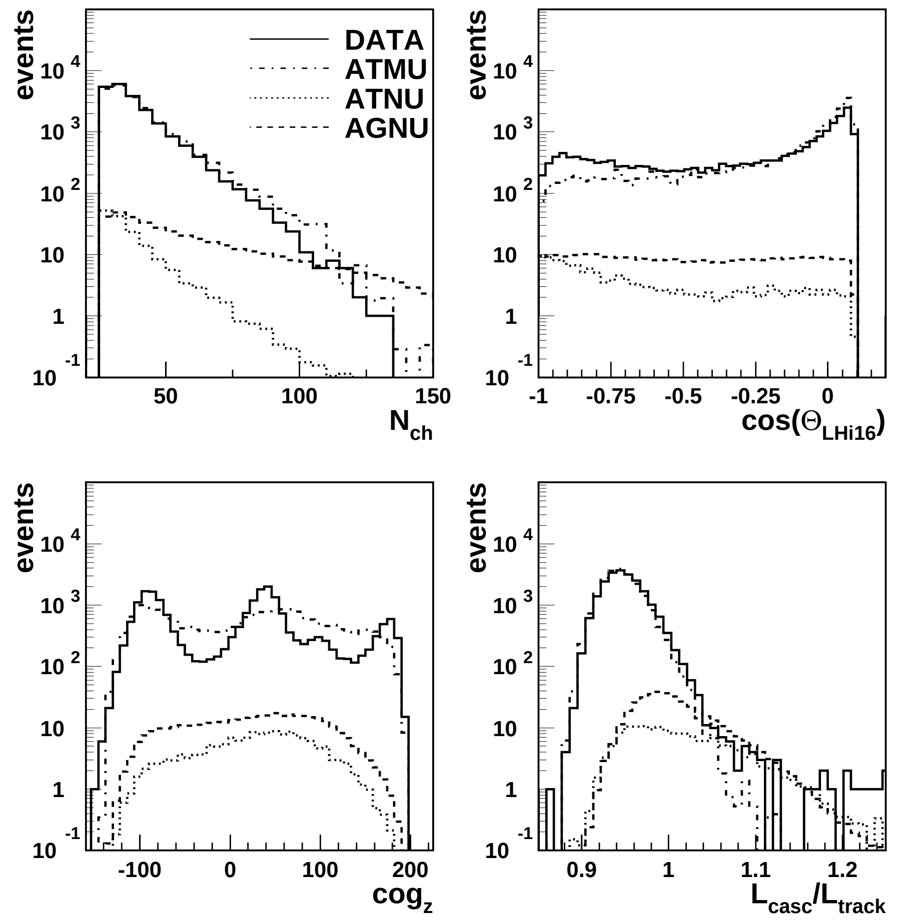

Figure 7.3: The four last cut parameters at filter level 3. The cog_z-distribution together with the two separation cuts zenith angle θ_{LHi16} and number of hit channels N_{ch} and the best cog_z rejection cut: The ratio of the likelihood parameters for cascade and track fit L_{casc}/L_{track}. The background MC is normalized to the data. The normalization to number of triggers yields a factor 1.5 lower BG prediction.

tracks would create hits further up as well. However, horizontal tracks cross relatively little instrumented volume. The width of the detector is close to the width of the light pattern resulting in a more spherical hit distribution. This effect increases with hit multiplicity. In contrast to the neutrino MC the muon background MC concentrates at low likelihood ratios. This is understood because elongated downgoing hit patterns can easily be identified as downgoing muons and are already rejected. The fakes therefore concentrate at small likelihood ratios.

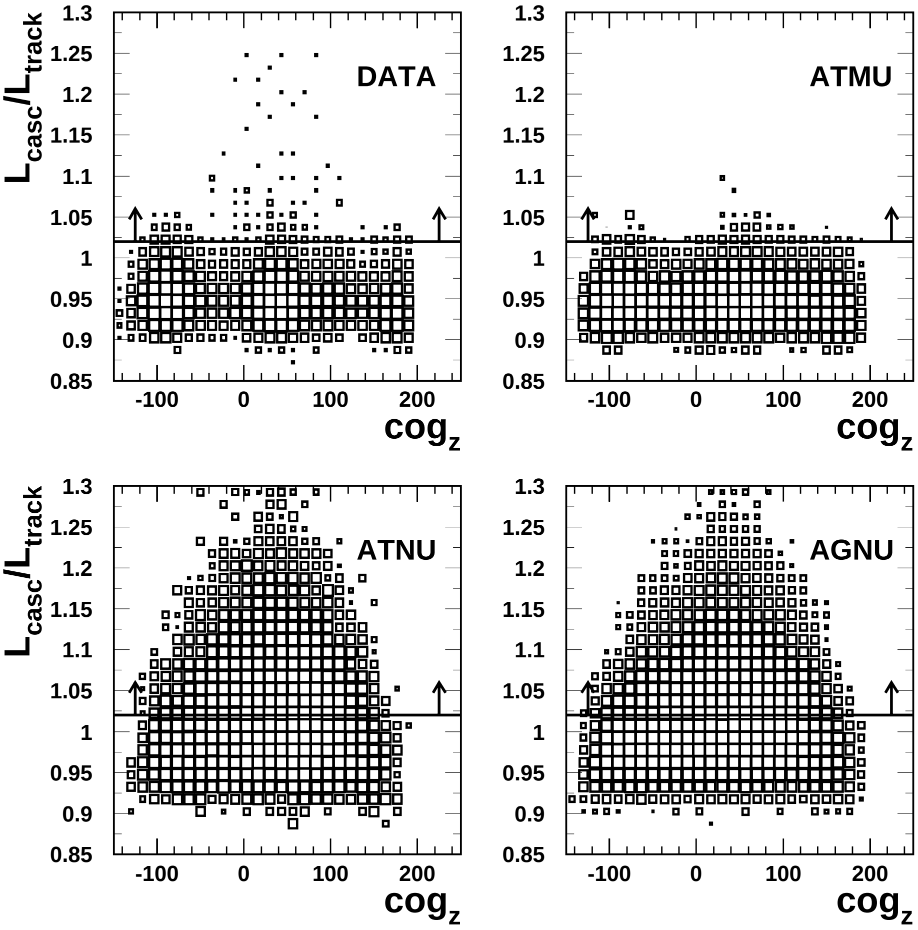

Figure 7.4: The cog_z rejection cut: The correlation between cog_z and the ratio of the likelihood parameters for the cascade and track fit.

The MC based cut optimization of mode one proposes a cut at $L_{casc}/L_{track} > 0.98$. A slightly harder cut at $L_{casc}/L_{track} > 1.02$ rejects most of the cog_z-background (figure 7.4). After this cut the cog_z distribution for data agrees much better with MC (figure 7.5). The triple peak structure is clearly seen in the background MC. The left part of the middle peak is reproduced by the atmospheric neutrino MC.

The center of gravity $(-50 \text{ m} < cog_z < 140 \text{ m})$

The cut in cog_z is applied against so called corner clippers at top and bottom of the array. These are mostly horizontal events that just pass near the detector without penetrating deeply

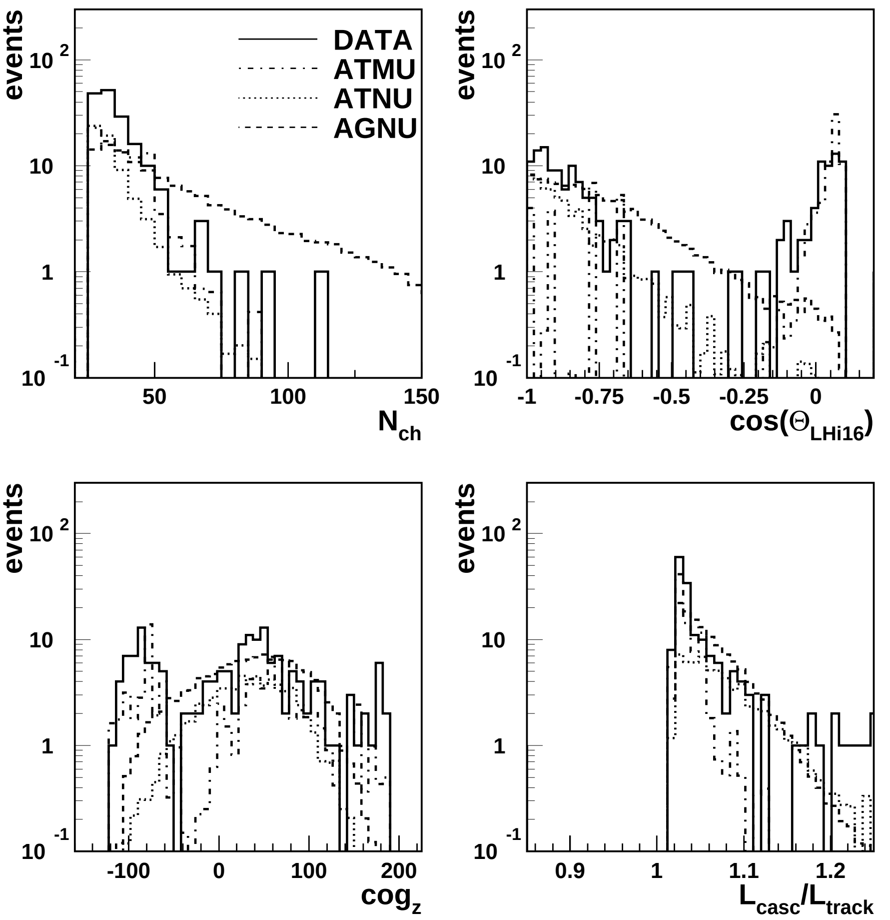

Figure 7.5: The four final cut parameters after the likelihood ratio cut. The cog_z triple peak structure is reproduced by the sum of background and atmospheric neutrino MC.

into the instrumented volume. The poor information leads to an increased rate of misreconstruction. Both peaks in the center of gravity are reproduced by the background MC. The lower peak is larger because in addition events with bright showers below the detector are misidentified by the reconstruction as upward going muons, due to the upward moving light. For this scenario most hits are located close to the bottom of the array, resulting in a low center of gravity.

After the cog_z-cut the zenith angle distribution already decays into two event classes: one piling up at the horizon and one in vertical direction (see figure 7.6). The events close to the horizon are reproduced by the background MC. They are due to poorly reconstructed tracks from just above the horizon. The upward going tracks are reproduced by the atmospheric neu-

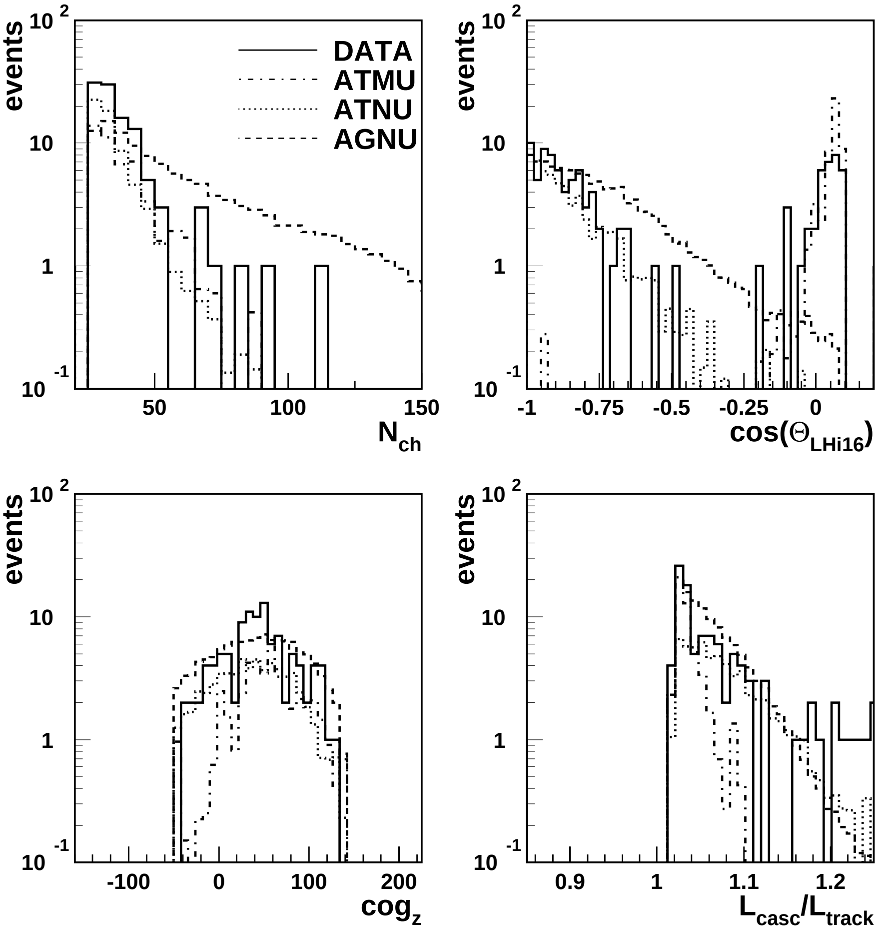

Figure 7.6: The four final cut parameters after the liklihood ratio and cog_z cut. The zenith distribution now decays into two groups of events. They can be separated by a zenith cut at $\theta_{LHi16} > 110^\circ$ ($\cos\theta_{LHi16} < -0.342$).

trino MC.

The zenith angle cut ($\theta_{LHi16} > 110^\circ$, [$\cos\theta_{LHi16} < -0.342$])

The zenith angle cut in the valley between nearly horizontal tracks and vertical tracks removes the majority of the fakes. After this cut experimental data are consistent with atmospheric neutrino MC in all four distributions (figure 7.7. The background MC is nearly completely removed.

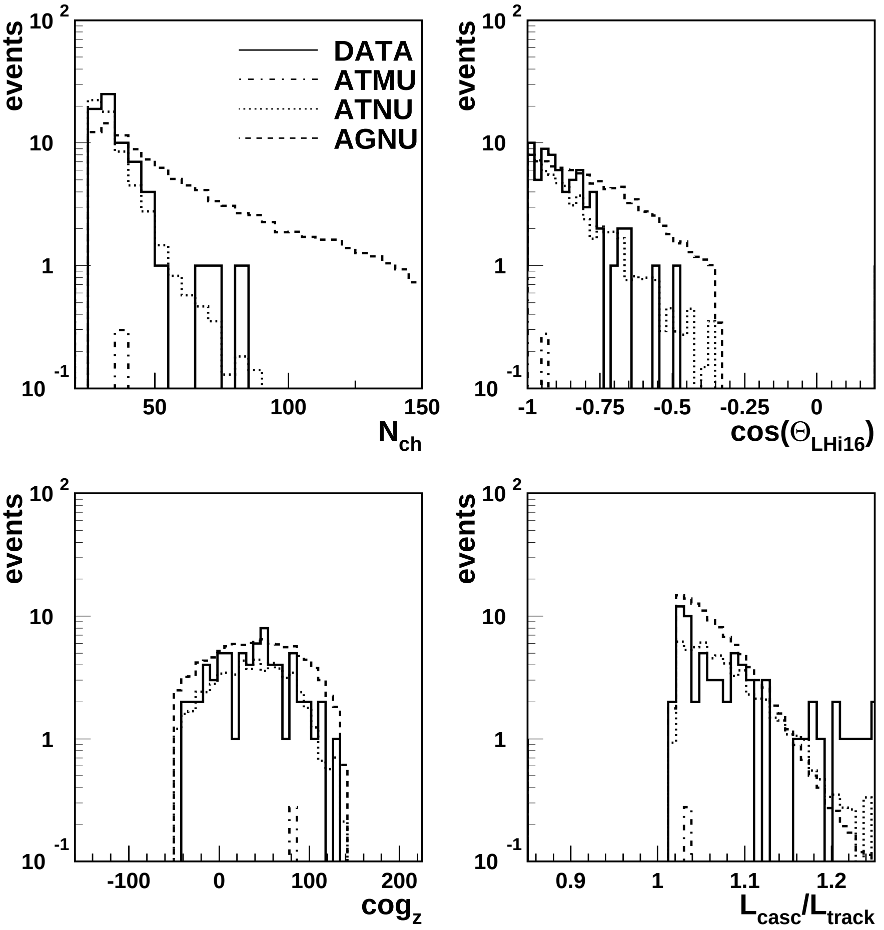

Figure 7.7: The four final cut parameters just before the final N_{ch}-cut. All four distributions show nice agreement between data and the atmospheric neutrino hypothesis. The final N_{ch}-cut will be placed according to maximal sensitivity.

7.5 Limit Calculation

After the filter level three and the three cuts introduced above, a clear excess of high energy signal expectation over the atmospheric neutrinos remains in the N_{ch} distribution . Because no excess of data over the atmospheric neutrino prediction is observed, a limit can be derived. The final cut on the number of hit channels is placed according to maximal sensitivity, i.e., the lowest average upper limit. The motivation of the final cut will be discussed in some detail according to the procedure introduced in section 5.4. Note that **average** *upper limits* refer to MC based predictions based on the average over many identical experiments. In contrast *upper limits* are results based on the experimental observation. Two kinds of limits are used:

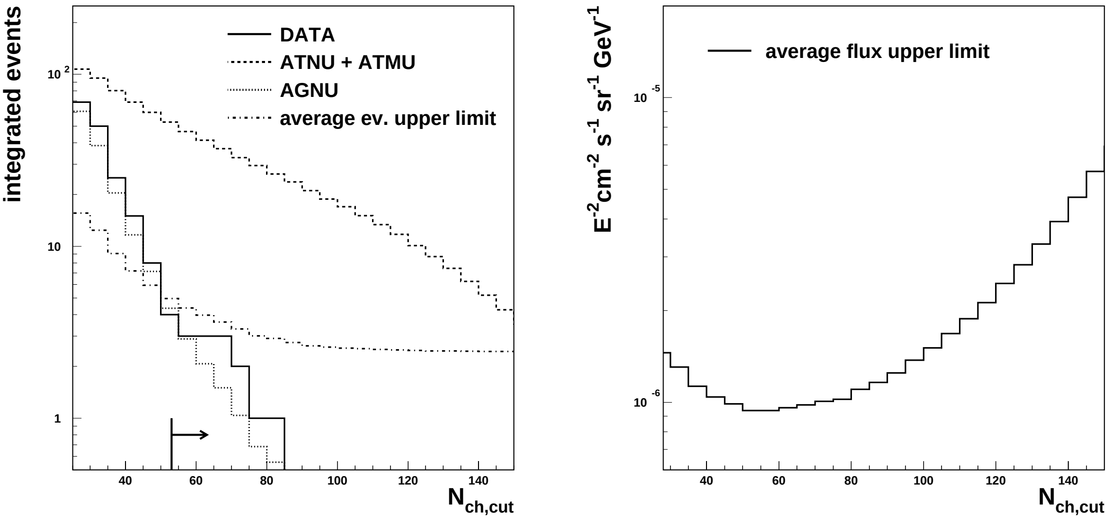

Figure 7.8: Left: The integrated N_{ch} distribution for experimental data together with atmospheric neutrino prediction and high energy neutrino prediction. Also, the average event upper limit based on atmospheric neutrinos and background MC is shown. The arrow indicates the final cut position at $N_{ch} > 53$. Right: The average upper limit as function of the cut position.

event upper limits, referring to the maximal number of events observed, and *flux* upper limits referring to the maximal flux consistent with the event upper limit.

The integrated number of events as function of the cut on the number of hit channels N_{ch}^{cut} for experimental data, atmospheric neutrino MC and high energy neutrino MC is shown in figure 7.8 (left plot). Further the average event upper limit is plotted. This is the maximal number of signal events observed (at 90% confidence level) if precisely as many events are observed as expected from background, i.e. downgoing muons and atmospheric neutrinos. The high energy event expectation is proportional to the simulated flux of $d\Phi/dE = 10^{-5}\ E^{-2}\ \text{cm}^{-2}\text{s}^{-1}\text{sr}^{-1}\text{GeV}$. In order to be consistent with the average event upper limit, the flux is scaled down by the ratio of average event upper limit to high energy signal expectation. The resulting flux estimate is the average flux upper limit as plotted in figure 7.8 (right). The highest sensitivity is reached at the point of the lowest average flux upper limit. Note that this is a purely MC based parameter. The choice of the final cut is therefore independent of experimental data. This avoids the dependence of the cut on fluctuations and yields in the limit of many identical experiments the best exploitation of the experimental information. The experimental data in figure 7.8 are just added in order to show the good agreement between experimental data and atmospheric neutrino prediction.

The final N_{ch}-cut is placed at the position of the lowest average flux upper limit i.e. the highest sensitivity. The minimum of $d\Phi/dE = 0.9 \cdot 10^{-6}\ E^{-2}\ \text{cm}^{-2}\text{s}^{-1}\text{sr}^{-1}\text{GeV}$ is found for $N_{ch} > 53$.

Before this cut, 0.4 events are expected from background, 60.4 events from atmospheric neutrino MC. A high energy neutrino flux of $d\Phi/dE = 10^{-5}\ E^{-2}\ \ \mathrm{cm}^{-2}\mathrm{s}^{-1}\mathrm{sr}^{-1}\mathrm{GeV}$ would result in 107.2 events. In experimental data 69 events are observed. After this cut no MC background is left, 3.12 events are expected from atmospheric neutrino MC and 47.8 events from high energy neutrinos. Three events are observed in experimental data. This is an excellent agreement with the prediction from atmospheric neutrinos. It results in an event upper limit of 4.3 for high energy neutrino events. The flux upper limit is

$$E^2 \left(\frac{d\Phi_{\nu+\bar{\nu}}}{dE}\right)_{90\%\ C.L.} \leq 0.9 \cdot 10^{-6}\mathrm{cm}^{-2}\mathrm{s}^{-1}\mathrm{sr}^{-1}\mathrm{GeV} \tag{7.5}$$

The energy spectrum assumed is not limited in range. However, the flux is only constrained in the range where a signal would be detected. The energy spectrum as predicted from atmospheric MC and high energy neutrino MC before and after the final N_{ch}-cut is shown in figure 7.9. For the hypothesis of atmospheric neutrinos the final events have energies of a few TeV (mean 2.7 TeV). For an E^{-2}-spectrum the detector is most sensitive in the range of tens of TeV (mean 80 TeV). 90% of the predicted high energy neutrino events have energies between 6 TeV and 1 PeV.

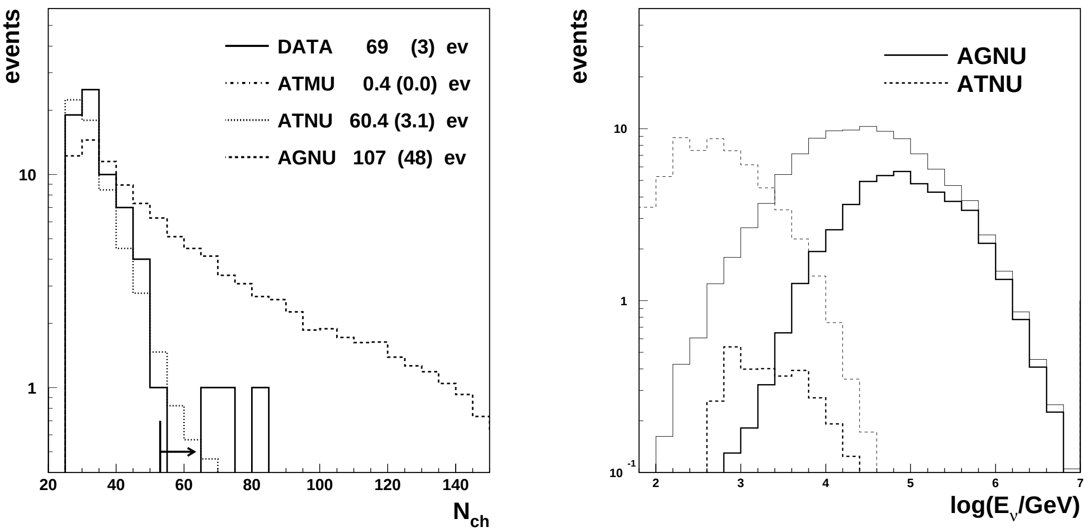

Figure 7.9: The flux limit. Left: The numbers in the plot give the events for each sample before and after the final N_{ch}-cut (arrow). Right: The energy spectrum predicted for atmospheric neutrinos and high energy neutrinos before (thin lines) and after (bold lines) the final N_{ch}-cut.

7.6 Systematics

The limit presented above is based on the signal prediction from the neutrino MC. This MC has been developed further over the course of several iterations on the atmospheric neutrino analysis. For the analysis presented here different versions of signal MC with varied physics input were processed in order to estimate the systematic uncertainty of the signal prediction.

The statistical uncertainty of the experimental data is taken into account in the limit calculation. However, the systematic uncertainty of the signal prediction has to be taken into account separately. The analysis shown above is based on the MC version favored by the atmospheric neutrino analysis [101]. In order to get an estimate of the systematic uncertainty of the limit from the signal prediction, four variations of the signal MC have been analyzed. The following variations to the used MC have been compared:

Angsens is the latest release of the MC and was used in the high energy analysis presented above. It was derived from the previous standard MC (version4) by the introduction of a semi-empirical angular sensitivity of the optical module. This sensitivity is based on the comparison of the hit frequency as a function of module orientation relative to the expected wave front. Experimental data were compared to the result of the standard MC simulation. This way the variation of the sensitivity possibly compensates for other MC-data discrepancies. The use of this MC is justified by the fact that the MC-data comparison is done on a low rejection level with downgoing muons. So the final signal prediction is not biased in a trivial way. The comparison of this MC version with data and other MC versions in the most recent atmospheric neutrino analysis clearly favors this MC version.

Version4 This MC was the standard MC before the version *angsens* was developed. It shows the systematic shift in the number of hit channels discussed in the previous chapter. The most favored reason for this difference to the data is an angle dependent, overestimated module sensitivity. The difference between the two MC versions characterized the uncertainty in the angle dependent module sensitivity.

Relsens This version is a modification of the *Version4* MC. The individual optical module sensitivity was lowered by 15%. The comparison of the two MC allows to quantify the influence of the uncertainty in the OM sensitivity. An independent investigation of the sensitivity dependence of the signal prediction [104] found that the number of predicted atmospheric neutrino events scales approximately linearly with the OM-sensitivity.

Angsenli This version is derived from *angsens*. It was produced with an alternative muon propagation code. The standard MC is propagated with a code based on [81]. This version is based on the propagation model by [82]. The difference between *angsens* and *angsensli* quantifies the uncertainty due to the muon propagation.

PTD2 This version is a modification of *version4*. A correction applied to the light propagation code changed the expected light output. The effect of this change on the final limit may be used as a measure for possible fluctuations due to further corrections.

The filtering and the three selection cuts on the likelihood ratio, the center of gravity and the zenith angle were left unchanged:

$$\begin{array}{rcl} L_{casc}/L_{track} & > & 1.02 \\ -50\text{ m} & < cog_z < & +140\text{ m} \\ \theta_{LHi16} & > & 110.^\circ \end{array} \qquad (7.6)$$

However, the final cut on the number of channels was redefined for each MC version, with the same procedure as used for the standard MC. Due to the variation in neutrino prediction, the best sensitivity is reached at different cut positions for different MC versions.

For each of the variations, the integrated N_{ch} distributions for atmospheric and high energy neutrino prediction are compared to data (see figure 7.10). None of the MC versions describes the data as a superposition of atmospheric neutrinos and a high energy component. Such a superposition would produce a change of slope in the integrated N_{ch} distribution. This is not observed in the data at a significant level. The observed data are reproduced best by the used MC version *angsens*. This is also in agreement with the atmospheric neutrino analysis [101].

Further the sensitivity (average flux upper limit) and the flux upper limit was calculated for each of the MC versions. The final cut on the number of channels was placed according to the lowest average upper limit. Together with the expected number of events for the different samples and before and after the final N_{ch} cut they are shown in table 7.2.

	Angsens	Version4	Relsens	Angsensli	PTD2
before final cut					
exp. data	69	69	69	69	69
atm. μ (BGMC)	0.44	0.44	0.44	0.44	0.44
atm. ν	60.4	147.6	108.3	35.7	168.3
HE ν	107.2	157.6	135.2	105.9	154.1
N_{ch} - cut position	> 53	> 60	> 55	> 51	> 69
after final cut					
exp. data	3	3	3	4	2
atm. μ (BGMC)	-	-	-	-	-
atm. ν	3.13	5.81	5.60	3.75	4.60
HE ν	47.8	56.8	54.1	61.6	46.4
average event upper limit	4.47	5.46	5.39	4.73	5.04
event upper limit	4.31	2.26	2.40	4.85	1.97
average flux upper limit (sensitivity) [10^{-6} E^{-2} cm^{-2}s^{-1}sr^{-1}GeV]	0.93	0.96	0.99	0.70	1.07
limit obtained from exp. data [10^{-6} E^{-2} cm^{-2}s^{-1}sr^{-1}GeV]	0.90	0.40	0.44	0.79	0.42

Table 7.2: Results of the limit calculation for the different MC versions. The fluctuation of the sensitivity and upper limit is a measure for the systematic uncertainty of the limit.

All investigated MC versions yield sensitivities of $0.7 - 1.1 \cdot 10^{-6}$ E^{-2} cm^{-2}s^{-1}sr^{-1}GeV. The fluctuation is smaller than that observed for the total number of predicted events. The reason is the correlation between atmospheric and high energy neutrino prediction. The obtained actually limits however, fluctuate by about a factor two. This is because for three of the five MCs the

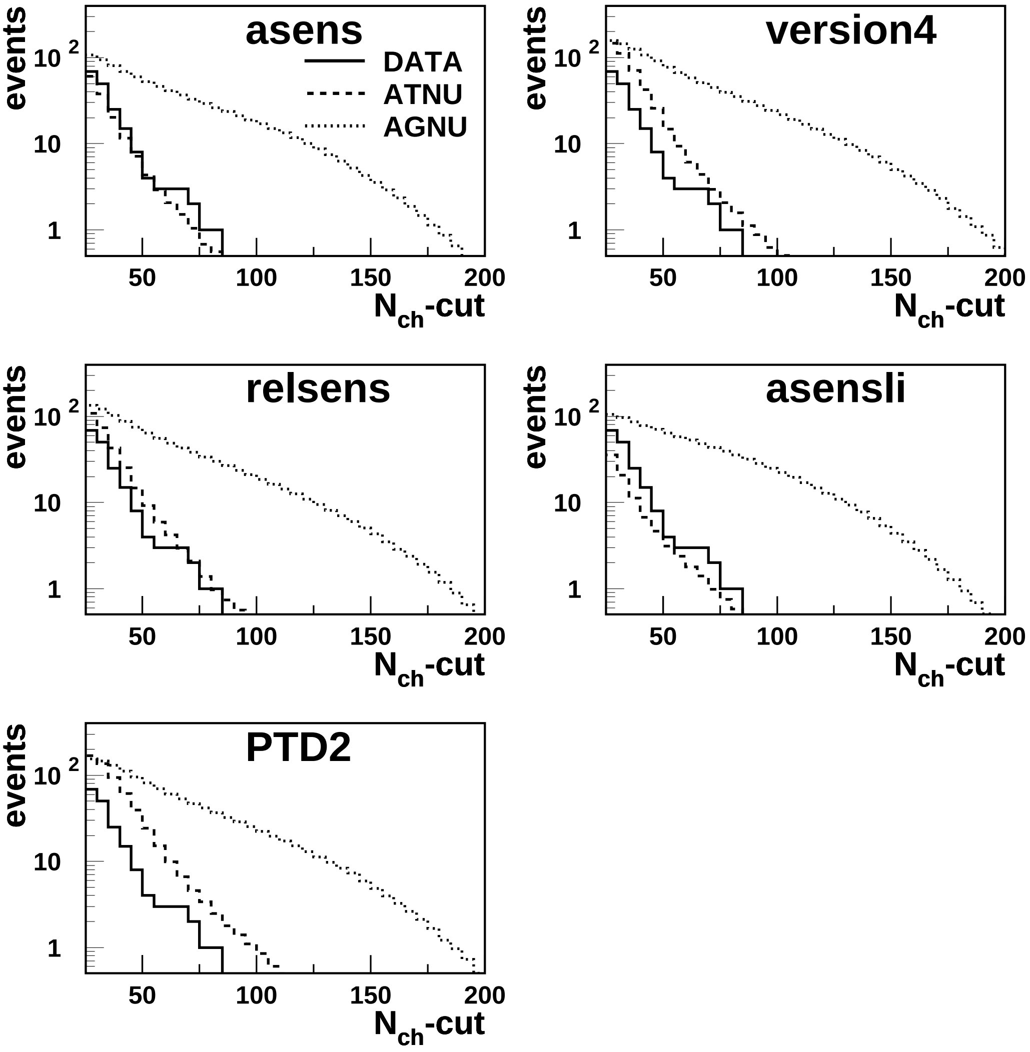

Figure 7.10: The integrated N_{ch}-distribution for the four analyzed variations of the signal MC.The best fit of the data is reached by version *angsens* shown in figure 7.8.

data are much below the expectation for atmospheric neutrinos. The probabilities to observe such a downward fluctuation however is low. The more likely reason for these observations is a systematic disagreement between MC and data. The used MC *angsens* reproduces the data best. At the same time it yields the most conservative upper limit. Therefore no systematic error is added to the flux limit obtained with *angsens* at this point.

At present the sensitivity of the optical module, including effects of the hole ice, is uncertain to a level of 30%. This is about the difference between the standard MC and the MC that reproduced the data best in the sensitivity analysis [104]. A 15% reduction (*relsens*) in the OM sensitivity reduces the predicted rate for high energy neutrinos by 14%, and for atmospheric neutrinos by 27%. Due to the positive correlation of the predictions for atmospheric and high energy neutrinos, the corresponding increase of the average upper limit is much smaller: +3%. The stronger disagreement of the actual upper limit based on the data (10%, from 0.40 to $0.44 \cdot 10^{-6}\ E^{-2}\ \mathrm{cm}^{-2}\mathrm{s}^{-1}\mathrm{sr}^{-1}\mathrm{GeV}$) is introduced by the obviously bad description of the overall experimental data rate by the *version4* MC. It yields a considerably higher rate for atmospheric neutrinos than observed in experimental data and, correspondingly, produces an artificially low limit. Therefore, rather the 3% given by the average upper limit, than the 10% difference are considered a measure for the systematic uncertainties due to the OM sensitivity.

The uncertainty of the primary atmospheric neutrino flux is about 30% [108]. Assuming a variation of ±30% of the atmospheric neutrino flux results in a change in sensitivity of (-5%, +10%). In a similar way as discussed for the OM sensitivity, the resulting disagreement between the atmospheric neutrino prediction of 42.5 and 89.7 events and experimental data (69 events) introduces a stronger fluctuation of the actual limit: for a 30% reduced (increased) atmospheric neutrino flux one yields a change of the limit of +20% (-20%). Note that the actual flux limit shows an “inverted” behavior as compared to the expectation from the sensitivity. This is a result of the discrepancy between data and MC, introduced by the scaling of the flux. With the same argument as above the fluctuation of the sensitivity is taken as a measure of the systematic uncertainty rather than the variation of the limit. Further, the scaling by 30% exceeds the statistical uncertainty of the number of measured events ($\approx$ 15%). With an assumed uncertainty of the total number of events of 15% the uncertainty of the sensitivity is of the order of 5%. This is taken as measure for the systematic uncertainty of the limit due to the primary atmospheric flux normalization.

Flux Limit on High Energy only Selection

In section 7.3 four modes of cut optimization were introduced. The first two were defined to optimize the atmospheric neutrino response and the last two to optimize the response to an E^{-2}-spectrum. The result of all modes influenced the choice of parameters for the selection presented above. However, the cuts were chosen in a way, that high energy *atmospheric* neutrinos were observed, as proof of the sensitivity at high multiplicities.

In order to gain additional confidence in the limit presented above, the two modes, that optimized the response to high energy neutrinos only, were analyzed. The result shall be presented briefly.

Mode SIGNIF(AGNU) selects the following cut set:

$$\begin{aligned} \theta_{LHi16} &> 101.25^\circ \\ N_{ch} &> 61 \\ L_{casc}/L_{track} &> 0.975 \\ P_{hit}^{av,geo} &> 0.485 \\ \sqrt{S_{phit} * S_{van}} &< 0.225 \quad . \end{aligned} \tag{7.7}$$

The hand made cut set introduced in the previous section (see cut set 7.6) is close to the one derived from the data independent optimization 7.7. Clearly the most important cut is the zenith angle followed by N_{ch} in its function as energy selection parameter. The ratio of likelihood efficiently rejects spherical events. $P_{hit}^{av,geo}$ is the geometrical average of the hit probabilities for all hit modules. It is correlated with the muon energy (see section 5.2.2 for details). The last parameter yields only a minor improvement of the sensitivity (0.5%). The sensitivity derived from MC only is $5.4 \cdot 10^{-7}\ E^{-2}\ \mathrm{cm^{-2}s^{-1}sr^{-1}GeV}$. However, there are remaining events in experimental data that show the topology of cog_z events: With two exceptions they have a spherical hit topology, i.e. a likelihood ratio smaller than one. Further, they are concentrated at the bottom of the detector i.e. half of them have a cog_z smaller than -80 m. The rejection of these events requires additional cuts, such that the sensitivity improves only little as compared to the cut set presented before.

Mode AGNU is defined by the optimization function $AGNU/\sqrt{ATMU + ATNU}$. It yields a cut set, that removes more of the unsimulated background:

$$\begin{aligned} \theta_{LHi16} &> 97.1^\circ \\ P_{hit}^{av,geo} &> 0.543 \\ L_{casc}/L_{track} &> 0.974 \\ P_{nohit}^{av,geo} &> 0.893 \\ 3 \cdot I_1/(I_1 + I_2 + I_3) &< 0.809 \quad . \end{aligned} \tag{7.8}$$

After visual inspection, only a simple multiplicity cut at $N_{ch} > 45$ was added to remove all but two candidates. In figure 7.11 each cut parameter is plotted for all four event samples and after all other cuts are applied. It shows that each cut is needed and that the remaining events are close to background from atmospheric neutrinos and muons.

After all cuts are applied the following number of events are expected from the four samples: 0.64 events from atmospheric muons, 1.21 events from atmospheric neutrinos and 66.4 events from a flux of $10^{-5}\ E^{-2}\ \mathrm{cm^{-2}s^{-1}sr^{-1}GeV}$. From experimental data 2 events are observed. This is in good agreement with the prediction of 1.85 background events total and yields an event upper limit of 4.06 events and an upper flux limit of $0.61 \cdot 10^{-6}\ E^{-2}\ \mathrm{cm^{-2}s^{-1}sr^{-1}GeV}$.

This result indicates that even with the available data a more stringent limit, than obtained above, can be derived. It can be taken as a preliminary limit in the sense, that it may be

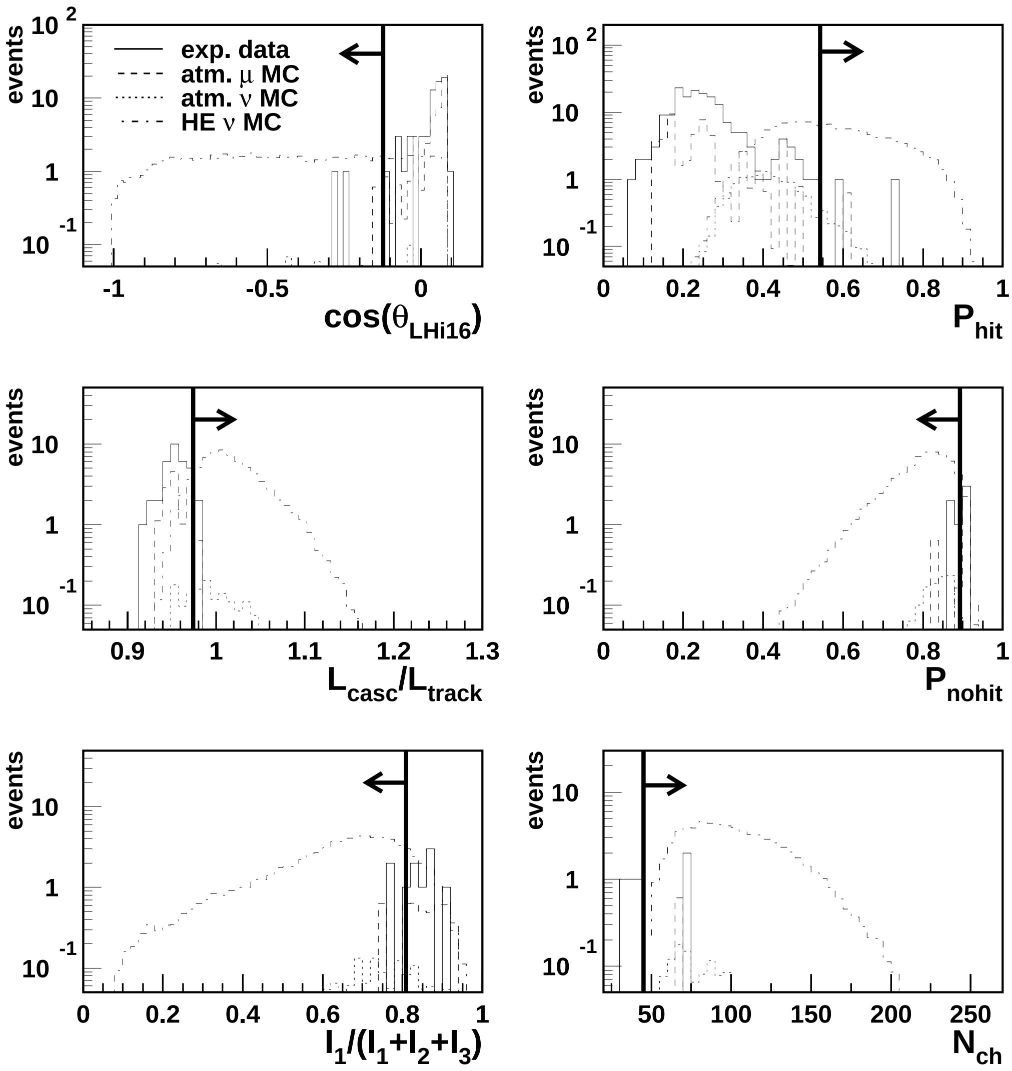

Figure 7.11: The HE only optimization cut set. The distribution for experimental data (solid line), atmospheric muon MC (dashed line), atmospheric neutrino MC (dotted line) and high energy neutrinos (dash-dotted line) are shown. Each cut parameter is plotted with all other cuts applied.

established as limit after the systematic uncertainty estimates, as discussed for the selection in the previous section, are resolved. Unfortunately, this goes beyond the time frame of this work. However, the fact that there was no observation with this cut set, which was chosen nearly *ad hoc*, may be taken as a systematic check for the upper limit at $0.9 \cdot 10^{-6}\ E^{-2}\ \mathrm{cm}^{-2}\mathrm{s}^{-1}\mathrm{sr}^{-1}\mathrm{GeV}$.

7.7 Conclusion

Based on the experience from the analysis of the atmospheric neutrinos sample a separate high energy event filter was developed. The last cut level was derived with a systematic scan of cut parameters. A set of three cuts was chosen to separate high energy neutrinos. The observed sample was consistent with the MC prediction for atmospheric neutrinos. Because no excess was found, a fourth cut on the number of channels was applied. From the remaining events a limit on the flux of neutrinos from a E^{-2} spectrum was derived. The systematic uncertainty of the limit due to the uncertainties of atmospheric neutrino flux prediction, the optical module sensitivity, muon propagation and photon propagation was estimated to a total of 10%, Including the uncertainties, a limit on the extraterrestrial flux of muon neutrinos with an E^{-2}-spectrum, for energies between 5 TeV and 1 PeV, can be placed at

$$E^2 \left(\frac{d\Phi_{\nu+\bar{\nu}}}{dE} \right)_{90\%\ C.L.} \leq 1.0 \cdot 10^{-6} \mathrm{cm}^{-2}\mathrm{s}^{-1}\mathrm{sr}^{-1}\mathrm{GeV} \quad . \tag{7.9}$$

From a cut set optimized for high energy events only, a preliminary limit at

$$E^2 \left(\frac{d\Phi_{\nu+\bar{\nu}}}{dE} \right)_{90\% C.L.} \leq 0.61 \cdot 10^{-6} \mathrm{cm}^{-2}\mathrm{s}^{-1}\mathrm{sr}^{-1}\mathrm{GeV} \tag{7.10}$$

was derived.

Chapter 8

Conclusion and Outlook

AMANDA-B is operational since 1996. The analysis of the data of AMANDA-B10 taken in 1997 has developed to a stage where the conclusive observation of atmospheric neutrinos proves the detection capabilities for TeV neutrinos.

The topic of this thesis is the search for a cosmic flux of high energy neutrinos. In a first approach, the sample of atmospheric neutrinos has been analyzed with respect to an additional component of high energy neutrinos. An energy reconstruction based on the measured amplitudes has been developed and compared to other energy selection parameters. It was found that for the relatively small detector AMANDA-B10 the energy resolution is limited by the stochastics of the light production. Further the atmospheric neutrino selection was found to be inefficient at high energies. As a consequence, a separate high energy selection was performed.

For the high energy selection a separate filter was developed. In a systematic analysis the most efficient cuts for the selection of high energy neutrinos from a E^{-2} spectrum were developed. In order to reject an unsimulated class of background, the cuts found with a cut-optimizing routine were slightly modified. With a comparatively simple set of three cuts a sample of high energy neutrinos could be separated. The found events are consistent with the prediction for atmospheric neutrinos with up to TeV energies. With an additional cut on the number of channels the majority of the events could be rejected. No indication of an excess due to a cosmic neutrino flux was found. Therefore a limit on a hypothetical flux with spectral index $\gamma = 2$ in the energy range from 5 TeV to 1 PeV was derived. After an estimation of the systematic uncertainties a limit could be placed at:

$$E^2 \left(\frac{d\Phi_{\nu+\bar{\nu}}}{dE} \right)_{90\%\ C.L.} \leq 1.0 \cdot 10^{-6} \mathrm{cm}^{-2} \mathrm{s}^{-1} \mathrm{sr}^{-1} \mathrm{GeV} \qquad .$$

This limit is currently the lowest limit on the flux of muon neutrinos with an E^{-2}-spectrum. A comparison to other experimental limits, theoretical bounds and flux predictions discussed in detail in the introduction is shown in figure 8.1. The limit is slightly below the theoretical upper bound derived from the diffuse gamma ray background. An early AGN-core model with pp-interaction [36] is just about excluded.

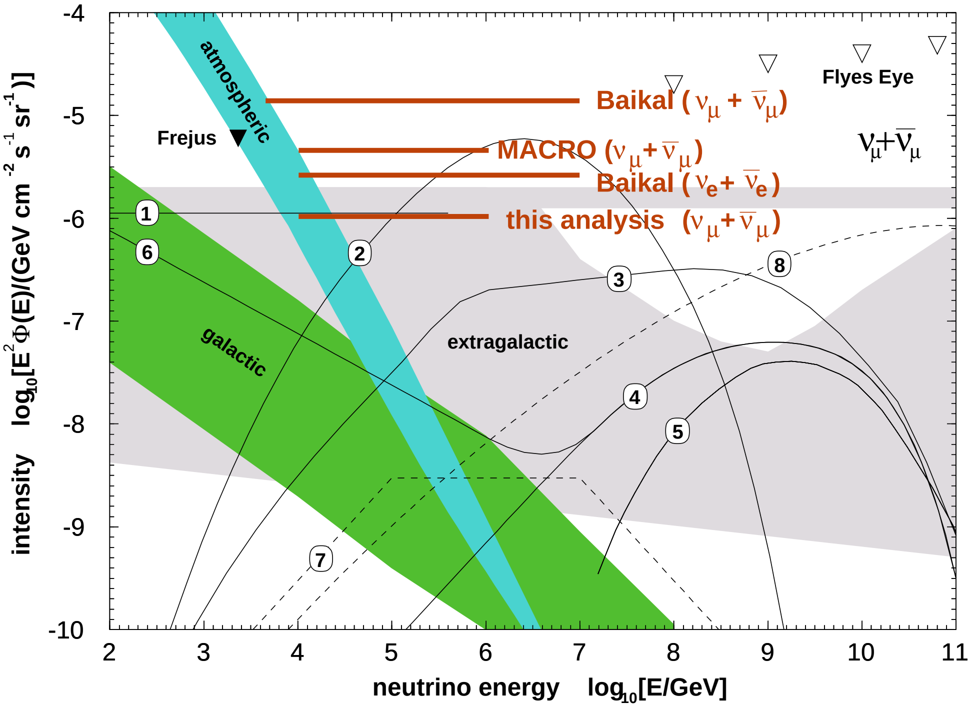

Figure 8.1: The derived flux limit in comparison with the flux predictions, theoretical upper bounds and other experimental limits as introduced in the first chapter (taken from [3], for details see section 2.6).

A previous preliminary upper limit of $E^2 d\Phi/dE \leq 1.6 \cdot 10^{-6}\mathrm{cm}^{-2}\mathrm{s}^{-1}\mathrm{sr}^{-1}\mathrm{GeV}$ [102] could be settled with this analysis and slightly lowered. The limit derived in this work was shown as preliminary at NANP [109] and at the ICRC 2001 [110] and will be presented as final limit in a journal publication [111].

As a part of this work, the proposed IceCube detector has been analyzed with MC methods currently used for AMANDA. The work has been developed further in the framework of a diploma thesis [71]. As one of the central results, the sensitivity of IceCube has been estimated to reach $E^2 d\Phi/dE = 3 \cdot 10^{-9}\mathrm{cm}^{-2}\mathrm{s}^{-1}\mathrm{sr}^{-1}\mathrm{GeV}$.

The development of the analysis methods to a level, where high energy atmospheric neutrinos can reliably be detected, has taken years. At this stage the search for cosmic neutrinos has just begun. Since the data used in this analysis were taken, the detector has been completed and more data have been accumulated. With three years data on tape and 19 strings in the ice, the sensitivity to high energy fluxes will improve considerably in the near future.

Bibliography

[1] T. K. Gaisser, F. Halzen, and T. Stanev. Particle astrophysics with high energy neutrinos. *Phys. Rep.*, 258:175–236, 1995.

[2] O. C. de Jager and F. W. Stecker. Extragalactic Gamma-Ray Absorption and the Intrinsic Spectrum of Mkn 501 During the 1997 Flare. 2001. astro-ph/0107103.

[3] J. G. Learned and K. Mannheim. High-Energy Neutrino Astrophysics. *Annual Reviews of Nuclear Science*, 50:679–749, 2000.

[4] E. Fermi. On the Origin of Cosmic Radiation. *Phys. Rev.*, 75:1169 – 1174, 1949.

[5] E. Fermi. Galactic magnetic fields and the origin of cosmic radiation. *Astrophys. J.*, 119:1–6, 1954.

[6] T. K. Gaisser. *Particle astrophysics with high energy neutrinos.* Cambridge University Press, 1992.

[7] W. Bednarek and R. J. Protheroe. Gamma-ray and neutrino flares produced by protons accelerated on an accretion disc surface in active galactic nuclei. *Mon. Not. Roy. Astr. Soc.*, 302:373–380, 1999.

[8] C. A. Haswell, T. Tajima, and J.-I. Sakai. High-energy particle acceleration by explosive electromagnetic interaction in an accretion disk. *Astrophys. J.*, 401:495–507, 1992.

[9] T. K. Gaisser. Semi-analytic approximations for production of atmospheric muons and neutrinos. In *Proc. International Workshop on Observing Ultra-high Energy Cosmic Rays from Space and Earth*, April 2000.

[10] `http://hires.physics.utah.edu/general/detect.html`.

[11] J. H. Buckley et al. Constraints on cosmic-ray origin from TeV gamma-ray observations of supernova remnants. *Astron. & Astrophys.*, 329:639–658, January 1998.

[12] M. Catanese and T. C. Weekes. Very High Energy Gamma-Ray Astronomy. *Proc. Astron. Soc. Pac.*, 111:1193–1222, October 1999.

[13] T. Weekes. Status of VHE astronomy. astrop-ph/0010431, June 2000.

[14] N. Hayashida et al. The anisotropy of cosmic ray arrival directions around 10^{18} eV. *Astroparticle Physics*, 10:303–311, May 1999.

[15] D. J. Bird et al. Study of Broad-Scale Anisotropy of Cosmic-Ray Arrival Directions from 2×10^{17} to 10^{20} Electron Volts from Fly's Eye Data. *Astrophys. J.*, 511:739–749, February 1999.

[16] L. V. Volkova. *Yad. Fiz.*, 31:1510, 1980. Sov. J. Nucl. Phys. **31** , 784 (1980).

[17] T. G. Gaisser. Cosmic Rays and Particle Physics. *Cambridge University Press*, 1992.

[18] P. Lipari. In *Proc. Workshop on Methodical Aspects of Underwater/Ice Neutrino telescopes*, August 2001.

[19] M. Thunman, G. Ingelman, and P. Gondolo. Charm Production and High Energy Atmosheric Muon and Neutrino Fluxes . *Astropart.Phys.*, 5:309–332, 1996.

[20] L. Pasquali, M. H. Reno, and I. Sarcevic. Neutrinos and Muons from Atmospheric Charm. *hep-ph/9905389*, 1999.

[21] L. V. Volkova et al. Prompt-muon production in cosmic rays. *Nuovo Cimanto C10*, page 465, 1987.

[22] P. Lipari. Lepton spectra in the earth's atmosphere. *Astropart. Phys.*, 1:195 – 227, 1993.

[23] K. Greisen. *Phys. Rev. Lett.*, 16:748, 1966.

[24] G. T. Zatsepin and V. A. Kuzmin. *Pisma Zh. Eksp. Teor. Fiz.*, 4:114, 1966.

[25] St. Hundertmark. In *Proceedings ICRC 2001*, pages 1129–1132, 2001.

[26] A. M. Atoyan et al. On the gamma-ray fluxes expected from Cassiopeia A. *Astron. & Astrophys.*, 355(1):211 – 220, 2000.

[27] V. S. Berezinskii and V. S. Ptuskin. Radiation from young SN II shells produced by cosmic rays accelerated in shock waves. *Astron. & Astrophys.*, 215:399–408, May 1989.

[28] P. Goldreich and W. H. Julian. Pulsar Electrodynamics. *Astrophys. J.*, 157:869+, August 1969.

[29] W. Bednarek and R. J. Protheroe. Gamma rays and neutrinos from the Crab Nebula produced by pulsar accelerated nuclei. *Phys. Rev. Lett.*, 79:2616–2619, 1997.

[30] R. M. Baltrusaitis et al. Sporadic and periodic 10-1000 TeV gamma rays from Cygnus X-3. *Astrophys. J.*, 323:685–689, December 1987.

[31] C. M. Hoffman, C. Sinnis, P. Fleury, and M. Punch. Gamma-ray astronomy at high energies. *Reviews of Modern Physics*, 71:897–936, 1999.

[32] F. Halzen. Neutrinos in Physics and Astrophysics. In *Proc. Advanced Study Inst. at Boulder*, 1998.

[33] F. W. Stecker, C. Done, M. H. Salamon, and P. Sommers. Erratum: "High-energy neutrinos from active galactic nuclei" [Phys. Rev. Lett. 66, 2697 (1991)]. *Physical Review Letters*, 69:2738+, November 1992.

[34] F. W. Stecker and M. H. Salamon. High Energy Neutrinos from Quasars. *Space Science Reviews*, 75:341–355, January 1996.

[35] A. P. Szabo and R. J. Protheroe. Implications of particle acceleration in active galactic nuclei for cosmic rays and high energy neutrino astronomy. *Astropart. Phys.*, 2:375–392, October 1994.

[36] L. Nellen, K. Mannheim, and P. L. Biermann. Neutrino production through hadronic cascades in AGN accretion disks. *Phys. Rev.*, D 47:5270–5274, 1993.

[37] K. Mannheim. AGN Models : High-Energy Emission. In *Very High Energy Phenomena in the Universe; Moriond Workshop*, pages 17–6, 1997.

[38] C. Hettlage and K. Mannheim. High energy neutrino fluxes from cosmic accelerators. In *Proc. XXIst Moriond Workshop 'Very High Energy Phenomena in the Universe', Les Arcs, France*, January 2001.

[39] E. Waxman and J. Bahcall. *Phys. Rev. Lett.*, 78:2292–2295, 1997.

[40] P. Meszaros and M. J. Rees. Relativistic fireballs and their impact on external matter - models for cosmological gamma-ray bursts. *Astrophys. J.*, 405(1):278–284, 1993.

[41] P. Sreekumar et al. EGRET Observations of the Extragalactic Gamma-Ray Emission. *Astrophys. J.*, 494:523+, February 1998.

[42] E. Waxman and J. Bahcall. High energy neutrinos from astrophysical sources: an upper bound. *Phys. Rev.*, D(54):023002, 1999.

[43] K. Mannheim, R. J. Protheroe, and J. P. Rachen. On the cosmic ray bound for models of extragalactic neutrino production. *Phys.Rev.*, D 63:023003, 2001.

[44] I. A. Sokalski and Ch. Spiering. The Baikal Neutrino Telescope NT-200, Project discription, Moskau/Zeuthen. 1992.

[45] O. Streicher. *Entwicklung einer Methode zur Rekonstruktion der Energie von Myonen mit dem Baikal-Neutrinoteleskop NT-96.* Dissertation, Humboldt-Universität zu Berlin, 2000.

[46] Balkanov et al. An upper limit on the diffuse flux of high energy neutrinos obtained with the Baikal detector NT-96. *Astroparticle Physics*, 14:61–66, 2000.

[47] Z. Dzhilkibaev et al. (The BAIKAL collaboration). A search for very high energy neutrinos with the Baikal Neutrino Telescope. In *Proceedings of the 9th International Workshop: Neutrino Telescopes*, pages 5269+, 2001.

[48] S. P. Ahlen et al. (The MACRO Collaboration). *Nucl. Inst. Meth.*, A324:337, 1993.

[49] L. Perrone et al. (The MACRO Collaboration). Neutrinos Astronomy with MACRO. In *Proceedings ICRC 2001*, 2001.

[50] W. Rhode et al. (Frejus Collaboration). Limits on the flux of very high energy neutrinos with the Frejus detector. *Astropart. Phys.*, 4:217–225, 1996.

[51] R. M. Baltrusaitis et al. Limits on deeply penetrating particles in the $> 10^{17}$ eV cosmic-ray flux. *Phys. Rev.*, D 31:2192–2198, May 1985.

[52] V. S. Berezinsky and V. I. Dokuchaev. Hidden source of high-energy neutrinos in collapsing galactic nucleus. *Astropart. Phys.*, 15:87–96, 2001.

[53] S. Colafrancesco and P. Blasi. Clusters of galaxies and the diffuse gamma-ray background. *Astropart. Phys.*, 9:227–246, October 1998.

[54] P. Bhattacharjee and G. Sigl. Origin and Propagation of Extremely High Energy Cosmic Rays. *Phys.Rept.*, (327):109–247, 2000.

[55] R. Gandhi, C. Quigg, M. H. Reno, and I. Sarcevic. Ultrahigh-energy neutrino interactions. *Astropart. Phys*, (5):81–110, 1996.

[56] Alan D. Martin, W. James Stirling, and Robert G. Roberts. Pinning down the glue in the proton. *Phys. Lett.*, B 354:155–162, 1995.

[57] Particle Data Group. Review of particle physics. *The European Physical Journal C*, 3(1-4):144, 2000.

[58] K. Hirata et al. Observation of a Neutrino Burst from Supernova SN1987A. *Phys.Rev.Lett.*, 58:1490–1493, 1987.

[59] R. M. Bionta et al. Observation of a Neutrino Burst in Coincidence with Supernova SN1987A in the Large Magellanic Cloud. *Phys.Rev.Lett.*, 58:1494–1496, 1987.

[60] Y. Fukuda et al. (The SuperKamiokande Collaboration). Constraints on Neutrino Oscillations Using 1258 Days of Super-Kamiokande Solar Neutrino Data. *Phys. Rev. Lett.*, 86:5656–5660, 2001.

[61] Q. R. Ahmad et al. (The SNO Collaboration). Measurement of the Rate of $\nu_e + d \longrightarrow p + p + e^-$ Interactions Produced by 8B solar neutrinos at the Sudbury Neutrino Observatory. *Phys. Rev. Lett.*, 87:071301, 2001.

[62] P. K. F. Grieder for the DUMAND Collaboration. DUMAND II: String 1 deployment, initial operation, results and system retrieval . *Nuclear Physics B (Proc. Suppl.)*, 43:145–148, 1995.

[63] DUMAND Collaboration. Proposal to Construct a Deep-Ocean Laboratory for the study of High Energy Neutrino Astrophysics and Particle Physics. *HDC-2-88*, Honululu, 1988.

[64] G. V. Domogatsky. The Lake Baikal Experiment: Selected Results, Proceedings NANP 1999. *Phys. Rev. Lett.*, 83, 1999.

[65] E. Aslanides et al. A deep sea telescope for high energy neutrinos. Proposal, ANTARES Collaboration, 1999.

[66] S. Bottai. NESTOR: A Status Report . In *Proc. ICRC 1999, HE 6.3.08.*, 1999.

[67] M. J. Leuthold. IceCube Configuration Studies. In *Zeuthen workshop on simulation and analysis methods for large neutrino telescopes*, pages 484–493, July 1999.

[68] J. Ahrens et al. IceCube: a Kilometer-Scale Neutrino Observatory. A proposal to the National Science Foundation. Proposal, The U.S. institutions of the IceCube Collaboration, 1999.

[69] M. J. Leuthold. Icecube performance studies. *AMANDA internal report 19991102*, 1999.

[70] M. J. Leuthold and H. Wissing. Performance Studies for IceCube. In *Proc. 27th International Cosmic Ray Conference*, Hamburg, Germany, 2001.

[71] H. Wissing. Detection of Cosmic Muon-Neutrinos with ICECUBE. Diploma thesis, Humboldt Universität, Berlin, 2001.

[72] J. Ahrens et al. The IceCube NSF Proposal. Proposal, ICE CUBE Collaboration, 2000.

[73] A. Biron et al. Participation of DESY-Zeuthen in the IceCube Project. May 2001.

[74] E. Andrés et al. The AMANDA neutrino telescope: Principle of operation and first results. *Astropart. Phys.*, 13:1 – 20, 2000. astro-ph/9906203.

[75] E. Dickinson et al. The new South Pole air shower experiment - SPASE-2. *Nucl. Inst. Meth. A*, 440 (1):95–113, 2000.

[76] C. Allen et al. Status of the Radio Ice Cherenkov Experiment (RICE). *New Astronomy Review*, 42:319–329, September 1998.

[77] S. N. Boziev et al. INR-Preprint P-0630, 1989.

[78] D. Heck and J. Knapp. Extensive air shower simulation with CORSIKA: A user's guide. *Forschungszentrum Karlsruhe, Institut für Kernphysik*, January 2000.

[79] K. H. Kampert. First Results from the KASCADE Experiment. In *Very High Energy Phenomena in the Universe; Moriond Workshop*, pages 405+, 1997.

[80] Gary C. Hill. Detecting neutrinos from AGN: New fluxes and cross sections. *Astroparticle Physics*, 6:215–227, 1997.

[81] W. Lohmann, R. Kopp, and R. Voss. Energy loss of muons in the range 1-10000 GeV. *CERN*, 85-03, 1985.

[82] P. Lipari and T. Stanev. Propagation of multi-TeV muons . *Phys. Rev.*, D(44-11):3543, 1991.

[83] C.H. Wiebusch et al. Observation of high energy atmospheric neutrinos with AMANDA. *Proceedings ICRC 2001, HE 2.03.07.*, 2001.

[84] A. Karle. In *Zeuthen workshop on simulation and analysis methods for large neutrino telescopes*, pages 174–185, July 1998.

[85] S. Hundertmark. *Simulation und Analyse von Myonereignissen im Amanda-B4-Neutrinoteleskop*. PhD thesis, Humboldt-Universität zu Berlin, 1999.

[86] S. Hundertmark. Vertical ice properties for the amanda-simulation. *AMANDA internal report*, (20001001), 2000.

[87] V. Stenger. Track fitting for the DUMAND Octogon. Technical Report HDC-1-90, University of Hawaii, 1990.

[88] C. Wiebusch. Muon reconstruction with AMANDA. Technical Report DESY-PROC-1-1999, DESY Zeuthen, 1999.

[89] D. Pandel. Measurment of Water and Detector Parameters and Reconstruction of Muons to Energies of 100 TeV with the Baikal Neutrino Telescope NT-72. Diploma thesis, Humboldt Universität, Berlin, 1996.

[90] M. Gaug, P. Niessen, and C. H. V. Wiebusch. Investigations on Smoothness observables. *Amanda internal report*, (20000201), 2000.

[91] M. Kowalski. On the Reconstruction of Cascade like Events in the AMANDA Detector. Diploma thesis, Humboldt Universität, Berlin, 1999.

[92] M. Gaug. CutEval manual. Technical report, 2001. `http://www-zeuthen.desy.de/ gaug/cuteval/`.

[93] M. Gaug. *Detection of atmospheric muon neutrinos with the AMANDA neutrino telescope*. Diploma thesis, Humboldt-Universität zu Berlin, October 2000.

[94] J. Neyman. *Phil. Trans. Roy. Soc. London, Series A 236*, page 333, 1937.

[95] G. M. Feldman and R. D. Cousins. Unified approach to the classical statistical analysis of small signals. *Physical Review D*, 57(7):3873, 1998.

[96] H. C. Hill and K. Rawlins. Optimising experimental model rejection potential. *AMANDA Internal Report*, (20000902), 2000.

[97] A. Biron, M. Leuthold, and C. H. Wiebusch. First and Second Level Reconstruction of 97 Muon Data. *AMANDA internal report*, (19990701), 1999.

[98] A. Biron, M. Leuthold, and Ch. Wiebusch. Separation of ν_μ event candidates in AMANDA-B10. *AMANDA Internal Report*, (19990902), 1999.

[99] E. Andres et al. (AMANDA Collaboration). Observation of High Energy Neutrinos with Cherenkov Detectors embedded in deep Antarctic Ice. *Nature*, 410:441–443, 2001.

[100] T. R. DeYoung. *Observation of Atmospheric Muon Neutrinos with AMANDA*. PhD thesis, University of Wisconsin, Madison, 2001.

[101] A. Biron, M. Gaug, C. H. V. Wiebusch, and R. P. Wischnewski. Analysis of Atmospheric Neutrinos in 97 Data. *Amanda internal report*, (20010501), 2001.

[102] E. Andres et al. Results from the amanda high energy neutrino detector. *Nucl. Phys. Proc. Suppl.*, 91:423–430, 2000.

[103] G. C. Hill and M. Leuthold. Status of the AMANDA-B10 diffuse limit analysis. In *Proc. Irvine AMANDA meeting*, 2000.

[104] A. Biron and H. Wissing. Impact of Varied OM Sensitivities on the AMANDA-B10 Analysis. *AMANDA internal report*, (20001202), 2000.

[105] P. Olbrechts and C. H. Wiebusch. On the angular sensitivity of optical modules in the ice. *AMANDA internal report*, (20010102), 2000.

[106] Gary C. Hill. Status of the madison 1997 neutrino analysis. In *Proc. Irvine Laguna Beach AMANDA meeting*, October 2000.

[107] J. Lamoreux and J. Jacobsen. (Re) Filtering/Reconstructing 97/98/99 Up-Going AMANDA Events. Technical report, 1999. `http://rust.lbl.gov/~jodi/amanda/97_refilter/index.html`.

[108] Thomas K. Gaisser. Uncertainty in Flux of Atmospheric Neutrinos: Implications for Upward Muons in AMANDA B10. *Amanda internal report*, (20001201), 2000.

[109] M. J. Leuthold. Status of the AMANDA experiment, Proceedings NANP 2001. *in preparation*, July 2001.

[110] G. C. Hill and M. J. Leuthold. Search for a diffuse flux from sources of high energy neutrinos with AMANDA-B10. In *Proc. 27th International Cosmic Ray Conference*, Hamburg, Germany, 2001.

[111] E. Andres et al. in preparation. 2001.

Lebenslauf

Personalien:

Name : Matthias Leuthold
Wohnort : Dolziger Str. 2, 10247 Berlin
Geburtstag und -ort : 23. Februar 1971 in Dresden
Familienstand : ledig
Staatsangehörigkeit : deutsch

Schulbildung:

09/77 - 08/81	Polytechnische Oberschulen in Späningen und Brunau
09/87 - 08/89	Erweiterte Oberschule in Salzwedel Abitur ”mit Auszeichnung”

Wehrdienst:

09/89 - 03/90	Nationale Volksarmee

Studium:

09/90 - 09/93	Grundstudium Physik an der Humboldt-Universität zu Berlin Vordiplom “sehr gut”
01/92 - 06/92	Studienaufenthalt USA am City College of New York of City University New York
10/93 - 04/96	Hauptstudium Physik an der Humboldt-Universität zu Berlin Schwerpunkte: Elementarteilchen-, Laser- und Plasmaphysik
01/96 - 01/97	Diplomarbeit in der Elementarteilchenphysik am DESY Zeuthen Thema: “Untersuchungen zur Effizienz der Rekonstruktion am Experiment HERA-B anhand vollständig simulierter Modellereignisse”
03/97	Studienabschluß als Diplomphysiker Diplom “gut”

Erklärung

Hiermit erkläre ich, die Dissertation selbstständig und ohne unerlaubte fremde Hilfe angefertigt zu haben. Ich habe mich anderwärts nicht um einen Doktorgrad beworben und besitze einen entsprechenden Doktorgrad nicht. Ich erkläre die Kenntnisnahme der dem Verfahren zugrunde liegenden Promotionsordnung der Mathematisch-Naturwissenschaftlichen Fakultät I der Humboldt-Universität zu Berlin.

Berlin, 6. Oktober 2001

Matthias Leuthold